UNIVERSITY OF OSLO
Department of Informatics

Nonlinear propagation of ultrasonic signals. Theoretical studies and potential applications.

Fabrice Prieur

July 5, 2012

Series of dissertations submitted to the
Faculty of Mathematics and Natural Sciences, University of Oslo
No. 1240

ISSN 1501-7710

Cover: Inger Sandved Anfinsen.
Printed in Norway: AIT Oslo AS.

Produced in co-operation with Akademika publishing.
The thesis is produced by Unipub merely in connection with the
thesis defence. Kindly direct all inquiries regarding the thesis to the copyright
holder or the unit which grants the doctorate.

Preface

This thesis has been submitted to the Faculty of Mathematics and Natural Sciences at the University of Oslo in partial fulfillment of the requirements for the degree *Philosophiae Doctor (Ph.D.)*. The work was carried out at the Group for Digital Signal Processing and Image Analysis at the Department of Informatics, University of Oslo, under the supervision of Associate Professor Andreas Austeng and Professor Sverre Holm. It is part of the "High Resolution Imaging and Beamforming" project, financed by the Norwegian Research Council and Kongsberg Maritime.

Acknowledgements

I would like to thank my supervisors, Associate Professor Andreas Austeng and Professor Sverre Holm for their contributions to this work and for introducing me to the field of research. All my co-authors deserve also my recognition for their valuable input and stimulating discussions. In particular, I would like to thank Professor Hans Torp from the Norwegian University of Science and Technology for an exciting collaboration on two articles in the field of medical ultrasound imaging. None of the experimental results presented would have been possible without the precious help from Are Johansen and Max-Ole Wittussen from Kongsberg Maritime with whom we sat during several nights, or without the assistance from Øyvind Standal, Jochen Deibele, and Saeed Mehdizadeh from the Department of Circulation and Medical Imaging at the Norwegian University of Science and Technology. Frank Tichy and Håvard Nes from Kongsberg Maritime as well as Atle Lohrmann from Nortek AS also deserve some acknowledegments for giving me some insights into the world of underwater acoustics. Finally, thanks to Lise for her support and encouragement.

Abstract

Countless applications use the propagation and reflection of sound to gain better knowledge of the surrounding medium. This medium can, for instance, be made of a set of complex and heterogeneous biological tissues or of ships in the sea several kilometres away from the sound receiver. In all cases, the sound propagation is affected by some nonlinear effects. In many applications those effects are neglected, while in others they are exploited.

In this thesis we investigate the possibility of using the nonlinear effects in fields where they are avoided, neglected, or overseen. We also try to establish faster or more accurate estimations of nonlinear sound fields. The two domains that were investigated are the domain of underwater acoustics with applications such as echo sounders or acoustic Doppler current profilers, and the domain of medical imaging.

In underwater acoustics, we studied the combined use of the second harmonic and fundamental signals for imaging using a scientific echo sounders and for determining current velocities using acoustic Doppler current profilers. We show that the use of the second harmonic signal can improve the performance in these applications when the range is limited.

In medical imaging, we investigated the use of the second harmonic signal with the multi-line transmission technique. In this case too, images produced by the second harmonic signal suffer from less perturbations than images produced by the fundamental signal.

We have developed new models to estimate the nonlinear propagation of sound. One model intends to appropriately describes the attenuation and the dispersion observed in complex media. It derives a wave equation with a loss operator defined by fractional order derivatives. The model relies on variations of the constitutive equations that adequately describe the stress-strain relation and heat transfer. The other models based on the quasi-linear approximation intend to speed up or increase the flexibility of the implementation. They proved in one case to be faster than other state-of-the-art simulators, and in the other case, more flexible than alternative methods. Given that the conditions for quasi-linear propagation are satisfied, those simulators adequately describe the sound field for the fundamental and second harmonic signals.

List of Publications

This thesis is based on the following seven papers, referred to in the text by their Roman numerals (I-VII).

I F. Prieur, S. P. Näsholm, A. Austeng, F. Tichy, and S. Holm, "Feasibility of second harmonic imaging in active sonar: measurements and simulations", *IEEE Journal of Oceanic Engineering*, Accepted for publication May 2, 2012.

II F. Prieur and R. E. Hansen, "Theoretical improvements when using the second harmonic signal in acoustic Doppler current profilers", *IEEE Journal of Oceanic Engineering*, Revised version submitted June 11, 2012.

III F. Prieur and S. Holm, "Nonlinear acoustic wave equations with fractional loss operators", *Journal of the Acoustical Society of America*, vol. 130, no. 3, pp. 1125-1132, September 2011.

IV F. Prieur, G. Vilenskiy , and S. Holm, "A more fundamental approach to the derivation of nonlinear acoustic wave equations with fractional loss operators" *Journal of the Acoustical Society of America*, Revised version submitted June 15, 2012.

V F. Prieur, T. F. Johansen , S. Holm, and H. Torp, "Fast simulation of second harmonic ultrasound field using a quasi-linear method" *Journal of the Acoustical Society of America*, vol. 131, no. 6, pp. 4365-4375, June 2012.

VI F. Prieur, "3D simulation of parametric ultrasound fields" *Proceedings of the 19th International Symposium on Nonlinear Acoustics*, Tokyo, Japan, May 2012.

VII F. Prieur, B. Dénarié, A. Austeng, and H. Torp, "Multi-Line Transmission in medical imaging using the second harmonic signal" *IEEE Transactions on Ultrasonics, Ferroelectrics, and Frequency Control*, Submitted July 3, 2012.

Related publications

i S. Holm and F. Prieur, "Low sidelobe limited diffraction beams in the nonlinear regime", *Journal of the Acoustical Society of America*, vol. 128, no. 3, pp. 1015-1020, September 2010.

ii F. Prieur, S. P. Näsholm, A. Austeng, F. Tichy, and S. Holm, "Exploiting nonlinear propagation in echo sounders and sonar", *Proceedings of the European Conference on Underwater Acoustics*, Istanbul, Turkey, July 2010

Contents

Chapter 1

Introduction

Medical ultrasound imaging and underwater acoustic applications are two of many fields where sound is used to gain better knowledge of the environment. The principle of listening to the sound generated by a source, like with passive sonars, or to the echo of a transmitted sound signal after reflection from a target, like with active sonars and in medical ultrasound imaging, involves sound propagation. When the equations describing a problem are linear, many mathematical tools are available and solutions are easier to compute than for nonlinear equations. But the equations of physics describing the propagation of sound are, by definition, nonlinear. Approximations are necessary to obtain a linear equation for sound propagation. For many years, and in many cases, these approximations have managed to describe a large part of the problems involving what is called "small signals" with an adequate precision. But in some scenarios involving "finite amplitude sound", the introduction of nonlinear effects is required to explain the observations. The need for extending the linear theory to include nonlinear effects was prompted by the discovery of nonlinear aspects in existing applications, like the variations of propagation speed with the transmitted pressure level [1], and the emergence of new technologies based on nonlinear interactions, like the parametric acoustic array [2, 3].

1.1 When sound propagates

1.1.1 Constitutive equations

The constitutive equations form the starting point for deriving a wave equation. They describe the physics of the medium when it is disturbed from its equilibrium state by the presence of sound. Three equations are necessary to derive a linear wave equation: the equation of continuity, the momentum equation, and the thermodynamic equation of state. In order to derive a wave equation describing the nonlinear effects in thermoviscous fluids, a fourth equation is necessary, the entropy equation.

The equation of continuity simply states that when the fluid is in motion, the net influx of mass through a fixed volume element must be reflected as density changes within this volume. It links the particle velocity vector $\mathbf{v}$ to the fluid instantaneous density ρ through the relation [4]

$$\frac{\partial \rho}{\partial t} + (\mathbf{v} \cdot \boldsymbol{\nabla})\rho + \rho \boldsymbol{\nabla} \cdot \mathbf{v} = 0, \tag{1}$$

where t is the time.

The momentum equation is the formulation of the law of physics stating that the forces exerted on the fluid contained in a unit of volume are equal to the product of the mass of this volume by its acceleration. It can be written in the case of a thermoviscous fluid as [4]

$$\rho\left(\frac{\partial \mathbf{v}}{\partial t} + (\mathbf{v}\cdot\boldsymbol{\nabla})\mathbf{v}\right) = -\boldsymbol{\nabla}P + \eta\nabla^2\mathbf{v} + (\zeta + \tfrac{1}{3}\eta)\boldsymbol{\nabla}(\boldsymbol{\nabla}\cdot\mathbf{v}), \tag{2}$$

where P is the thermodynamic pressure, η is the shear viscosity, and ζ is the bulk viscosity. In this equation, the terms involving the viscosities are issued from the formulation of the viscous stress tensor for a mechanical model based on the Hooke's law [5]. When more complex models lead to different formulations of the viscous stress tensor, the form of the momentum equation changes. Such models have been used in this thesis to come to a different form of the momentum equation involving fractional derivatives (Eq. (17) in Paper III).

The thermodynamic equation of state relates three quantities describing the thermodynamic behavior of the fluid. These quantities can be P, ρ, and T where T is the temperature, or P, ρ, and s, where s is the specific entropy (per unit of mass). A Taylor expansion of this relation about the equilibrium state is normally used. To the second order, it can be written [4]

$$p = c_0^2\rho' + \frac{c_0^2}{\rho_0}\frac{B}{2A}\rho'^2 + \left(\frac{\partial P}{\partial s}\right)_{\rho,0} s', \tag{3}$$

where p, ρ', and s' are the dynamic pressure, density, and entropy, respectively, describing small disturbances relative to the uniform state of rest, B/A is the parameter of nonlinearity characteristic of the medium [6], and c_0 is the "small signal" sound speed, the pressure dependent sound speed evaluated at equilibrium state.

The entropy equation expresses the dissipation of energy due the fluid viscosity and to heat transfers [7]. For a thermoviscous fluid in which relaxation effects are neglected, it is written [4]

$$\rho T\left(\frac{\partial s}{\partial t} + (\mathbf{v}\cdot\boldsymbol{\nabla})s\right) = \kappa\nabla^2 T + \zeta(\boldsymbol{\nabla}\cdot\mathbf{v})^2 + \frac{1}{2}\eta\left(\frac{\partial v_i}{\partial x_j} + \frac{\partial v_j}{\partial x_i} - \frac{2}{3}\delta_{ij}\frac{\partial v_k}{\partial x_k}\right)^2, \tag{4}$$

where κ is the thermal conductivity and δ_{ij} is the Kronecker delta. The final term of Eq. (4) is written in Cartesian tensor notation: v_i denotes the components of $\mathbf{v}$ in direction x_i. In Eq. (4) as in Eq. (2), the terms involving the viscosities differ when using mechanical models more complex than a Hooke's law. Likewise, the term involving the thermal conductivity κ comes from a heat transfer model based on Fourier's law. Models for heat transfer described by fractional derivatives have also been introduced in this thesis leading to a different form for the entropy equation (Eqs. (6) and (8) in Paper IV).

All these four constitutive equations are nonlinear. Yet it is possible to completely linearize them in order to obtain a linear wave equation, or to keep the nonlinear terms up to a given order and obtain a wave equation describing some nonlinear aspects of sound propagation. As an illustration, a linear wave equation valid to the first order can be derived from these constitutive equations in the very simple case of a fluid of negligible viscosity and thermal conductivity [8] (η, ζ, and κ are of the same order as $\mathbf{v}$ and p and only contribute to the second order). Keeping only the term of

the first order, the continuity equation, Eq.(1), becomes

$$\frac{\partial \rho'}{\partial t} + \boldsymbol{\nabla} \cdot (\rho_0 \mathbf{v}) = 0, \tag{5}$$

where ρ_0 is the density of the medium undisturbed. Likewise, keeping only the term to the first order, the momentum equation, Eq. (2), becomes

$$\rho_0 \frac{\partial \mathbf{v}}{\partial t} = -\boldsymbol{\nabla} p. \tag{6}$$

The linearized equation of state, Eq. (3), reduces to

$$p = c_0^2 \rho'. \tag{7}$$

Taking the time derivative of Eq. (5) and the divergence of Eq. (6) give

$$\frac{\partial^2 \rho'}{\partial t^2} + \boldsymbol{\nabla} \cdot \left(\rho_0 \frac{\partial \mathbf{v}}{\partial t} \right) = 0 \quad \text{and} \tag{8}$$

$$\boldsymbol{\nabla} \cdot \left(\rho_0 \frac{\partial \mathbf{v}}{\partial t} \right) = -\nabla^2 p, \tag{9}$$

which when combined give

$$\frac{\partial^2 \rho'}{\partial t^2} = \nabla^2 p. \tag{10}$$

Using Eq. (7) to replace ρ' in Eq. (10), we get

$$\frac{1}{c_0^2} \frac{\partial^2 p}{\partial t^2} = \nabla^2 p, \tag{11}$$

which is a linear wave equation describing propagation of sound in a lossless medium and valid to the first order.

1.1.2 Nonlinear wave equations

Daring not to present the first contributions to the formulations of nonlinear sound propagation in the eighteenth and nineteenth centuries by Euler, Lagrange, Poisson, Stokes, and Earnshaw, we jump straight to the middle of the twentieth century and present three of the most used wave equations describing the nonlinear propagation of sound. The equations presented in this section can all be found in Ref. [4]. To get to these equations, the approach consists of keeping the terms of the first and second order in the four constitutive equations presented above. Doing so for sound propagation in a thermoviscous fluid leads for the continuity equation to [4]

$$\frac{\partial \rho'}{\partial t} + \rho_0 \boldsymbol{\nabla} \cdot \mathbf{v} = \frac{1}{\rho_0 c_0^4} \frac{\partial p^2}{\partial t} + \frac{1}{c_0^2} \frac{\partial \mathcal{L}}{\partial t}, \tag{12}$$

and for the momentum equation to

$$\rho_0 \frac{\partial \mathbf{v}}{\partial t} + \boldsymbol{\nabla} p = -\frac{1}{\rho_0 c_0^2}(\zeta + \tfrac{4}{3}\eta)\boldsymbol{\nabla}\frac{\partial p}{\partial t} - \boldsymbol{\nabla}\mathcal{L}, \tag{13}$$

where

$$\mathcal{L} = \frac{1}{2}\rho_0 v^2 - \frac{p^2}{2\rho_0 c_0^2} \tag{14}$$

is the second-order Lagrangian density. The entropy equation simplifies to

$$\rho_0 T_0 \frac{\partial s'}{\partial t} = \kappa \nabla^2 T, \tag{15}$$

where T_0 is the temperature of the medium at rest. After replacing the entropy in Eq. (3) by the expression given in Eq. (15) and using thermodynamics relations, the equation of state can be written [4]

$$\rho' = \frac{p}{c_0^2} - \frac{1}{\rho_0 c_0^4}\frac{B}{2A}p^2 - \frac{\kappa}{\rho_0 c_0^4}\left(\frac{1}{c_v} - \frac{1}{c_p}\right)\frac{\partial p}{\partial t}, \tag{16}$$

where c_v and c_p are the specific heat capacities at constant volume and pressure, respectively. Following the same procedure as presented in the previous section to obtain a lossless linear wave equation, the time derivative of Eq. (12) is subtracted to the divergence of Eq. (13) and Eq. (16) is used to eliminate ρ'. This leads to the second order wave equation [4]

$$\Box^2 p + \frac{\delta}{c_0^4}\frac{\partial^3 p}{\partial t^3} = -\frac{\beta}{\rho_0 c_0^4}\frac{\partial^2 p^2}{\partial t^2} - \left(\nabla^2 + \frac{1}{c_0^2}\frac{\partial^2}{\partial t^2}\right)\mathcal{L}, \tag{17}$$

where $\beta = 1 + B/(2A)$ is the coefficient of nonlinearity, $\Box^2$ is the d'Alembertian operator defined as

$$\Box^2 \equiv \nabla^2 - c_0^{-2}(\partial^2/\partial t^2), \tag{18}$$

and δ is the diffusivity of sound defined by

$$\delta = \frac{1}{\rho_0}\left(\frac{4}{3}\eta + \zeta\right) + \frac{\kappa}{\rho_0}\left(\frac{1}{c_v} - \frac{1}{c_p}\right). \tag{19}$$

Equation (17) is the second-order wave equation. From this equation, three widely used nonlinear wave equations can be derived: the Westervelt equation, the generalized Burgers' equation, and the Khokhlov-Zabolotskaya-Kuznetsov (KZK) equation.

The Westervelt (1963) equation describes diffraction, attenuation, and nonlinear effect of sound propagation and is written

$$\Box^2 p + \frac{\delta}{c_0^4}\frac{\partial^3 p}{\partial t^3} = -\frac{\beta}{\rho_0 c_0^4}\frac{\partial^2 p^2}{\partial t^2}. \tag{20}$$

The generalized Burgers' equation (1948) describes the nonlinear propagation for plane, cylindrical, and spherical waves, and is written

$$\frac{\partial p}{\partial r} + \frac{m}{r}p \mp \frac{\delta}{2c_0^3}\frac{\partial^2 p}{\partial \tau^2} = \pm\frac{\beta p}{\rho_0 c_0^3}\frac{\partial p}{\partial \tau}, \tag{21}$$

where the $\pm$ signs account for outgoing and incoming waves, r is the radial coordinate, $m = 0$, $1/2$, or 1 for plane, cylindrical, or spherical waves, respectively, and $\tau = t \mp (r - r_0)/c_0$ with r_0 the source or starting radius.

The KZK equation (1971) uses the parabolic approximation and is written

$$\frac{\partial^2 p}{\partial z \partial \tau} - \frac{c_0}{2}\nabla_\perp^2 p - \frac{\delta}{2c_0^3}\frac{\partial^3 p}{\partial \tau^3} = \frac{\beta}{2\rho_0 c_0^3}\frac{\partial^2 p^2}{\partial \tau^2}, \tag{22}$$

where $\tau = t - z/c_0$ for the outgoing wave, and $\nabla_\perp^2 = \partial^2/\partial x^2 + \partial^2/\partial y^2$ is a Laplacian that operates in the transverse plane, the plane perpendicular to the axis of the beam. All these formulations are approximations of the second-order nonlinear wave equation valid to the second order. They assume cumulative nonlinear effects dominate local nonlinear effects, they describe attenuation in a thermoviscous fluid, and they are valid for directive sources, that is $ka \gg 1$ where a is the distance characteristic of the source, and $k = 2\pi/\lambda$ with λ the typical wavelength [4]. Although these equations are widely used, they fail to describe some important situations like sound attenuation in the ocean floor and in biological tissues. Parts of this thesis (Papers III and IV) study variations of these equations to better describe frequency power law attenuation characteristic of complex media. Finding a solution to these equations involves numerical computation. Since most of the work done in this thesis uses numerical simulators it is appropriate to give a brief overview of some of the methods used for solving these equations.

1.2 Numerical simulators

Numerical methods for solving nonlinear wave propagation can follow three main paths. They can work in the time domain, in the frequency domain, or in a mix of time and frequency domains. There exists many simulators with many variations [9, 10]. We mention only four examples that are widely used and that have been used at some point in this thesis.

A simulator that solves the wave propagation in the time domain and that is based on the work done at the University of Bergen [11, 12] is called the Bergen Code [13]. It seeks a solution to a dimensionless version of the KZK equation in form of a Fourier series and actually computes the terms of this series. The version publicly available can model general two-dimensional (2D) sources and attenuation in a thermoviscous fluid. The Bergen Code was used during the elaboration of Paper I to compare its results against those provided by the simulator developed at the department. Although these comparisons were satisfactory, they are not shown in the published version of the article.

Another method that solves nonlinear propagation in the frequency domain and that is based on the operator splitting technique has been presented by Christopher and Parker [14, 15]. This method differs from the other three in that it does not solve a wave equation. Its background is more phenomenological. Christopher and Parker solve two effects. The first is the diffraction and attenuation of the wave when it propagates linearly, and the second is the nonlinear effects. It uses the angular spectrum approach to solve diffraction and solves a lossless form of the Burger's equation to take nonlinear effects into account. In this case, the operator splitting technique does not come from a wish to estimate all the terms in a wave equation but more to estimate simultaneously different physical effects. It is well adapted to simulate attenuation in media such as biological

tissue, but encounters limitations for wide band pulses due to its excessive computational burden in this case. An implementation of this method was developed at the department and used in Papers I and II [16].

A simulator that works in the time domain was first developed by Lee and Hamilton [17,18]. It solves the KZK equation and uses the operator splitting method. It was later updated by Cleveland *et al.* [19] who included multiple relaxation mechanisms to allow modeling of attenuation in non-thermoviscous media. The KZKTexas code [20], as it is called, models axisymmetric sources and was used in Papers I, II, and V. A version that solves the KZK equation in the case of general 2D sources has been developed [21, 22] but is not publicly available.

Finally, a simulator capable of simulating nonlinear sound propagation in heterogeneous and absorbing media was recently released under the GNU General Public License, version 3 [23]. Abersim [24–26] is a simulator based on the operator splitting method that solves the diffraction and attenuation operators in the frequency domain but solves the nonlinear operator in the time domain. It can model any transducer geometry, any power frequency law attenuation, and simulates heterogeneities by using phase shift screens. Abersim was used in Papers V and VII.

The result of these simulators can help identify the source of perturbations and the required corrections when measurements depart from the predictions of the models based on linear propagation. They can also predict how the signal is affected by nonlinear effects in order to take advantage of them.

1.3 Taking advantage of the effects of nonlinearity

When nonlinear effects are described by the second-order approximation, they translate to a distortion of the pulse as it propagates. The distortion of the pulse is due to an increased propagation speed compared to the small-signal sound speed where the medium is compressed, and a decreased propagation speed where the medium is stretched, causing the peaks of a periodic wave to travel faster than the troughs. This translates to energy transfers from the frequency band of the transmitted signal to the frequency bands around the upper harmonics of the transmitted center frequency (Fig. 1).

Nonlinear effects in sound propagation have found some applications. In the case of Tissue Harmonic Imaging (THI) in medical imaging, this energy transfer is used to create images by filtering the received echo in the second harmonic frequency band. This technique of second harmonic imaging based solely on the nonlinear propagation of sound in biological tissue enhances the image quality in many cases compared to imaging when filtering the signal in its transmitted frequency band [27] (Fig. 2).

Parametric sonars form another industrial application of nonlinear effects in sound propagation. It exploits the nonlinear interaction between two primary beams at slightly offset frequencies. This interaction generates signals at the sum and difference frequencies. The radiation at the difference frequency contains almost no sidelobes, has a high directionality, and can penetrate the ocean bottom due to a low attenuation at low frequency. Parametric sonars can be used for sub-bottom characterization and buried-object detection [28] (Fig. 3).

However, in some cases, as for target strength estimation in fishery research [29,30], the energy transfer from the transmitted frequency band to the upper harmonic frequency bands can be seen

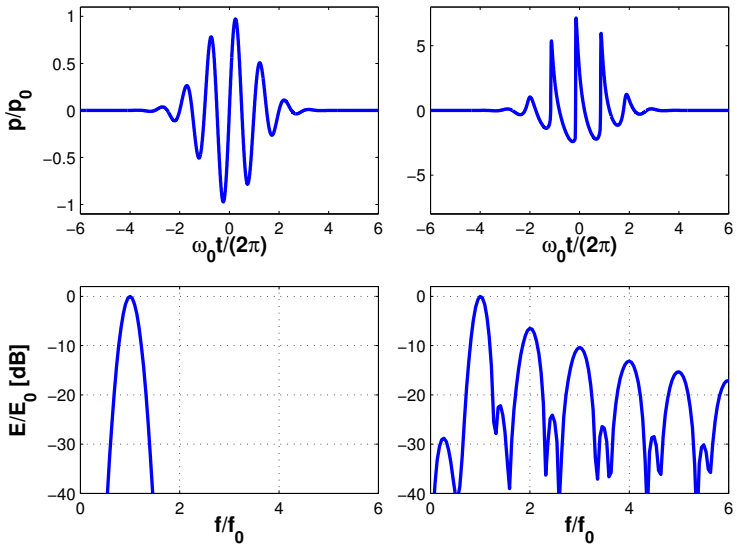

Fig. 1*: Signal's normalized pressure amplitude (top row) and normalized energy spectra (bottom row) at transmission (left column) and at focus point after nonlinear propagation through blood (right column). The transducer is a flat circular piston of radius 11 mm focused at 60 mm. The transmitted pulse has a center frequency of 1.2 MHz and an amplitude of 1.8 MPa.*

as detrimental since the signal loses energy from its transmitted frequency band. This duality in how the nonlinear effects in sound propagation are seen has been the motivator for this thesis.

1.4 The research question

The question that this thesis attempts to address is two-folded. The first part is: *"Can we utilize the effects of the nonlinear propagation of sound in areas where they are either ignored or avoided ?"*, and the second part is: *"Can we improve the models predicting the nonlinear propagation of sound ?"*. These questions are fairly open. The work in this thesis has limited the fields of investigation to underwater acoustics and medical ultrasound imaging although some of the theoretical studies can be applied to wider areas.

1.5 The research method

A natural starting point to investigate new ways of using the nonlinear propagation of sound is to look into areas where these effects are either avoided or neglected and investigate if one can use them in a similar way as other technologies have successfully done. This was the method used when investigating the possibility for second harmonic imaging with echo sounders as it is done in medical harmonic imaging. Another path that this work has followed consists of studying a technology and check how it could be improved when making use of the nonlinear effects. This lead to the studies on acoustic Doppler current profilers and on multi-line transmission method in

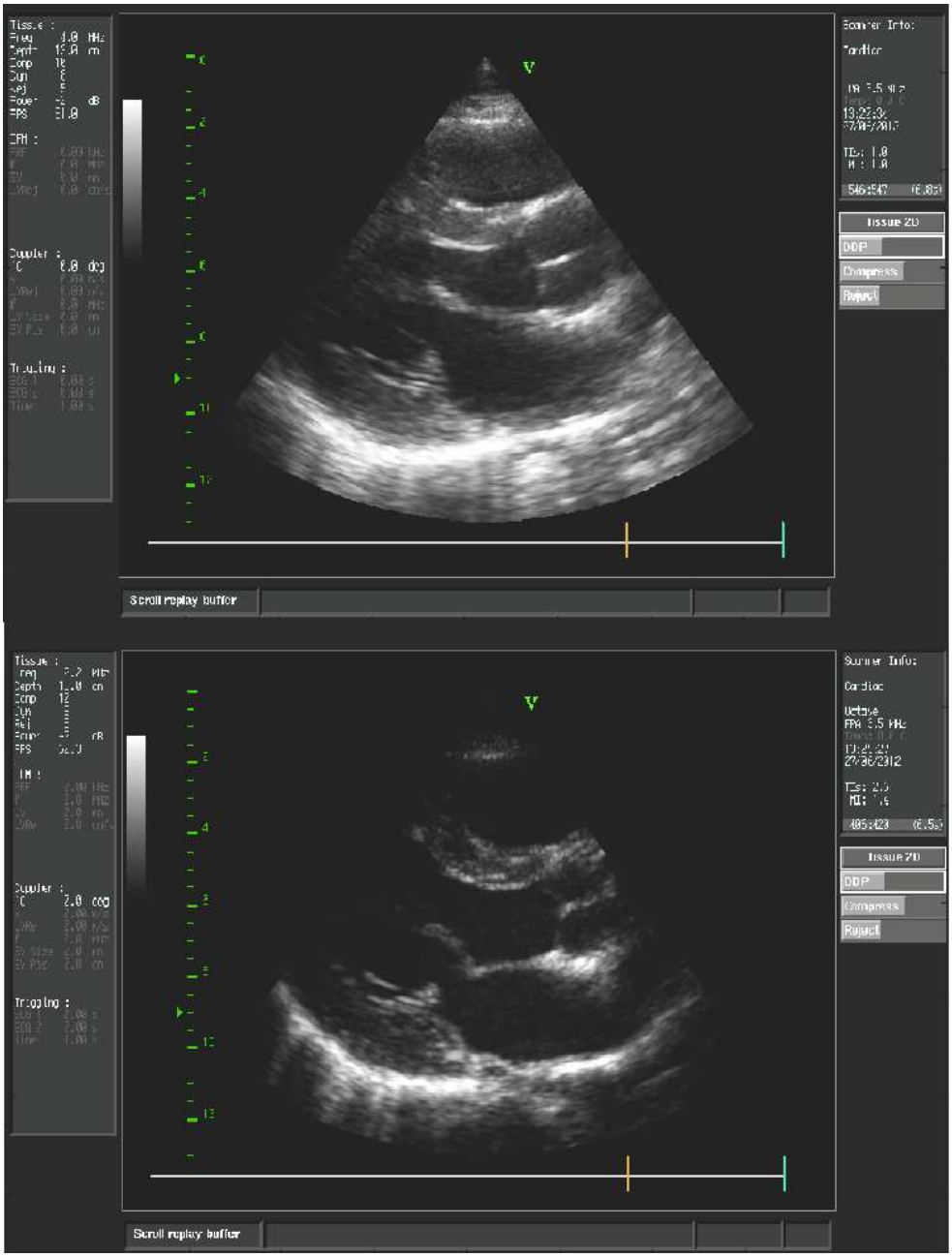

Fig. 2: *Ultrasound image of a human heart (parasternal view) using fundamental imaging (top) with a transmitted pulse of center frequency 4.0 MHz and harmonic imaging (bottom) with a transmitted pulse of center frequency 2.2 MHz. The depth of view is 13 cm and the focus is at 9 cm. The noise is reduced and the border of the heart walls and the mitral valve are more clearly delimited in the case of harmonic imaging.*

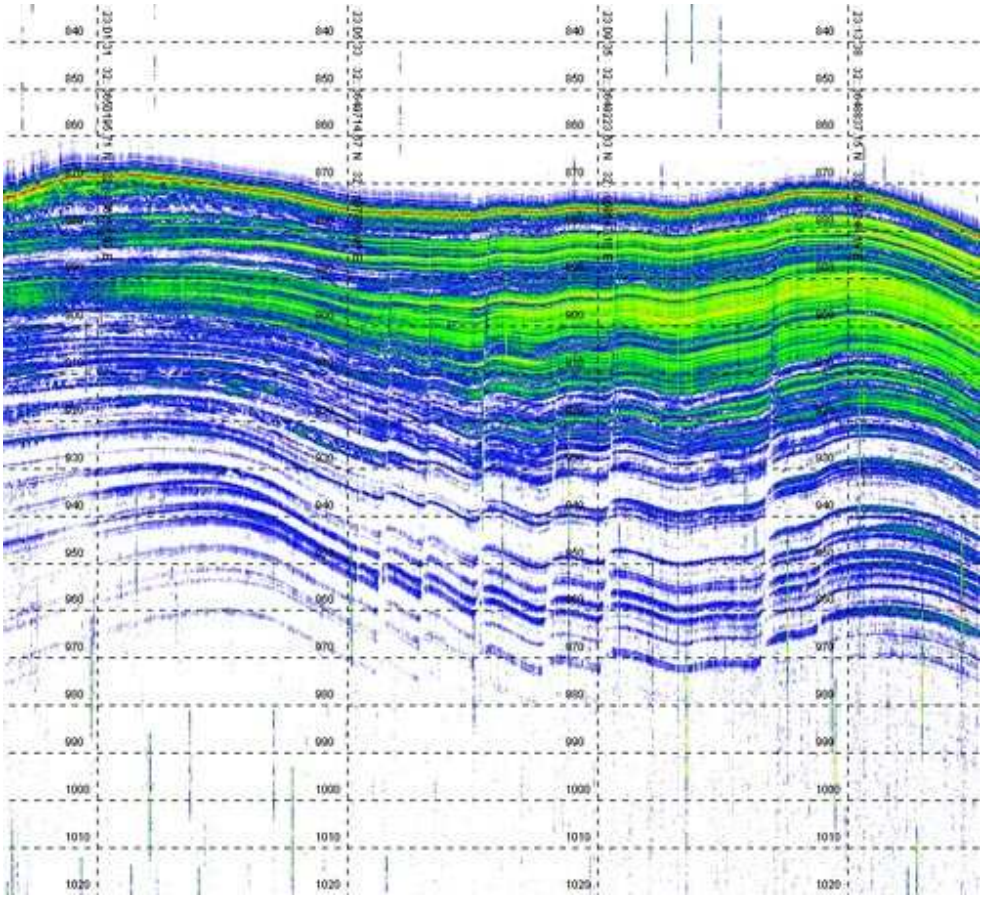

Fig. 3: *Image showing faults in sediment obtained by the TOPAS PS 18 sub-bottom profiler manufactured by Kongsberg Maritime. The penetration is above 100 m and the water depth is around 870 m (source: Kongsberg Maritime).*

medical imaging.

After an extensive use of the state-of-the-art simulators publically available for predicting nonlinear propagation of sound, the development of our own simulator, and equipped with an overview of their strengths and limitations, a natural extension was to check if alternative models could be found to predict nonlinear effects. The results that emerged from this are a combination of new theoretical models and numerical methods backed up, in part, by measurements either done in the past and reported in the literature, or realized during this thesis.

1.6 Justification of the work

The study of nonlinear effects in sound propagation has blossomed in the last sixty years due to the appearance of computers powerful enough to find numerical solutions for the established wave equations [31]. New disciplines have emerged such as high intensity focused ultrasound (HIFU) in medicine [32] involving acoustic signals strongly affected by nonlinear effects. This in turn has stimulated some efforts to better predict nonlinearity in sound propagation. Despite this access to better knowledge, nonlinear effects are still avoided or neglected in some domains. There is therefore a clear opportunity in these fields for a research study on the use of the nonlinear effects in sound propagation and their combination with existing technologies.

As previously mentioned, there exists many tools that numerically solve the nonlinear wave equations with their own strength and limitations. The numerical simulators and models available can be improved to either describe more accurately the measurements or to increase their efficiency.

The research presented in this thesis uncovers new potential ways of using nonlinear sound propagation. It also complements the theoretical and numerical models for nonlinear propagation. With domains of application as large and complex as underwater acoustics and medical imaging, the nonlinear propagation of sound deserves the attention of the scientific community. Impacts such as better diagnostics for patients and a more efficient use of our natural resources are hopefully some results of the research in this field.

Chapter 2

Summary of publications

2.1 Paper I

"Feasibility of second harmonic imaging in active sonar: measurements and simulations"
IEEE Journal of Oceanic Engineering, Accepted for publication May 2, 2012.

In this paper, we investigate the feasibility of using the second harmonic signal generated by nonlinear propagation in water for pulse-echo imaging with an echo sounder. Two transducers of center frequency 120 kHz and 200 kHz were used together with an EK 60 scientific echo sounder (Kongsgerg Maritime, Horten, Norway). By comparing our simulations to measurements of the axial and lateral profiles when the signal is filtered around the harmonic frequency bands after free propagation in water, we verify the correct implementation of our simulator. The measurements confirm the characteristic narrower main lobe and lower sidelobes of the upper harmonic signals compared to the fundamental signal. A comparison of pulse-echo imaging when using the fundamental and second harmonic signals with calibration spheres as reflectors reveals that one sphere could only be detected by the second harmonic signal. Since the amplitude of the second harmonic signal generated by nonlinear propagation is much lower than the amplitude of the signal around the fundamental frequency band, the maximum attainable ranges for both signals have to be evaluated. These ranges are estimated using simulations of both signals at long range combined with sonar budget equations. As expected, the maximum range of the second harmonic is lower than the range of the fundamental signal, but given its imaging capabilities, the second harmonic signal has a potential use in sonar applications when combined with the fundamental signal.

2.2 Paper II

"Theoretical improvements when using the second harmonic signal in acoustic Doppler current profilers"
IEEE Journal of Oceanic Engineering, Revised version submitted June 11, 2012.

This article presents how the use of the second harmonic signal in acoustic Doppler current profilers (ADCPs) can improve the performance when measuring ship velocity or current speed. The geometry of the second harmonic beam improves the determination of the time of arrival of the

pulse and decreases the velocity spread. Additionally, the velocity estimates obtained by combining the fundamental and second harmonic signals can exhibit a lower variance than the estimate given by the fundamental signal only. These properties are verified in the case of incoherent, coherent, and broadband echo processing. As in the previous paper, the maximum attainable ranges for the second harmonic and fundamental signals are evaluated. These ranges are estimated for the fundamental signal of frequency f_0 = 153.6 kHz, the second harmonic signal of frequency $2f_0$, and the fundamental signal of a typical transducer transmitting at the frequency $2f_0$. The results show that the range for the second harmonic signal is comparable to the range of a typical transducer transmitting at the same frequency. This paper shows that the combined use of the fundamental and second harmonic signals can improve the velocity estimate from ADCPs based on three main processing methods.

2.3 Papers III and IV

"Nonlinear acoustic wave equations with fractional loss operators"
Journal of the Acoustical Society of America, vol. 130, no. 3, pp. 1125-1132, September 2011.

"A more fundamental approach to the derivation of nonlinear acoustic wave equations with fractional loss operators"
Journal of the Acoustical Society of America, Revised version submitted June 15, 2012.

These two papers show a theoretical derivation of a nonlinear wave equation with fractional derivatives. The aim is to derive a nonlinear wave equation that leads to frequency laws for attenuation and dispersion describing adequately the measurements in complex media such as biological tissues or the ocean bottom layers. In contrast with some articles where the loss operator in the wave equation is modified ad-hoc, the presented papers take an alternative form of the constitutive equations as a starting point. New physical models described by a stress-strain relation and a heat flux equation with fractional derivatives or fractional integrals are presented. They lead to a fractional version of the Navier-Stokes equation and, in the first paper, to a fractional version of the entropy equation. However, the second paper reveals that the derivation of the entropy equation cannot be obtained rigorously. Instead of using the entropy equation to get to a nonlinear fractional wave equation, it establishes a fractional relation between density and pressure using thermodynamic arguments. The nonlinear fractional wave equation obtained in the second paper differs slightly from the equation presented in the first paper, but lead to similar expressions for the attenuation and dispersion as functions of the frequency. These papers show that a nonlinear fractional wave equation not only describes appropriately the frequency power laws for attenuation and dispersion when sound propagates in complex media, but also that the origin of the fractional derivatives can be traced back to the constitutive equations when using adapted physical models.

2.4 Paper V

"Fast simulation of second harmonic ultrasound field using a quasi-linear method"
Journal of the Acoustical Society of America, vol. 131, no. 6, pp. 4365-4375, June 2012.

This paper presents a numerical simulator based on the quasi-linear approximation and evaluates its performance. The simulator aims at providing an estimate of the amplitude and spatial distribution of the fundamental and second harmonic signals in the case of medical ultrasound imaging. The theory shows that no stepwise propagation from the source to the depth of interest is required, making the simulator fast and adapted when quick computation is needed. A comparison of the axial and lateral profiles of the fundamental and second harmonic signals with the results given by the KZKTexas code and Abersim as well as measurements of the sound field generated by a medical probe in water validate the simulator. The speed performance of the simulator is evaluated against the KZKTexas code, and Abersim. It shows that the presented simulator is the faster. To conclude, this paper shows that if the assumptions of quasi-linearity and propagation in a homogeneous medium are satisfied, the simulator could be a fast alternative for estimating the fundamental and second harmonic pressure amplitudes and spatial distributions in medical imaging applications.

2.5 Paper VI

"3D simulation of parametric ultrasound fields"
Proceedings of the 19th International Symposium on Nonlinear Acoustics, Tokyo, Japan, May 2012.

In this paper, a variation of the quasi-linear simulator presented in paper V is applied to parametric arrays that use the nonlinear interaction between two primary beams transmitted at slightly different frequencies to generate signals at the sum and the difference of these frequencies. The axial and radial profiles of the signals at both the sum and the difference frequencies are simulated and the results are compared to the results of two analytical formulations that compare favorably to past measurements. The article concludes that the presented simulator does not have the restrictions on the source geometry that the analytical methods have and that it allows for more flexibility. In this case too, if the assumptions of quasi-linearity and propagation in a homogeneous medium are satisfied, this simulator could be used to predict the signals generated by parametric arrays. An extended version of the paper included in the proceedings of the 19*th* International Symposium on Nonlinear Acoustics is presented in this thesis to make the paper self-contained and easier to understand for the reader.

2.6 Paper VII

"Multi-Line Transmission in medical imaging using the second harmonic signal"
IEEE Transactions on Ultrasonics, Ferroelectrics, and Frequency Control, Submitted July 4, 2012.

An alternative technique to increase the image frame rate in medical imaging is applied to the second harmonic signal in this paper. The technique called multi-line transmission (MLT) consists of transmitting at the same time several pulses in separate directions thereby reducing the number of needed transmissions to cover a predefined angular sector and increasing the frame rate. A theoretical study using an adapted version of the quasi-linear simulator shows that when using the

second harmonic signal, the perturbations at reception due to the echo of edge waves generated by pulses transmitted in different directions are lower than when using the fundamental signal. These results are confirmed by measurements using a cardiac probe transmitting at 1.5 MHz and imaging a wire target immersed in anti-freezing additive. The conclusion of the paper is that there is a potential improvement in image quality when using the second harmonic signal in conjunction with the MLT technique.

Chapter 3

Discussions and future work

3.1 Discussions

The main contributions of this thesis are:

- Experimental data showing the feasibility of second harmonic imaging with echo sounders and improved imaging capability for the second harmonic signal compared to the fundamental signal.
- Theoretical studies of the range performance when using the second harmonic signal with echo sounders and acoustic Doppler current profilers.
- Study of the potential improvements in the velocity estimates when using the second harmonic signal in acoustic Doppler current profilers.
- Theoretical and experimental study of the potential reduction of perturbations in multi-line transmission method when using the second harmonic signal in medical imaging.
- Derivation from constitutive equations of a nonlinear wave equation that can describe the attenuation and dispersion observed in complex media with the use of fractional derivatives.
- Implementation of a numerical simulator based on the quasi-linear approximation and comparison of its speed and accuracy against measurements and recognized state-of-the-art simulators for medical imaging applications.
- Short evaluation of simulations of parametric radiations using a numerical simulator based on the quasi-linear approximation against analytical solutions.

3.1.1 Out in the "real world"

During this thesis, a number of experiments were carried out at Kongsberg Maritime facility in Horten, Norway, and at the Department of Circulation and Medical imaging of the Norwegian University of Science and Technology, in Trondheim, Norway. In all experiments, the measurements of the sound field created by the scientific echo sounder (Paper I) and by the medical probe (Papers V and VII) showed a fairly good match with the results of the numerical simulations. This increases the confidence in the model on which the simulators are based. During the measurements

using echo sounders, it was a positive surprise to see the results of pulse-echo imaging using the sphere as targets. The results as presented in Paper I did not appear as the signals were acquired. Each quadrant of the transducer was connected to one channel of the oscilloscope, and it was only after processing the data from all four quadrants and combining the results that the echo from the smallest sphere appeared so clearly when using the second harmonic signal while it was drowned by the echo from the tank wall when using the fundamental signal.

An experiment that was not reported in any article consisted of using the EK 60 scientific echo sounder in dual-frequency mode where two channels were used. The first channel was driving an ES120-7C transducer emitting a pulse at 120 kHz and the second was connected to an ES200-7C transducer that was muted (not transmitting). Both transducers were positioned side by side and scanned an angular sector of approximately $\pm$ 30° in which several calibration spheres were placed at about 3 m from the source. The echo from the fundamental signal centered around 120 kHz was recorded by the ES120-7C transducer and was displayed in the upper half of the echogram view, while the signal filtered around 200 kHz mostly coming from the second harmonic signal was recorded by the ES200-7C transducer and displayed in the lower half of the echogram view. Although clear echoes from the calibration spheres were seen in both views, it was difficult to quantify the resolution performance in each case. This could be due to the signal processing done by the acquisition electronics and software. Unfortunately, we could not draw any clear conclusions from this experiment although this is our closest attempt to what combined fundamental and second harmonic imaging could be using an echo sounder.

During the experiments conducted to back up the simulations presented in Paper VII, we had to estimate the frequency response of the probe we used in order to carefully choose the center frequency and the bandwidth of the transmitted signal. If the transmit frequency was chosen close to the center frequency of the probe, it allowed a high signal amplitude and a high signal-to-noise ratio but the sensitivity of the probe in the second harmonic frequency band would be too low. The choice was, therefore, a trade-off between a frequency low enough to record the part of the signal in the second harmonic frequency band without too much attenuation or distortion, but close enough to the probe's center frequency to maximize the transmitted power and the signal-to-noise ratio. These experiments were the first opportunity to work with a transducer array with a large bandwidth, at least compared to the transducers used when experimenting with echo sounders. It also gave us the chance to implement and work with a delay-and-sum beamformer. We were able after that to put in perspective the requirements and performance of the transducers and data acquisition in underwater acoustics against medical imaging.

3.1.2 Range performance estimation

When evaluating the maximum attainable range for the fundamental and second harmonic signal for sonar application, we noticed that the results were fairly sensitive to simulation parameters such as the receiver bandwidth and the volume scattering strength. It is therefore of prime importance to get a precise knowledge of the system setup and the environmental conditions when estimating maximum ranges in order to get trustworthy results. As justly pointed out by one of the anonymous reviewers, "statement of maximum detection ranges is meaningless without statement of the applicable frequencies, assumed target strength, and other factors defining the conditions". The results obtained for the maximum ranges were reviewed by our collaborators at Kongsberg Maritime and

found in line with what is experienced in practice in similar operating conditions.

In the case of acoustic Doppler current profilers (ADCPs), the computation of the maximum attainable range was inspired by the equations presented in Urick's book [33] but it does not use a sonar budget equation as in the case of echo sounders. To the authors' knowledge, this is new to the literature. For this study too, the results for the obtained maximun ranges were reviewed by our collaborator at Nortek AS and found in line with what can be expected from comparable products in the industry.

It should be noted that the volume scattering strength plays a different role in the context of echo sounders and ADCPs. For echo sounders, volume reverberation is only a source of perturbation that decreases the signal to noise ratio while for the ADCP it has two ambivalent contributions. When measuring currents speed, the volume reverberation is the source of the signal analyzed. If the volume scattering strength is high, it increases the signal to noise ratio but limits the maximum range, and if it is low the signal to noise ratio is weaker but the maximum range is increased. For detection at short range, a high volume scattering strength is beneficial, whereas if large attainable range is an objective, a low volume scattering strength is preferable.

3.1.3 A quasi-linear simulator

We use the quasi-linear approximation in Papers V and VI as well as in the simulations of Paper VII . The theory of quasi-linearity is not new, the innovative parts lies in the formulation of the solutions to the quasi-linear approximation. By analytically performing an integration along the propagation direction, we remove the need for a stepwise integration from the source plane to the depth of interest. A triple integral in the frequency domain is all that needs to be computed. It is independent of the depth of interest. The use of the beampattern at focus in order to easily compute the Fourier transform in the source plane contribute to get a fast simulator. The use of a "virtual" focus plane for one-dimensional (1D) arrays with different azimuth and elevation foci is another technique that was implemented. The setup for the measurements of the sound field created by a medical probe in water and presented in Paper V was chosen so that all these techniques were tested. The match between measurements and simulations was surprisingly good.

When a similar simulator is used for estimating parametric radiations, the calculations become indirectly dependent on the depth of interest. Indeed, the extent of the frequency domain on which the triple integral is computed has to be taken large enough to avoid perturbations from aliasing due to the discrete Fourier transform. The size of this domain and the number of operations needed increase with the square of the depth of interest for a given opening angle. The situation is different in the case of medical imaging where the beam is focused. So the simulator's advantage does not lie in its speed but more in its flexibility of use compared to the analytical solutions. In addition, during the comparisons of the methods, we witnessed that the analytical solutions where solved fairly fast using today's computing power and the built-in algorithms in MATLAB® (version 2011a, The MathWorks, Natick, MA). That might not have been the case when the solutions were first established (at least one of them).

3.1.4 Establishing a new model

From simulations that can be verified by measurements in Papers I, II, V, VI, and VII, we worked in Papers III and IV on a theory that could describe measurements. Obtaining a fractional nonlinear wave equation was harder than first anticipated. We are, in this regard, grateful to Dr. Gregory Vilenskiy who, during a seminar, pointed out some imprecisions in Paper III that lead to Paper IV. In Paper IV, all the equations were meticulously derived to keep the validity to the second order. This is what led us away from the entropy equation and towards a direct formulation of the density as a function of pressure using fractional derivatives.

In contrast with the papers describing simulations, the results of these papers are harder to be verified by measurements since they constitute the starting point of the method. Indeed, in that case the scientific method consists of tracing back the origin of the observed attenuation and dispersion to the correct physical models that appropriately describe them. The outcome is therefore a bit more uncertain albeit very satisfactory to the mind.

3.2 Future work

An obvious follow-up for the potential use of the second harmonic signal with echo sounders and acoustic Doppler current profilers would be trials at sea. Experiments in a real environment could confirm the potential imaging improvements and the estimates of the maximum attainable range. Measurements in shallow water where the range is traditionally limited by reverberation from the sea surface and ocean bottom could reveal an improved range when using the second harmonic signal with a narrow main lobe.

The numerical simulator based on quasi-linearity could also be tried successively, where the output of one simulation is the input to the next. For each simulation, the parameters of the medium can vary and allow a modeling of a medium made of homogeneous layers. This solution would be particularly adapted to model the inhomogeneities of the ocean's sub-bottom that can easily be modeled by layers of different nature with different properties for the propagation of sound.

In more complicated applications such as fishery sonars or multi-beam echo sounders, improvements in the obtained image similar to what was shown during our experiments with an echo sounder should be possible when using the second harmonic signal. Each beam of a multi-beam echo sounder would exhibit a narrower main lobe and higher main-lobe-to-sidelobe ratio. The obtained image after beamforming should therefore have a better resolution. It should also suffer from less perturbation due to volume reverberation, or echoes from the sea-bottom coming from the direction of the sidelobes.

In applications such as sonar imaging and underwater communcation, wide bandwidth signals are often used to offer either good range resolution or large signal-to-noise ratio. With the emergence of very wide band transducers [34] it becomes necessary to consider the frequency dependent distortion of those signals that cover a large range of frequencies. The part of the signal containing higher frequencies is more attenuated due to higher absorption and greater nonlinear losses than the part with low frequencies. A pre-conditioning of the signal at transmission could be investigated to compensate for this and ensure that the desired signal reaches the target. A better match-filtering could also be obtained when the nonlinear distortions of the received signal are taken into account.

This technique is used in applications using the nonlinear propagation of sound in air to create parametric audio sources [35, 36].

A research theme that was started but did not come to fulfillment due to lack of resources is about the finite element modeling (FEM) of sound propagation using the fractional forms of constitutive equations. With FEM no wave propagation equation is necessary. The constitutive equations based on the chosen physical models describe the propagation medium and all physical quantities such as density, particle speed, temperature, and pressure are computed in the entire medium as a defined perturbation is applied at some place and time. Such modeling, though very computer intensive, does not involve all the approximations done for getting to a nonlinear wave equation and can give more correct estimates. In addition, since a model for heat transfer is used, the evolution of the temperature in the medium is given during the simulation for the sound propagation. Traditionally, the modeling of temperature increase due to sound propagation for applications such as hyperthermia [37] and high intensity focused ultrasound (HIFU) [38, 39] is done in two stages. The sound propagation is first simulated, and the temperature evolution is then deduced from the local heat sources generated by the sound propagation with the help of the bio-heat transfer equation. Using FEM would also accommodate fairly easily the formulations of different physical models to describe the stress-strain relation and heat transfer. The challenge in this method would be to properly implement a description of the fractional derivative and integral. Had this implementation been completed, it would have been interesting to see how the results compare to the results given by the simulators described in Ch. 1.

Bibliography

[1] S. Earnshaw, "On the Mathematical Theory of Sound.[Abstract]," *Royal Society of London Proceedings Series I*, vol. 9, pp. 590–591, 1857.

[2] P. J. Westervelt, "Parametric acoustic array," *J. Acoust. Soc. Am.*, vol. 35, no. 4, pp. 535–537, Apr. 1963.

[3] H. O. Berktay, "Possible exploitation of non-linear acoustics in underwater transmitting applications," *J. Sound Vib.*, vol. 2, no. 4, 1965.

[4] M. F. Hamilton and C. L. Morfey, "Model equations," in *Nonlinear Acoustics*, M. F. Hamilton and D. T. Blackstock, Eds. San Diego: Academic Press, Dec. 1998, ch. 3, pp. 41–63.

[5] L. D. Landau and E. M. Lifshitz, "Viscous fluids," in *Fluid Mechanics*, 2nd ed., ser. Course of theoretical physics. Oxford, England: Pergamon Press, 1987, vol. 6, ch. 2, pp. 44–48.

[6] R. T. Beyer, "The parameter B/A," in *Nonlinear Acoustics*, M. F. Hamilton and D. T. Blackstock, Eds. San Diego: Academic Press, Dec. 1998, ch. 2, pp. 25–39.

[7] B. O. Enflo and C. M. Hedberg, "Physical theory of nonlinear acoustics," in *Theory of Nonlinear Acoustics in Fluids*, ser. Fluid mechanics and its applications. New York: Kluwer academic publishers, 2002, vol. 67, ch. 2, pp. 13–24.

[8] L. E. Kinsler, A. R. Frey, A. B. Coppens, and J. V. Sanders, "The acoustic wave equation and simple solutions," in *Fundamentals of Acoustics*, 4th ed. New York: John Wiley and Sons, Inc., 2000, ch. 5, pp. 113–148.

[9] J. H. Gingsberg and M. F. Hamilton, "Computational methods," in *Nonlinear Acoustics*, M. F. Hamilton and D. T. Blackstock, Eds. San Diego: Academic Press, Dec. 1998, ch. 11, pp. 309–341.

[10] M. D. Verweij and J. Huijssen, "Computational methods for nonlinear acoustic wavefields in homogeneous media," in *Computational Methods in Nonlinear Acoustics: Current Trends*, ser. Special Review Books in Physical Sciences, C. Vanhille and C. Campos-Pozuelo, Eds. Kerala, India: Research Signpost, 2011, ch. 1, pp. 1–19.

[11] S. I. Aanonsen, T. Barkve, J. Naze Tjøtta, and S. Tjøtta, "Distortion and harmonic generation in the nearfield of a finite amplitude sound beam," *J. Acoust. Soc. Am.*, vol. 75, no. 3, pp. 749–768, Mar. 1984.

[12] M. F. Hamilton, J. Naze Tjøtta, and S. Tjøtta, "Nonlinear effects in the farfield of a directive sound source," *J. Acoust. Soc. Am.*, vol. 78, pp. 202–216, Feb. 1985.

[13] J. Berntsen, "Numerical calculations of finite amplitude sound beams," in *Frontiers of Nonlinear Acoustics: Proc. 12th International Symposium on Nonlinear Acoustics*, M. F. Hamilton and D. T. Blackstock, Eds., Aug. 1990, pp. 191–196.

[14] P. T. Christopher and K. J. Parker, "New approaches to the linear propagation of acoustic fields," *J. Acoust. Soc. Am.*, vol. 90, no. 1, pp. 507–521, Jul. 1991.

[15] ——, "New approaches to nonlinear diffractive field propagation," *J. Acoust. Soc. Am.*, vol. 90, no. 1, pp. 488–499, Jul. 1991.

[16] J. F. Synnevåg and S. Holm, "Non-linear propagation of limited diffraction beams," in *Proc. IEEE Ultrason. Symp.*, Sendai, Japan, Oct. 1998, pp. 1885–1888.

[17] Y. S. Lee and M. F. Hamilton, "Time-domain modeling of pulsed finite-amplitude sound beams," *J. Acoust. Soc. Am.*, vol. 97, pp. 906–917, 1995.

[18] Y. S. Lee, "Numerical solution of the KZK equation for pulsed finite amplitude sound beams in thermoviscous fluids," Ph.D. dissertation, The University of Texas at Austin, Dec. 1993.

[19] R. O. Cleveland, M. F. Hamilton, and D. T. Blackstock, "Time-domain modeling of finite-amplitude sound in relaxing fluids," *J. Acoust. Soc. Am.*, vol. 99, no. 6, pp. 3312–3318, Jun. 1996.

[20] Y. S. Lee, R. Cleveland, and M. F. Hamilton, "KZKTexas," http://people.bu.edu/robinc/kzk/, date last viewed May 30, 2012, Oct. 1998.

[21] X. Yang and R. O. Cleveland, "Time domain simulation of nonlinear acoustic beams generated by rectangular pistons with application to harmonic imaging," *J. Acoust. Soc. Am.*, vol. 117, no. 1, pp. 113–123, Jan. 2005.

[22] Y. Jing and R. O. Cleveland, "Modeling the propagation of nonlinear three-dimensional acoustic beams in inhomogeneous media," *J. Acoust. Soc. Am.*, vol. 122, no. 3, pp. 1352–1364, Sep. 2007.

[23] "GNU General Public License," http://www.gnu.org/copyleft/gpl.html, date last viewed May 30, 2012, Jun. 2007.

[24] T. Varslot and G. Taraldsen, "Computer simulation of forward wave propagation in soft tissue," *IEEE Trans. Ultrason. Ferroelectr. Freq. Control*, vol. 52, no. 9, pp. 1473–1482, Sep. 2005.

[25] T. Varslot and S. E. Måsøy, "Forward propagation of acoustic pressure pulses in 3D soft biological tissue," *Model. Identif. Contr.*, vol. 27, no. 3, pp. 181–200, Jul. 2006.

[26] M. E. Frijlink, H. Kaupang, T. Varslot, and S. E. Måsøy, "Abersim: A simulation program for 3D nonlinear acoustic wave propagation for arbitrary pulses and arbitrary transducer geometries," in *Proc. IEEE Ultrason. Symp. 2008*. Beijing, China: IEEE, Nov. 2008, pp. 1282–1285.

[27] F. A. Duck, "Nonlinear acoustics in diagnostic ultrasound," *Ultrasound Med. Biol.*, vol. 28, no. 1, pp. 1–18, Jan. 2002.

[28] A. Trucco, "Detection of objects buried in the seafloor by a pattern-recognition approach," *IEEE J. Oceanic Eng.*, vol. 26, no. 4, pp. 769–782, Oct. 2001.

[29] F. E. Tichy, H. Solli, and H. Klaveness, "Non-linear effects in a 200-kHz sound beam and the consequences for target-strength measurement," *ICES J. Mar. Sci.*, vol. 60, no. 3, pp. 571–574, 2003.

[30] A. Pedersen, "Effects of nonlinear sound propagation in fisheries research," Ph.D. dissertation, University of Bergen, Department of Physics and Technology, Mar. 2007.

[31] L. Bjørnø, "Forty years of nonlinear ultrasound," *Ultrasonics*, vol. 40, pp. 11–17, 2002.

[32] M. R. Bailey, V. A. Khokhlova, O. A. Sapozhnikov, S. G. Kargl, and L. A. Crum, "Physical mechanisms of the therapeutic effect of ultrasound (a review)," *Acoust. Phys.*, vol. 49, no. 4, pp. 369–388, 2003.

[33] R. J. Urick, *Principles of underwater sound*, 3rd ed. McGraw-Hill Book Company, 1983.

[34] B. Horvei and K. E. Nilsen, "A new high resolution wideband multibeam echo sounder for inspection work and hydrographic mapping," in *Proc. OCEANS MTS/IEEE 2010*, Seattle, WA, Sep. 2010, pp. 1–7.

[35] M. Yoneyama, J. Fujimoto, Y. Kawamo, and S. Sasabe, "The audio spotlight: An application of nonlinear interaction of sound waves to a new type of loudspeaker design," *J. Acoust. Soc. Am.*, vol. 73, pp. 1532–1536, May 1983.

[36] T. D. Kite, J. T. Post, and M. F. Hamilton, "Parametric array in air: Distortion reduction by preprocessing," in *Proc. 16th Int. Cong. Acoust.*, vol. 2, Seattle, WA, Jun. 1998, pp. 1091–1092.

[37] R. J. Lalonde, A. Worthington, and J. W. Hunt, "Modelling temperature distributions produced by ultrasound phased arrays for hyperthermia," in *Proc. IEEE Ultrason. Symp. 1989*. Montreal, Canada: IEEE, Oct. 1989, pp. 941–944.

[38] I. M. Hallaj and R. O. Cleveland, "FDTD simulation of finite-amplitude pressure and temperature fields for biomedical ultrasound," *J. Acoust. Soc. Am.*, vol. 105, pp. 7–12, May 1999.

[39] E. A. Filonenko and V. A. Khokhlova, "Effects of acoustic nonlinearity on heating of biological tissue induced by high intensity focused ultrasound," *Acoust. Phys.*, vol. 47, pp. 541–549, 2001.

Paper I

Feasibility of second harmonic imaging in active sonar: measurements and simulations

F. Prieur, S. P. Näsholm, A. Austeng, F. Tichy, and S. Holm

IEEE Journal of Oceanic Engineering, Accepted for publication May 2, 2012.

Feasibility of second harmonic imaging in active sonar: measurements and simulations

F. Prieur, Sven Peter Näsholm, A. Austeng, F. Tichy, and S. Holm

Abstract— Nonlinear acoustics allows for applications like tissue harmonic imaging in medicine and parametric arrays in underwater acoustics. Mainstream sonars transmit and receive signals at the same frequency and up to now energy transferred to higher harmonic frequencies has been mainly seen as a disturbance for target strength estimation, e.g., in fishery research. This paper investigates the feasibility of utilizing the part of the signal generated around the second harmonic frequency band by nonlinear propagation of sound in water. It presents the potential enhancements the second harmonic signal may provide for target imaging as well as multi-frequency target recognition. It compares measurements of the pressure field radiated by commercial transducers in water at 121 kHz and 200 kHz up to a range of 12 m with numerical simulations. The detected levels of higher harmonic signals agree with simulations of nonlinear wave propagation. This verifies the implementation of the simulator and allows a comparison of the beam characteristics at longer ranges when filtered around the fundamental or second harmonic frequencies. An example of pulse-echo imaging with spherical targets is also shown using signals at the fundamental and second harmonic frequencies where the second harmonic signal can detect one of the targets that the fundamental signal cannot. Using the active sonar equation to estimate the maximum range, simulations based on a simple model including ambient noise and volume reverberation confirm that with a source level of 228 dB and a detection threshold of 12 dB the fundamental signal at 200 kHz can detect a fish of target strength -36 dB to approximately 343 m while the detection range of the second harmonic signal is approximately 243 m. The combined use of the signal components in the second harmonic and fundamental frequency bands provides a high resolution image at short range and a long range imaging capability at a lower resolution as well as a multi-frequency characterization of targets.

I. Introduction

In most sonar applications the received signal is traditionally filtered around the transmit center frequency at reception. The energy transferred to different frequency bands due to nonlinear sound propagation effects is not used. But the signal generated in these different frequency bands has features that can potentially improve target imaging. An application that found a use for nonlinear propagation is the parametric sonar. In 1963 Westervelt [1] predicted that when transmitting two high-frequency beams at slightly offset frequencies the beams would interact due to nonlinear effects and the wave generated from this interaction would propagate at the sum and difference of the transmitted frequencies, the signal at the difference frequency being the more applicable. Berktay [2] further developed this theory and evaluated several possible applications of nonlinearity in underwater transmitting applications. As an implementation of this, the parametric sonar is a technology that exploits nonlinear propagation in underwater acoustics. It is an industrial product that helps sub-bottom characterization [3] and buried object detection [4] thanks to the directional low frequency beam, its long range, and bottom penetration capability. In his review, Bjørnø [5] describes the characteristics and the performance of the parametric sonar.

About fifteen years ago, use of nonlinear propagation of sound also reached the field of medical ultrasound with the development of tissue harmonic imaging (THI). In THI the image reconstruction is made from receiving signals in the second harmonic frequency band. In many clinical applications, THI results in enhanced image quality compared to reconstructing the image from echoes in the transmitted frequency band. Duck [6] presents a comprehensive review explaining why THI allows for better image quality. It is due to, among others, a narrower main lobe, a better main-lobe-to-sidelobe ratio, and limited reverberation for the second harmonic signal compared to the fundamental signal. THI is implemented in most commercial scanners and is often the default imaging mode for cardiology where it has been shown to improve endocardial border definition [7, 8] and measurements of heart functions [9]. THI has also shown promising image improvements for, e.g., liver [10] and kidney [11] examination.

In sonar applications recent papers in the fishery research field have reported the problem that energy transfer to higher harmonic frequencies creates for accurate target strength estimation [12, 13]. This problem strongly indicates that a significant amount of energy is transferred to higher harmonic frequencies. The combined success of harmonic imaging in medical ultrasound and the findings of significant energy transfers to higher harmonic frequencies in sonar applications prompted us to take a new look at harmonic generation due to nonlinearity. In addition, recent developments in transducer technology now allow sonar systems to work with a wide frequency bandwidth. It is therefore possible to consider a transducer that can receive both at the first and second harmonic frequencies as in medical ultrasound imaging.

In a parallel development, the use of the frequency response of living organisms to help characterize them has witnessed a widespread interest [14]. The echo strength coming from fish or zooplankton depends on the size but also on biological attributes of the species like the presence or lack of a gas-filled or fluid-filled swimbladder [15, 16]. Combining the signals around the fundamental and second harmonic frequency bands could assist in marine life characterization. It is reasonable to think that other applications like bathymetry and buried objects detection [17] also

can benefit from echoes at different frequency bands. This is a motivation for making a sonar that can receive at both the fundamental and second harmonic frequencies as an aid for target classification.

In the process of studying the potential use of the second harmonic signal in sonar, we learned that in 1980 Muir [18] demonstrated the feasibility of using the second harmonic signal for imaging. However to the authors' knowledge, little has been published after this on second harmonic imaging in underwater acoustic. Our work can be seen as a continuation of Muir's.

In the first part of this article we confirm the presence of harmonic signals by measuring the pressure field radiated by two circular transducers with a center frequency of 121 kHz for the first one and 200 kHz for the second one in a water tank up to 12-m range. These measurements also give us the opportunity to compare with our numerical simulations. In the second part we show that second harmonic imaging can be used for target detection by imaging spherical targets using a pulse-echo technique. This shows better resolution capabilities compared to images obtained with the fundamental signal. In the third part of the paper we use numerical simulations of the pressure field and the active sonar equation to estimate the maximum useful range for the second harmonic signal and compare it to the maximum useful range of the fundamental signal. Finally the last part advocates for the use of the second harmonic signal by discussing the advantages of combining it with the fundamental signal. Some initial considerations based solely on numerical simulations were presented as a conference proceedings paper [19] but we also report the measurement results in this article.

II. Fundamental and second harmonic pressure fields characterization

We conducted an experiment in a large water tank where a hydrophone recorded the pulse generated by 121- and 200-kHz transducers. Simulated and measured pressure fields are compared up to 12-m depth within $\pm 30^\circ$ angular range.

A. Setup

The transducers used were of type ES120-7C and ES200-7C (Simrad, Horten, Norway) with a center frequency of 121 kHz for the ES120-7C type and 200 kHz for the ES200-7C type. Both are made for split-beam echo sounders. They were driven by an EK60 scientific echo sounder (Simrad, Horten, Norway). The hydrophone used to record the pressure pulse was of type ITC-6128 (ITC, Santa Barbara, CA). Its receive sensitivity varies less than 15 dB re 1 V/μPa between 100 kHz and 600 kHz. The hydrophone signal was sent to a pre-amplifier of type 3988 (Krohn-Hite, Brockton, MA) before being recorded by an oscilloscope of type DSO6014A (Agilent, Santa Clara, CA), and transferred to a personal computer (PC) for further processing (Fig. 1).

Profiles showing the angular dependence at fixed range were recorded for both transducers. The hydrophone was held still while the transducer was rotated counter clockwise covering an angular range of $\pm 30^\circ$ using an angular step of 0.5°. The profiles were recorded at regularly spaced depths covering a depth range from 10 cm to 12 m. They were also used to determine an axial profile along the main propagation axis. All measurements were done at the Kongsberg Maritime facility in Horten, Norway, in a water tank of dimensions approximately 6 m $\times$ 15 m $\times$ 6 m (width $\times$ length $\times$ depth).

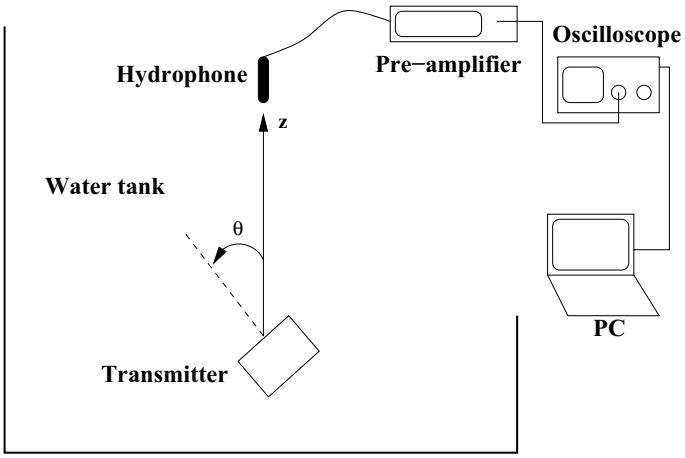

Fig. 1*: Setup for measurements of pressure fields in water tank. The hydrophone is positioned along the z axis and θ is the angle between the transducer's main propagation direction and the z axis.*

The size of both transducers and their aperture weighting are designed to give a 3-dB opening angle of approximately 7°. The weighting is optimized to reduce sidelobe levels at the expense of a slightly wider main lobe compared to a flat piston transducer of identical size. The transmitted pulse was a pulsed continuous wave of duration 256 μs.

B. Simulator

Nonlinear wave propagation simulations were carried out using an implementation of an angular spectrum method [20–23] for sources with cylindrical symmetry where the pressure field depends only on range and distance to the propagation axis. The angular spectrum method operates in the frequency domain and uses the operator splitting method. It consists of two operators applied sequentially. The first operator accounts for diffraction and absorption in the linear domain. It consists of multiplying the spatial Hankel transform of the particle velocity field for each harmonic at a depth z by the corresponding operator $H(n, \Delta z, r_i)$ defined for the nth harmonic by

$$H(n,\Delta z,r_i) = \begin{cases} \exp[-j2\pi\Delta z\sqrt{\left(\frac{nf}{c}\right)^2 - r_i^2} - \alpha_0(nf)^2\Delta z], & \text{if } |r_i| \le nf/c \\ \exp[-2\pi\Delta z\sqrt{r_i^2 - \left(\frac{nf}{c}\right)^2} - \alpha_0(nf)^2\Delta z], & \text{if } |r_i| > nf/c, \end{cases} \quad (1)$$

where Δz is the spatial step size, f the fundamental frequency, c the speed of sound, r_i the radial coordinate, and α_0 the attenuation coefficient in $\mathrm{Np{\cdot}m^{-1}{\cdot}Hz^{-2}}$. This linear step is called the ray-theory-updated frequency sampled convolution (RFSC) [21]. The second operator is a nonlinear step which implements the frequency domain solution of a lossless Burgers' equation. The nonlinear step at depth $z + \Delta z$ gives the expression of the velocity of the nth harmonic signal

$v_n(z+\Delta z, r_i)$ at radial coordinate r_i, as a function of the velocities obtained after the linear step:

$$v_n(z+\Delta z, r_i) = v'_n(z+\Delta z, r_i) + j\frac{\beta\pi f \Delta z}{c^2}\left(\sum_{k=1}^{n-1} k v'_k v'_{n-k} + \sum_{k=n+1}^{M} n v'_k v'^{*}_{k-n}\right), \quad \text{for } n = 1, 2, \cdots, M. \tag{2}$$

In (2) $v'_n(z+\Delta z, r_i)$ designates the particle velocity of the nth harmonic signal at depth $z+\Delta z$ and radial coordinate r_i obtained after the linear step, β is the coefficient of nonlinearity, and M is the number of harmonics taken into account in the simulations. The depth and radial indexes for v'_k were omitted in the summation for clarity and the star sign stands for complex conjugate. From the expression of the particle velocity v_n, the pressure is approximated by the relation $p_n = \rho c v_n$, where ρ is the density of the medium. At initialization ($z = 0$) the velocity profile of the fundamental signal $v_1(0, r_i)$ is determined by the extent of the transducer and its weighting as well as the input pressure level p_1 and for $k > 1$, $v_k(0, r_i) = 0$.

C. Measurements and simulations

To obtain the pressure field at a range z and limit perturbations from spatial aliasing, following Christopher and Parker [21], the radial extent of the simulation was set to $l = 2\tan\theta\ z$, where $\theta = 30°$ is the angular extent of the field at range z. The number of radial samples was $N = 2l/\lambda$ where λ is the wavelength. The input to the simulator was a continuous wave at frequency 121 kHz or 200 kHz. Table I summarizes the values of the parameters used in the simulations.

Table I*: Parameters used in the simulation for sound propagation in distilled water at 121 kHz and 200 kHz.*

Parameter	Value
Frequency (f)	121 kHz / 200 kHz
Source radius (R)	57.5 mm / 35 mm
Water density (ρ)	998 kg·m^{-3}
Sound speed (c)	1479 m·s^{-1}
Nonlinearity coefficient (β)	3.5
Attenuation coefficient (α_0)	0.025 Np·m^{-1}·MHz^{-2}
$\Rightarrow$ 3.0 dB·km^{-1}	at 121 kHz
$\Rightarrow$ 8.4 dB·km^{-1}	at 200 kHz
Number of harmonics (M)	50
Step size (Δz)	1 mm

1) ES120-7C transducer:

The recorded pulse was filtered to extract the amplitude of the signal around the fundamental, second, and third harmonic frequency bands. To compute levels equivalent to continuous wave propagation and allow comparison with the simulations, the transient parts where the pulse is building up and decaying were removed before filtering. The input electrical power levels sent to the ES120-7C transducer were 100 W and 600 W. Fig. 2 shows the frequency power spectra of the signal received when the hydrophone was situated on the propagation axis at 3 m from the source

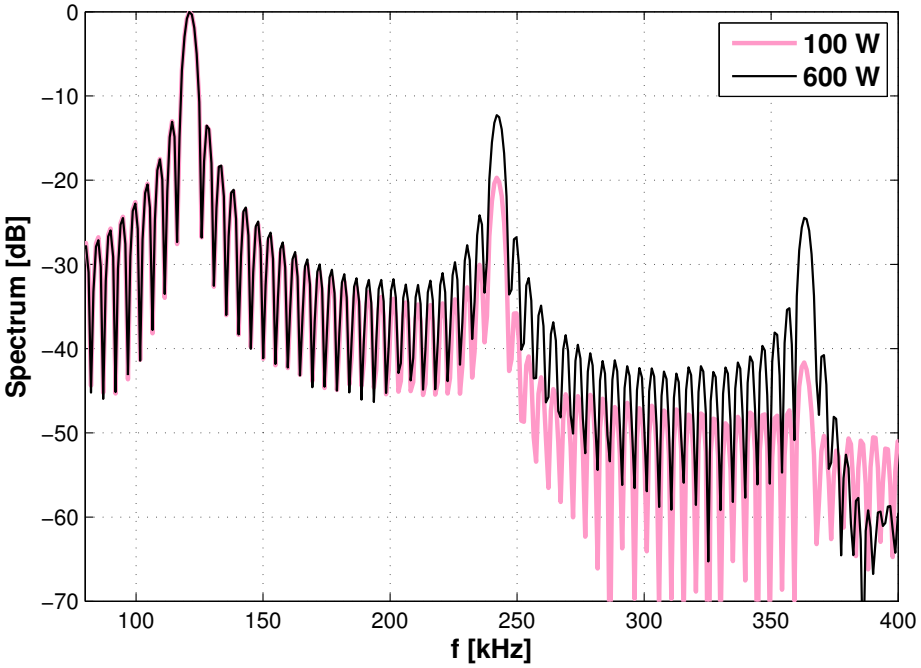

Fig. 2: *Frequency power spectra of received signal when hydrophone is on the propagation axis at 3 m from the source with 100-W (thick line) and 600-W (thin line) input electrical power. The spectra are normalized by their amplitude at the fundamental frequency, 121 kHz.*

for both input power levels and clearly indicates peaks for the first three harmonics.

From the angular profiles measured within the range interval 10 cm to 12 m, an axial profile was computed for each input power level along the propagation axis. We tried different pressure levels as an input to the simulator to obtain the best fit between measurements and simulations for the axial profile of the fundamental signal. This gave $p_1 = 190$ kPa for 100-W and $p_1 = 450$ kPa for 600-W input electrical power. In each case, the match between measurements and simulation results was comparable. The obtained axial profiles of pressure amplitude in the z-direction for an electrical power level of 600 W are shown in Fig. 3.3(a). The axial profile of the fundamental signal shows a drop in the pressure level of approximately 30 dB over 12 m in both cases. The results of a simulation using the KZKTexas code [24, 25] with the same input pressure level are also shown. They differ from the results of our simulator by less than 2 dB.

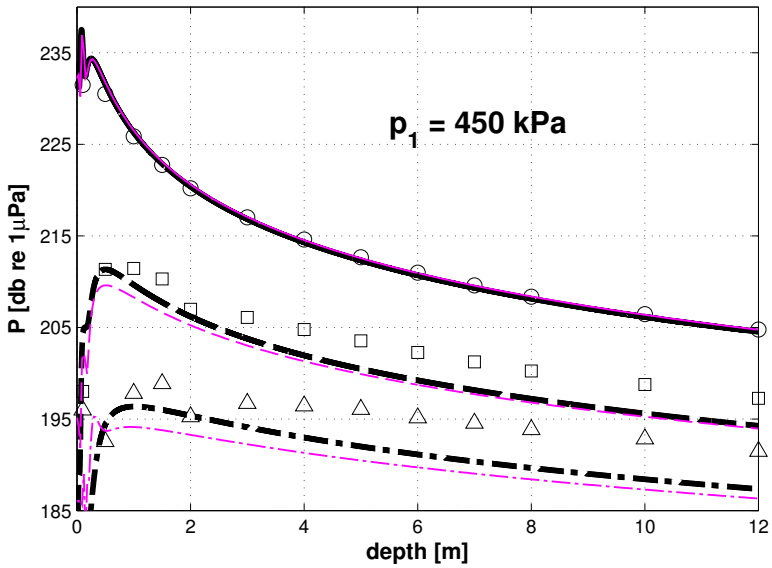

(a)

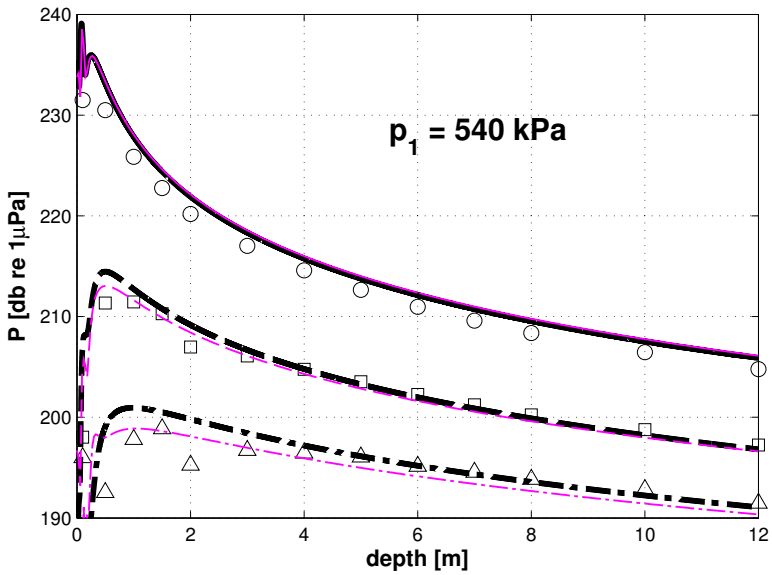

(b)

Fig. 3*: Axial profile of pressure amplitude for the ES120-7C transducer - input electrical power level: 600 W. Simulation results are shown with solid, dashed, and dash-dotted lines for first, second, and third harmonic signals, respectively. Bold lines are used for the results from our implementation of the ASA simulator. Thin lines are used for the results of the KZKTexas code. Input pressure* p_1 *estimated at 450 kPa (a) and 540 kPa (b). Measurements for first, second, and third harmonics are shown with circles, squares, and triangles, respectively.*

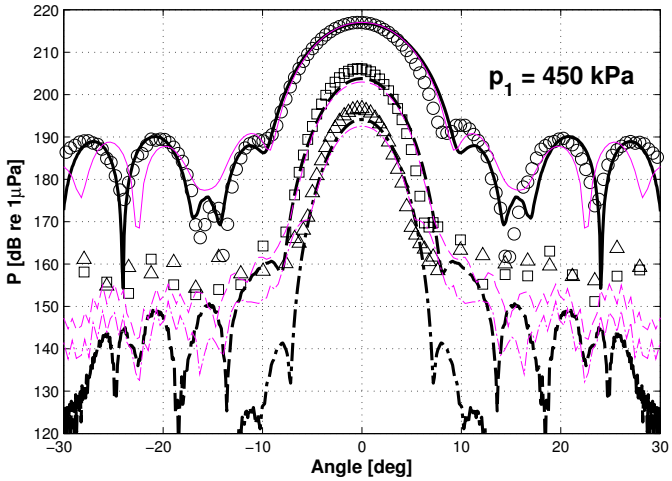

Fig. 4*: Angular beam profile of pressure amplitude for the ES120-7C transducer at 3-m range - input electrical power level: 600 W. Simulation results are shown with solid, dashed, and dash-dotted lines for first, second, and third harmonic signals, respectively. Bold lines are used for the results from our implementation of the ASA simulator. Thin lines are used for the results of the KZKTexas code. Measurements for first, second, and third harmonic signals are shown with circles, squares, and triangles, respectively.*

With this choice of input power level the axial profiles of the second and third harmonic signals show slightly higher levels for the measurements compared with what the simulations using the angular spectrum method predict, up to 4.4 dB higher beyond 6-m range. We tried to vary the values in the simulations for the nonlinearity coefficient β, the speed of sound c, and the attenuation coefficient α_0 within the intervals 3.32-3.61, 1447-1510 m·s^{-1}, and 0.31-0.17 dB·m^{-1}·MHz^{-2}, respectively, which are typical intervals at standard atmospheric pressure for a temperature between 10°C and 30°C [26]. Seeing no improvements with those changes or by varying the aperture radius, the input pressure p_1 was increased from 450 kPa to 540 kPa. The obtained match with the fundamental signal is not as close as with 450 kPa input pressure with a mismatch around 1.7 dB but the match with the second and third harmonics profiles is improved with a mismatch contained within 0.6 dB beyond 6 m [Fig. 3.3(b)]. The sensitivity data of the hydrophone were available for frequencies between 150 to 625 kHz with a 25-kHz interval. This means that in the case of the ES120-7C the sensitivity had to be interpolated at the fundamental and harmonic frequencies. If the interpolated sensitivity at the fundamental frequency was higher than the actual sensitivity, the measured pressure after correction for the receiver sensitivity would be under-estimated leading in turn to an axial profile for the fundamental signal that lies below the real pressure level. In that case an input pressure level used in the simulations to best fit the measured axial profile of the fundamental signal would be too low and it would explain why an input pressure of 540 kPa gives axial profiles that better fit the measurements for the second and third harmonic signals.

Fig. 4 compares measurements with simulations of angular profiles of pressure amplitude for first, second, and third harmonic signals at 3-m range with 600-W input electrical power. It also shows the results of a simulation using the KZKTexas code. For this comparison, the input pressure for the simulations was set to $p_1 = 450$ kPa which gave the best fit between measurements and

simulations for the axial profile of the fundamental signal. A fit to the fundamental signal was preferred since measured pressure levels around this frequency are higher than around the second or third harmonic frequencies and therefore less influenced by noise. This is specially important when comparing pressure levels away from the propagation axis.

The angular beam profiles shown in Fig. 4 shows a fairly good match between the measurements and the simulations using the angular spectrum with less than 4-dB difference for pressure levels above 160 dB re 1μPa. The match with the simulations using the KZKTexas code is comparable within the angular range $\pm 15^\circ$. However as the KZKTexas code is based on a parabolic approximation which is valid only for narrow angles, the beam profiles differ from the measurements at wider angles. The measurements and simulations confirm the narrower main lobe of higher harmonic signals compared to the fundamental signal and a main-lobe-to-sidelobe ratio of 41 dB for the second harmonic signal against 29 dB for the fundamental signal at 3 m. The noise level seems to lie between 150 and 160 dB re 1μPa. This fits with the 8-b resolution of our oscilloscope that fixes the minimum detectable level around 50 dB below the maximum level.

2) ES200-7C transducer:

Angular profile measurements and simulations were done for the ES200-7C transducer using 100- and 600-W input electrical power. Angular pressure profiles recorded at ranges between 10 cm and 12 m were used to compute an axial pressure profile. The best fit between measurements and simulations for the axial profile of the fundamental signal is obtained for $p_1 = 320$ kPa for 100-W and $p_1 = 800$ kPa for 600-W input electrical power. Both the angular and axial profiles have very similar shape as the profiles shown in Figs. 3.3(a) and 4 and are therefore not shown. The match between measurements and simulation results for 100- or 600-W input power is also comparable.

As with the ES120-7C, the measured angular profiles agree with the simulations on the overall beam shape and the level differences are mainly contained within 4 dB for negative angles and 10 dB for positive angles. The largest deviations for positive angles occur around the sidelobes of the fundamental signal. The agreement between measurements and simulations around the main lobe is better with a difference mainly contained within 5 dB. The main-lobe-to-sidelobe ratio is approximately 22 dB for the fundamental signal and 41 dB for the second harmonic signal at 3 m.

The axial profile of the fundamental signal shows a drop in the pressure level of approximately 35 dB over 12 m. As expected, the attenuation is more significant than when using the ES120-7C transducer that transmits at a lower frequency. The measurements for the axial profiles are in this case less than 2 dB below the simulation results beyond 6 m. This mismatch cannot be explained by the sensitivity of the hydrophone that was measured at the harmonic frequencies of the ES200-7C and the input pressure level p_1 can be assumed adequate. However an extension arm was added to the positioning system for measurements between 10 cm and 2 m with both transducers increasing the uncertainty of the hydrophone position by approximately ± 3 cm. A slight offset in the positioning of the hydrophone from the beam's propagation axis is a possible explanation for this mismatch that diminishes at longer range. Indeed the beam pattern in an angle span of $\pm 30^\circ$ covers a smaller radial extent and varies more with radial distance close to the source as shown in Fig. 5. A position error at short range can therefore give a larger error in the pressure measurement than farther from the source. This explains wider variations between measurements and simulations in this area with both transducers.

The overall match between measurements and simulation is within less than 5 dB beyond 6-m range. Considering the variations of the axial pressure for a 200-kHz transducer with an input

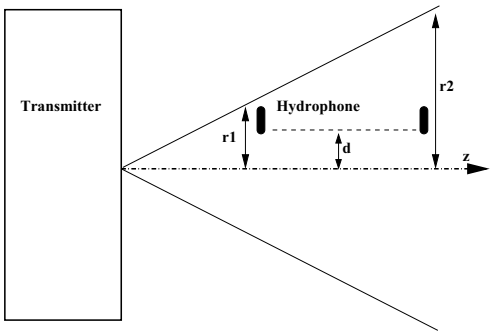

Fig. 5*: Effect of a constant radial offset d of the position of the hydrophone from the beam's propagation axis. The spatial extent $r1$ of the beam pattern is smaller at short range than the radial extent at longer range $r2$ giving more variations with the radial distance, and a possible larger error in the axial pressure measurements.*

pressure of 800 kPa over a range of 1000 m that is about 70 dB, and assuming that the simulator gives similar results over long range, the achieved precision is acceptable for our purpose. We can use our simulator to estimate and compare the range of the second harmonic signal to the range of the fundamental signal for an active sonar using the active sonar equation. It should be mentioned that the aim of these comparisons is not to validate the model based on the angular spectrum approach. This verification has been done and reported earlier in several papers [22, 27, 28]. The purpose is rather to check our implementation of the method, that we use the correct parameters values, and that the assumptions that the model relies on are appropriate.

III. Second harmonic pulse-echo imaging

The measured profiles confirmed that higher harmonics were present and detectable. We therefore set up an experiment where the ES120-7C transducer with a center frequency of 121 kHz sent a pulse that reflected on targets and the second harmonic at 242 kHz was recorded by the ES200-7C.

Both transducers were set side by side and the targets consisted of four spheres. Three spheres were of diameter 38.1 mm and made of tungsten carbide while the fourth sphere had a diameter of 13.7 mm and was made of copper. They were positioned in the horizontal plane which also contained the propagation axis of both transducers and at a distance of approximately 2.75 m from the source. The spheres were separated by approximately 0.8 m as shown in Fig. 6

The transducer ES200-7C was connected directly to the oscilloscope. The transducers were rotated counter clockwise covering an angular range of approximately 15° to -45°, where 0° is the direction parallel to the wall of the water tank and positive angle is taken in the clockwise direction. Input electrical power levels sent to the ES120-7C were 1 kW and 2 kW. The pulse used was a pulsed continuous wave of duration 128 μs. The recorded data were processed to filter out the pulse around the fundamental and the second harmonic frequency bands. The receiving sensitivity of the ES200-7C was estimated at 121 kHz and 242 kHz and compensated for to get the correct pressure level estimates for the recorded pulse. Fig. 7 displays the root mean square (RMS) value of the pressure amplitude of the received echoes from the spheres when filtered around the

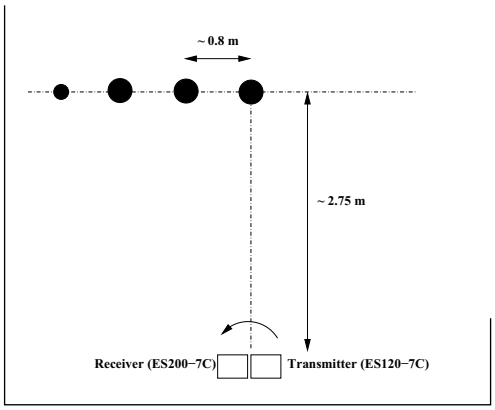

Fig. 6*: Setup of transducers and spheres for second harmonic imaging.*

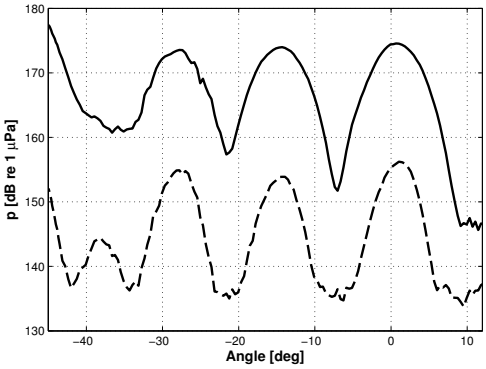

Fig. 7*: RMS value of the pressure amplitude of the received echoes from the spheres when filtered around fundamental (solid line) and second harmonic (dashed line) frequencies. The input electrical power level was 1 kW.*

fundamental and second harmonic frequency bands for 1-kW input power. The recorded echo pressure amplitudes are very similar in the case of 2-kW input power.

The echoes from the three biggest spheres are clearly visible. It is interesting to note that the echo from the smallest sphere is barely noticeable when filtering around the fundamental frequency while it is clear when filtering around the second harmonic frequency. This is due to the wider main lobe of the fundamental signal compared to the main lobe of the second harmonic signal. Indeed when the transducers point towards the small sphere the ensonified region delimited by the main lobe of the fundamental signal also includes part of the closest large sphere and some of the tank wall. The tank walls have a rough surface and the direct echo from the wall as well as from the closest large sphere add to the weaker echo from the small sphere. As the transducers rotate past the small sphere these perturbing echoes are strong enough to mask the signal reflected by the smaller sphere and make it barely distinguishable.

By comparison the region ensonified by the main lobe of the second harmonic signal is smaller. When the transducers point towards the smaller sphere the echoes coming from the closest large

sphere and the wall are much weaker. As the transducers rotate past the smaller sphere these weaker perturbing echoes allow the signal reflected by the smaller sphere to emerge. This allows a better delimitation in the angular profile of the echo coming from the smaller sphere.

From the measurements, it can be established that the average opening angle of the beam delimited by a 6-dB decrease from the maximum of the amplitude (full-width-half-maximum) of the echoes from the three largest spheres are 7.1° for the fundamental signal and 5.2° for the second harmonic signal for 1-kW input power. For 2-kW input power the average 6-dB opening angles are 7.7° and 5.3° for the fundamental and second harmonic signals, respectively. Assuming the spheres are point scatterers and reflect incoming waves isotropically, the beam pattern from each sphere echo is the product of the transmitter (ES120-7C) and receiver (ES200-7C) beam patterns. Since both transducers are designed with a 3-dB opening angle of approximately 7°, their product should give a beam pattern with a 6-dB opening angle of approximately 7°. This is confirmed by the data at the fundamental frequency. At the second harmonic frequency the main lobe of each echo is narrower than for the fundamental signal. This gives greater resolving capabilities as expected, just like one is used to in medical ultrasound applications.

This experiment shows that it is possible to use the second harmonic signal for imaging spheres. The image obtained by using the signal around the second harmonic frequency shows better resolving capabilities and reveals one target that fundamental imaging does not detect. The larger main-lobe-to-sidelobe ratio of the second harmonic signal can also be beneficial to target imaging. In a shallow water environment a sonar scanning at low grazing angles will be perturbed by surface and bottom reflections of the sidelobes. Scatterers situated in the propagation direction of the sidelobes will also create perturbations. The amplitude of these perturbations should be reduced in the case of second harmonic imaging due to the lower sidelobe levels.

IV. Range estimation for the second harmonic signal

As the pressure level of the second harmonic signal is well below the level of the fundamental signal, it is interesting to compare the maximum useful range for a sonar using the echo filtered around the second harmonic or the fundamental frequency bands. We therefore used our simulator to estimate the transmitted pulse pressure level along the main propagation direction in conjunction with traditional active sonar equations to estimate the maximum range at which the useful signal level is higher than the noise or reverberation level.

A. Active sonar equations

The two forms of the active sonar equation when the perturbation source for target detection is either isotropic noise or reverberation are, respectively:

$$\mathrm{SL} - 2\mathrm{TL} + \mathrm{TS} = \mathrm{NL} - \mathrm{DI} + \mathrm{DT}, \tag{3}$$

and

$$\mathrm{SL} - 2\mathrm{TL} + \mathrm{TS} = \mathrm{RL} + \mathrm{DT}, \tag{4}$$

where SL, TL, TS, NL, DI, DT, and RL stand for source level, transmission losses, target strength, noise level, directivity index, detection threshold and reverberation level, respectively. The definition of the terms used in (3) and (4) can be found in [29] and in the appendix. These equations characterize the case of the monostatic sonar. They give the maximum range to which a sonar can detect a target. Beyond this range the useful signal level is below either the noise or reverberation level and the signal-to-noise ratio becomes too small for target detection at a pre-assigned probability of detection and false alarm.

Each term in the equation is adapted to the second harmonic signal when suited to compare the maximum range for the fundamental and the second harmonic signals. The water depth and the sonar depression angle are assumed large enough for the bottom and surface reverberations to be neglected. Hence we only consider volume reverberation. This simulation represents a simple case of the models described by Urick [29]. The maximum attainable ranges may vary in real cases due to variable setups and environmental conditions. The aim of the simulation is to check that the attainable range of the second harmonic is comparable to the range of state-of-the-art sonars using fundamental imaging.

B. Simulations

The simulator based on the angular spectrum approach and described in section II-B was used to estimate the on-axis pressure level at long range. In the simulations a circular flat piston with the same dimensions as the ES200-7C was taken as source and receiver and the reflector was a fish of length L. The water density and sound speed were taken to be constant. The equations for determining TL, DT, NL, DI, and RL in our case are presented in the appendix. Note that NL$-$DI is constant with frequency. DT being independent of frequency, the quantity NL $-$ DI $+$ DT is equal for the fundamental and second harmonic signals.

The effects of diffraction were taken into account up to 5 m in the simulation. Beyond this range, diffraction was neglected and the wavefront was approximated by a plane in the radial extent of the simulation. The linear step became a simple attenuated spherical spreading. Instead of using the linear operator described by (1) between ranges z and $z + \Delta z$, the pressure level of the nth harmonic was computed as follows

$$p_n(z + \Delta z) = p_n(z)\frac{z}{z + \Delta z}e^{-[\alpha + j2\pi n f/c]\Delta z}, \tag{5}$$

where α is the absorption coefficient at frequency f expressed in Np·m^{-1}. While the absorption in distilled water can be considered proportional to the square of the frequency as shown in (1), the absorption in seawater obeys a more complicated law. The absorption model used in the simulations was based on the formula given by Ainslie and McColm [30] where temperature, salinity, pH, and depth are parameters. This formula reveals a large dependency on temperature. Table II shows the values of the parameters used to estimate the terms of the sonar equations and to simulate attenuation in seawater. Using these parameters, absorption in seawater is about 45 dB·km^{-1} at 200 kHz and 96 dB·km^{-1} at 400 kHz. The value for the other simulation parameters are unchanged from what Table I shows.

Table II: *Parameters used to estimate the terms in the active sonar equation (see also appendix for detailed on their use) and to simulate attenuation in seawater.*

Parameter	Value
Input pressure (p_1)	800 kPa
Fish size (L)	30 cm
Salinity	34 ppt
pH	7.7
Depth	100 m
Temperature	5°C
Volume scattering strength (S_v)	−85 dB
Pulse duration (τ)	1 ms
Detection probability (P_d)	95%
False alarm probability (P_f)	0.01%

C. Results

Figs. 8 and 9 show the different parts of the sonar equation applied to the fundamental and second harmonic signals.

It appears that the sonar performance is limited by reverberation for the fundamental signal. The maximum range is 343 m. For the second harmonic signal the noise level is the limitation. The maximum range is 243 m. This is possible because the reverberation level is proportional to the source level while the noise level is not.

A relation can be found between the maximum range of the fundamental and the second harmonic signals when reverberation is the only limitation. In the remote far field the upper harmonics do not obey spherical spreading because local effects contribute more to nonlinearity than the propagation of existing harmonics [31]. However if the range is limited as in our case, the transmission losses can be approximated for the first two harmonics by

$$\mathrm{TL} = 20\log r + \alpha r, \tag{6}$$

when α is expressed in dB·m^{-1}. Combining (6) and (17) the reverberation level can be written as

$$\mathrm{RL} = \mathrm{SL} - 2\mathrm{TL} + S_v + 10\log V, \tag{7}$$

which when used in (4) gives

$$\mathrm{TS} = S_v + 10\log V + \mathrm{DT}. \tag{8}$$

We call r_1 and r_2 the values of the ranges that satisfy (8) for the fundamental and the second harmonic signals, respectively. Using (11), (18) and (19) to express TS and V, we can write:

$$-0.9\log\left(\frac{f}{2f}\right) = 20\log\left(\frac{r_1}{r_2}\right) + 20\log\left(\frac{\lambda}{\lambda/2}\right) \tag{9}$$

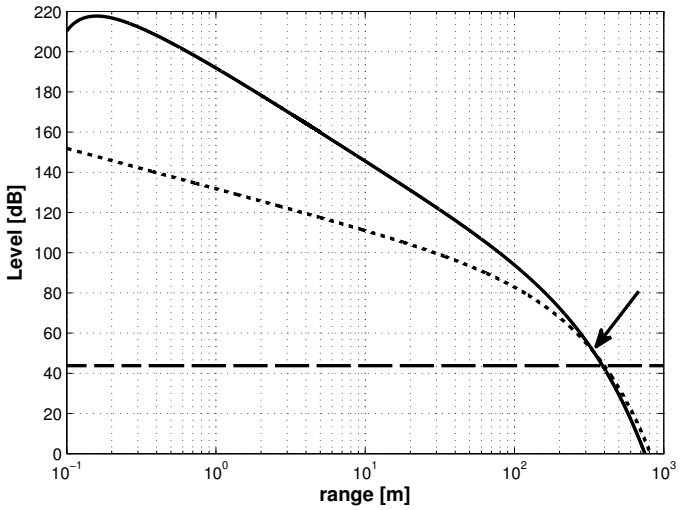

Fig. 8*: Active sonar equation plots for the fundamental signal propagating in seawater. The solid line is the left-hand side of the active sonar equation:* $SL - 2TL + TS$*. The dashed line is the right-hand side of* (3)*:* $NL - DI + DT$*. The dotted line is the right-hand side of* (4)*:* $RL + DT$*. The arrow indicates the maximum range where signal is no longer detectable due to reverberation.*

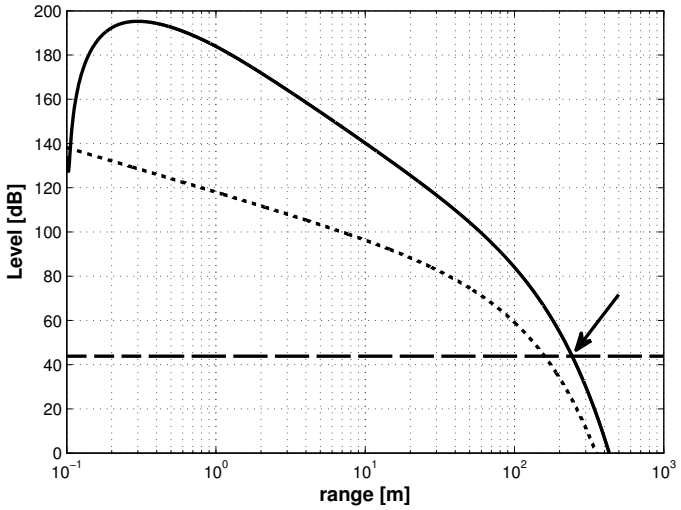

Fig. 9*: Active sonar equation plots for second harmonic signal propagating in seawater. The solid line is the left-hand side of the active sonar equation:* $SL - 2TL + TS$*. The dashed line is the right-hand side of* (3)*:* $NL - DI + DT$*. The dotted line is the right-hand side of* (4)*:* $RL + DT$*. The arrow indicates the maximum range where signal is no longer detectable due to noise.*

which gives the following relation between r_1 and r_2,

$$\frac{r_1}{r_2} \approx 0.52. \tag{10}$$

This surprising result shows that, in the case of reverberation only, the second harmonic signal has a maximum range around twice the range of the fundamental signal. The most favourable condition for exploiting the second harmonic signal is therefore where the ambient noise is low. In that case the high pressure level of the fundamental signal is likely to generate a high reverberation level while the low pressure level of the second harmonic signal contributes to limited reverberation. This low pressure level becomes a limitation when the ambient noise level rises and the signal-to-noise ratio of the second harmonic signal becomes too weak.

V. Why use the second harmonic?

The first two sections showed how the second harmonic signal can contribute to improving image quality in sonar imaging. But if a broadband transducer can be used for imaging both at the fundamental and second harmonic frequencies it is legitimate to compare the performance of a sonar transmitting at 200 kHz and using echoes around the first and second harmonic frequency bands with the performance of a sonar transmitting at 200 kHz then at 400 kHz and using the echoes around the fundamental frequencies only.

To estimate the maximum useful range for such a sonar transmitting at 400 kHz we use our simulator with an input pressure of 600 kPa and all the other parameters unchanged from what Table II describes. In this configuration the maximum useful range is below 220 m which is shorter than the maximum useful range for the second harmonic signal at 400 kHz. Moreover while a sonar transmitting at 400 kHz with the same transducer dimensions has a narrower main lobe and therefore a better resolution than the first and second harmonic signals of a sonar transmitting at 200 kHz, it lacks the high main-lobe-to-sidelobe ratio that the second harmonic signal at 400 kHz provides. One way to increase the main-lobe-to-sidelobe ratio is to apply a weighting on the aperture. However the weighting function needed reduces the transmitted axial pressure level and limits even further the maximum useful range.

The combination of echoes around the fundamental and second harmonic frequency bands brings additional advantages. It gives an update rate that is twice the rate of a sonar receiving echoes around the fundamental frequency only. The two images obtained allow one to combine the high-resolution of the second harmonic signal at short range and the long-range capability of the fundamental signal with a lower resolution. In addition the echoes at two different frequencies can be used to characterize acoustic targets. Previous studies have shown that one can use the echoes at multiple frequencies to distinguish organisms with different acoustic properties [32]. The size of the target is one obvious parameter that influences the frequency response. When the target size is well below the pulse wavelength λ the echo received comes from a diffraction process while it comes from reflection when the target size is much larger than the wavelength. A simplistic model for a target is a gas-filled bubble of radius a immersed in water. As mentioned in [29] the ratio of the acoustic cross section σ to the geometrical cross section in this case is proportional to $(ka)^4$ when $ka \ll 1$, where $k = 2\pi/\lambda$. For $ka \gg 1$ this ratio is constant. Given that $\mathrm{TS} = 10\log\left(\frac{\sigma}{4\pi}\right)$ the target strength evolves similarly with ka.

But the frequency response of organisms depends on more factors than just their size [32]. Experiments have been carried out to characterize the frequency response of fish with or without swimbladder [16, 33, 34], zooplankton [15, 34, 35], or jellyfish [34, 36]. They all give examples of how living organisms can be differentiated by their frequency response. For instance at frequencies between 18 and 200 kHz, Korneliussen and Ona showed that signal from zooplankton mainly comes from Rayleigh scattering while for most swimbladdered fish it comes from geometric scattering [32].

This shows that the combined use of echoes filtered around the fundamental and second harmonic frequency bands can help identifying living organisms and that it is advantageous when imaging targets compared to using only the echo filtered around the fundamental center frequency.

VI. Conclusions and future studies

Through experiment we have verified that propagation of sound in water for state-of-the-art sonars generates significant signals around the second and third harmonic frequency bands. Measurements of the pressure field radiated by two commercial transducers were compared with numerical simulations and fit within 5 dB beyond 6-m range. They show that the second harmonic signal exhibits low sidelobes relative to the main lobe, which is important in many applications of sonar imaging. The measured pressure fields were in accordance with the design of both transducers exhibiting a 3-dB opening angle around 7° and a main-lobe-to-sidelobe ratio higher than 20 dB. Higher attenuation for the pressure level of the fundamental signal at the highest transmitted frequency was also confirmed with a pressure drop over 12 m of approximately 30 dB at 121 kHz and 35 dB at 200 kHz.

The second harmonic signal was used to image spherical targets. The echo from the targets had a narrower main lobe when filtering the signal around the second harmonic frequency band and the smallest sphere could only be detected by the second harmonic signal. This shows that use of the second harmonic signal can potentially improve the image quality when combining it with the fundamental signal.

A simulator was used to compare the maximum range as defined in the active sonar equation for the fundamental signal at 200 kHz and the second harmonic signal at 400 kHz in the case of isotropic noise and volume reverberation as limiting factors. A simple case of the models presented in Urick's text [29] was used and indicates that the second harmonic signal can be used to detect a 30-cm long fish at a maximum range of approximately 243 m against 343 m for the fundamental signal when the source level is 228 dB and the detection threshold is 12 dB. In this case the maximum achievable range for the fundamental signal of a sonar transmitting at 400 kHz is less than for the second harmonic signal of a sonar transmitting at 200 kHz. This counterintuitive result depends on the model used and the levels chosen for the input pressure, the noise, and the scattering strength but it shows that there is a role for second harmonic imaging in sonars and echo-sounders. Using a single transducer one could combine the high resolution of the second harmonic signal at short range with the long-range capability and lower resolution of the fundamental signal.

Combining echoes from the fundamental and the second harmonic signals doubles the data rate per ping. In addition the echoes at two different frequencies can contribute to target classification, e.g., living organisms, by comparing their frequency response. This is another potential use for the second harmonic signal in fishery research.

In contrast to using several transducers simultaneously when characterizing living organisms by their frequency response, combining the fundamental with the second harmonic signals does not require extra equipment. This arrangement could be implemented into existing sonar systems at a potential reduced cost provided that the cost of wideband transducers will drop in the future.

A limitation of the presented technique is the need for high transmitted power. With low input power the higher harmonics signals generated due to nonlinear propagation are negligible. Medium-to-high input powers are necessary. In our case 1-kW input power was enough to achieve second harmonic imaging. Increasing input power also has its limitations in the form of cavitation, hard shock, or saturation that all dissipate energy into the medium. In addition the receiver needs to be sensitive enough to detect the low level of the echoes and the uncertainty of the recorded level should be small if used in organism characterization.

The results of these experiments confirm the potential of second harmonic imaging in underwater acoustics. In a future work, combining the echoes received around the fundamental and second harmonic frequency bands could be tried at sea using existing echo-sounders or sonars. Such an experiment would demonstrate both the image enhancement and target classification capabilities of the method. Experiments in shallow water would put in evidence the reduction in perturbations from surface and bottom reverberation when using the second harmonic signal with low sidelobe levels. Other examples of future work include a more detailed characterization of the second harmonic imaging in terms of resolution and sidelobe echoes strength as well as a comparison between fundamental and second harmonic images for varying ranges.

Appendix
Computation of active sonar equation

The target strength is defined as

$$\mathrm{TS} \equiv 19.1 \log L - 0.9 \log(f/1\ \mathrm{kHz}) - 62 \tag{11}$$

where L is the size of the fish in cm and f the frequency. Equation (11) is based on empirical measurements [29]. In our simulations, TS ≈ -36 dB at 200 kHz.

For the case of an active sonar transmitting a sinusoidal pulse in a background of Gaussian noise where the received signal is processed by an energy detector, the detection threshold can be defined as [37]

$$\mathrm{DT} \equiv -5 \log M + \left(6.2 + \frac{4.54}{\sqrt{M + 0.44}}\right) \log(A + 0.12AB + 1.7B), \tag{12}$$

where M is the number of independent samples of the squared amplitudes used by the energy detector and is equal to 1 in our case and

$$A \equiv \ln \frac{0.62}{P_f}, \tag{13}$$

$$B \equiv \ln \left(\frac{P_d}{1 - P_d}\right), \tag{14}$$

with P_f the false alarm probability taken equal to 0.01% and P_d the detection probability taken equal to 95% in our case. Equation (12) takes into account the low time-bandwidth product

(equal to 1 in our case) and is valid for sinusoidal signals in narrowband Gaussian noise. In our simulations, DT $\approx$ 12 dB.

The noise generated for the frequency range of interest is mainly due to thermal noise originating in the molecular motion of the sea. The chosen model valid for frequencies above 100 kHz for the noise level is

$$\mathrm{NL} \equiv -15 + 20\log(f/1\ \mathrm{kHz}) + 10\log\omega. \tag{15}$$

where ω is the bandwidth of the receiver assumed equal to the bandwidth of the signal (the inverse of the signal duration in our case). Both the detection threshold and the noise level are defined by considering the noise power in the bandwidth of the receiver ω instead of a 1-Hz bandwidth as done in [29]. By doing so, the same definition for the detection threshold can be used in (3) and (4). In our simulations, NL $\approx$ 61 dB at 200 kHz.

In our case the directivity index is the same as the array gain. For a circular piston of radius R we get [29]

$$\mathrm{DI} \equiv 10\log\left[\left(\frac{2R\pi}{\lambda}\right)^2\right], \tag{16}$$

where λ is the wavelength. In our simulations, DI $\approx$ 30 dB at 200 kHz.

The reverberation level is defined as

$$\mathrm{RL} \equiv \mathrm{SL} - 40\log r + S_v + 10\log V - 2\alpha r, \tag{17}$$

where r is the range, S_v the volume scattering strength, V is characteristic of the reverberation volume, and α the attenuation coefficient expressed in dB·m^{-1}. Computations in [29] give the following expression for V:

$$V \equiv \frac{c\tau}{2}\Psi r^2, \tag{18}$$

where c is the speed of sound, τ is the pulse duration, and for a circular piston of radius R, Ψ is defined by [29]

$$10\log\Psi \equiv 20\log\left(\frac{\lambda}{2\pi R}\right) + 7.7. \tag{19}$$

According to [29], the source of volume scattering strength S_v is biological. For frequencies above 20 kHz, the scatterers are likely to be zooplankton. The variation of S_v in this frequency range is slight or absent. S_v is taken constant for the fundamental and second harmonic signals in our simulations.

Bibliography

[1] P. J. Westervelt, "Parametric acoustic array," *J. Acoust. Soc. Am.*, vol. 35, no. 4, pp. 535–537, Apr. 1963.

[2] H. O. Berktay, "Possible exploitation of non-linear acoustics in underwater transmitting applications," *J. Sound Vib.*, vol. 2, no. 4, 1965.

[3] A. Caiti, O. Bergem, and J. Dybedal, "Parametric sonars for seafloor characterization," *Meas. Sci. Tech.*, vol. 10, pp. 1105–1115, 1999.

[4] A. Trucco, "Detection of objects buried in the seafloor by a pattern-recognition approach," *IEEE J. Oceanic Eng.*, vol. 26, no. 4, pp. 769–782, Oct. 2001.

[5] L. Bjørnø, "Forty years of nonlinear ultrasound," *Ultrasonics*, vol. 40, no. 1-8, pp. 11–17, 2002.

[6] F. A. Duck, "Nonlinear acoustics in diagnostic ultrasound," *Ultrasound Med. Biol.*, vol. 28, no. 1, pp. 1–18, 2002.

[7] H. Becher, K. Tiemann, T. Schlosser, C. Pohl, N. C. Nanda, M. A. Averkiou, J. Powers, and B. Lüderitz, "Improvement in endocardial border delineation using tissue harmonic imaging," *Echocardiogr.*, vol. 15, no. 5, pp. 511–517, 1998.

[8] R. J. Graham, W. Gallas, J. S. Gelman, L. Donelan, and R. E. Peverill, "An assessment of tissue harmonic versus fundamental imaging modes for echocardiographic measurements," *J. Am. Soc. Echocardiogr.*, vol. 14, no. 12, pp. 1191–1196, 2001.

[9] G. A. Whalley, G. D. Gamble, H. J. Walsh, S. P. Wright, S. Agewall, N. Sharpe, and R. N. Doughty, "Effect of tissue harmonic imaging and contrast upon between observer and test-retest reproducibility of left ventricular ejection fraction measurement in patients with heart failure," *Eur. J. Heart Failure*, vol. 6, no. 1, pp. 85–93, 2004.

[10] S. Tanaka, O. Oshikawa, T. Sasaki, T. Ioka, and H. Tsukuma, "Evaluation of tissue harmonic imaging for the diagnosis of focal liver lesions," *Ultrasound Med. Biol.*, vol. 26, no. 2, pp. 183–187, 2000.

[11] T. Schmidt, C. Hohl, P. Haage, M. Blaum, D. Honnef, C. Weiss, G. Staatz, and R. W. Günther, "Diagnostic accuracy of phase-inversion tissue harmonic imaging versus fundamental B-mode sonography in the evaluation of focal lesions of the kidney," *Am. J. Roentgenology*, vol. 180, no. 6, pp. 1639–1647, 2003.

[12] F. E. Tichy, H. Solli, and H. Klaveness, "Non-linear effects in a 200-kHz sound beam and the consequences for target-strength measurement," *ICES J. Mar. Sci.*, vol. 60, pp. 571–574, 2003.

[13] A. Pedersen, "Effects of nonlinear sound propagation in fisheries research," Ph.D. dissertation, University of Bergen, Department of Physics and Technology, Oct. 2006.

[14] P. G. Fernandes, R. J. Korneliussen, A. Lebourges-Dhaussy, J. Masse, M. Iglesias, N. Diner, E. Ona, T. Knutsen, J. Gajate, and R. Ponce, "The SIMFAMI project: species identification methods from acoustic multifrequency information. Final report," Q5RS-2001-02054. FRS Marine Laboratory Aberdeen, Aberdeen, UK, Tech. Rep., 2006.

[15] A. S. Brierley, P. Ward, J. L. Watkins, and C. Goss, "Acoustic discrimination of southern ocean zooplankton," *Deep Sea Research II*, vol. 45, no. 7, pp. 1155–1173, 1998.

[16] S. Gauthier and J. K. Horne, "Potential acoustic discrimination within boreal fish assemblages," *ICES J. Mar. Sci.*, vol. 61, no. 5, pp. 836–845, 2004.

[17] J. R. Stack, G. Dobeck, and C. Bernstein, "Multi-frequency backscatter variations for classification of mine-like targets from low-resolution sonar data," in *Proc. MTS/IEEE OCEANS*, Washington DC, Sep. 2005, pp. 218–222.

[18] T. G. Muir, "Nonlinear effects in acoustic imaging," *Acoust. Imag.*, vol. 9, pp. 93–109, 1980.

[19] F. Prieur, S. P. Näsholm, A. Austeng, and S. Holm, "Exploiting nonlinear propagation in echo sounders and sonar," in *Proc. European Conference on Underwater Acoustics.*, Istanbul, Turkey, Jul. 2010.

[20] J. F. Synnevåg and S. Holm, "Non-linear propagation of limited diffraction beams," in *Proc. IEEE Ultrason. Symp. 1998*, Sendai, Japan, Oct. 1998, pp. 1885–1888.

[21] P. T. Christopher and K. J. Parker, "New approaches to the linear propagation of acoustic fields," *J. Acoust. Soc. Am.*, vol. 90, no. 1, pp. 507–521, Jul. 1991.

[22] ——, "New approaches to nonlinear diffractive field propagation," *J. Acoust. Soc. Am.*, vol. 90, no. 1, pp. 488–499, Jul. 1991.

[23] S. Holm and F. Prieur, "Low sidelobe limited diffraction beams in the nonlinear regime," *J. Acoust. Soc. Am.*, vol. 128, no. 3, pp. 1015–1020, Sep. 2010.

[24] Y. S. Lee, R. Cleveland, and M. F. Hamilton, "KZKTexas," http://people.bu.edu/robinc/kzk/, date last viewed May 30, 2012, Oct. 1998.

[25] Y. S. Lee and M. F. Hamilton, "Time-domain modeling of pulsed finite-amplitude sound beams," *J. Acoust. Soc. Am.*, vol. 97, pp. 906–917, 1995.

[26] F. A. Duck, *Physical properties of tissues - A comprehensive reference book*. San Diego: Academic Press, 1990, ch. 4: Acoustic Properties of Tissue at Ultrasonic Frequencies, p. 95.

[27] R. J. Zemp, "Modeling nonlinear ultrasound propagation in tissue," Master's thesis, Institute of biomaterials and biomedical engineering, University of Toronto, 2000.

[28] R. J. Zemp, J. Tavakkoli, and R. S. C. Cobbold, "Modeling of nonlinear ultrasound propagation in tissue from array transducers," *J. Acoust. Soc. Am.*, vol. 113, no. 1, pp. 139–152, Jan. 2003.

[29] R. J. Urick, *Principles of underwater sound*, 3rd ed. McGraw-Hill Book Company, 1983, ch. 2, 3, 7, 8, and 9.

[30] M. Ainslie and J. G. McColm, "A simplified formula for viscous and chemical absorption in sea water," *J. Acoust. Soc. Am.*, vol. 103, no. 3, pp. 1671–1672, Mar. 1998.

[31] D. T. Blackstock, "Once Nonlinear, Always Nonlinear," in *AIP Conf. Proc.*, vol. 838, 2006, pp. 601–606.

[32] R. J. Korneliussen and E. Ona, "Synthetic echograms generated from the relative frequency response," *ICES J. Mar. Sci.*, vol. 60, no. 3, pp. 636–640, 2003.

[33] K. G. Foote, "Importance of the swimbladder in acoustic scattering by fish: a comparison of gadoid and mackerel target strengths," *J. Acoust. Soc. Am.*, vol. 67, no. 6, pp. 2084–2089, Jun. 1980.

[34] A. De Robertis, D. R. McKelvey, and P. H. Ressler, "Development and application of an empirical multifrequency method for backscatter classification," *Can. J. Fish. Aquat. Sci.*, vol. 67, no. 9, pp. 1459–1474, Sep. 2010.

[35] D. R. McKelvey and C. D. Wilson, "Discriminant classification of fish and zooplankton backscattering at 38 and 120 khz," *Trans. Am. Fish. Soc.*, vol. 135, no. 2, pp. 488–499, Apr. 2006.

[36] A. S. Brierley, B. E. Axelsen, D. C. Boyer, C. P. Lynam, C. A. Didcock, H. J. Boyer, C. A. J. Sparks, J. E. Purcell, and M. J. Gibbons, "Single-target echo detections of jellyfish," *ICES J. Mar. Sci.*, vol. 61, no. 3, pp. 383–393, 2004.

[37] W. J. Alberhseim, "A closed-form approximation to Robertson's detection characteristics," *Proc. IEEE*, vol. 69, no. 7, pp. 839–839, Jul. 1981.

Paper II

Theoretical improvements when using the second harmonic signal in acoustic Doppler current profilers

F. Prieur, R. E. Hansen

IEEE Journal of Oceanic Engineering, Revised version submitted June 11, 2012.

Theoretical improvements when using the second harmonic signal in acoustic Doppler current profilers

F. Prieur, R. E. Hansen

Abstract— Acoustic Doppler current profilers and velocity logs are devices that compute the Doppler frequency shift undergone by a pulse after reflection by floating particles in water or by the seafloor. Using this Doppler shift, the velocity of the water currents carrying the reflecting particles or the speed of a vessel relative to the sea bottom can be estimated. The attainable performance of Doppler logs in terms of range and velocity estimate error are directly linked to the physical dimensions and geometry of the transceivers as well as the nature of the pulse transmitted. Beyond a certain transmitted power, distortion of the transmitted pulse due to nonlinear effects is significant. The second harmonic signal generated in that case can be used to estimate velocity in conjunction with the fundamental signal. It has a narrower main lobe and a higher main-lobe-to-sidelobe ratio compared to the fundamental signal. Such geometrical properties contribute to a more localized velocity determination with less perturbations coming from scatterers away from the region of interest. Combining the velocity estimates using the fundamental and second harmonic signals also helps decreasing the velocity estimate error. For a Doppler log transmitting a pulse at 153.6 kHz using 250 W input power with a nominal range of 400 m, the attainable range for the second harmonic signal is estimated to around 221 m.

I. Introduction

The Doppler effect is the principle that acoustic Doppler current profilers (ADCPs) and Doppler velocity logs (DVL) rely on. The DVLs are used to track the speed of a ship or an autonomous underwater vehicle (AUV) over the sea bottom. The ADCPs are an evolution of the DVLs. While they also can track the speed of a ship or an AUV, their main purpose is to map the velocity of the water current by providing water velocity in range cells over a depth profile. By transmitting an acoustic pulse into water and recording the signal that small floating particles or plankton reflect, the ADCP can estimate the frequency shift that the reflected signal undergoes by Doppler effect. This frequency shift is characteristic of the water velocity since backscatterers are assumed to float in the water and move, on average, at the velocity of the water. For speed measurements the ADCP and DVL use the reflection from the sea bottom to estimate the speed of the ship or AUV over the sea bottom. To estimate a three-dimensional velocity the ADCP uses three or four independent acoustic beams pointing at an angle from the vertical and separated from each other. In the four-beam case the "Janus configuration" is often used where the beams are oriented 90° apart from each other in azimuth. One pair of beams is oriented along the longitudinal axis of the ship and is used to estimate the along-track velocity. The other pair is oriented athwartships and is used to estimate the cross-track velocity. In the three-beam case the beams are often placed with 120° separation in azimuth with one beam pointing forward along the ship longitudinal axis [1]. The geometry of these beams is crucial for the performance of the ADCP. Indeed at each depth cell the ADCP estimates an average of the backscatterers velocity over the ensonified depth cell volume. Therefore a narrower beam will define smaller depth cells and more localized velocity estimates. In the case of speed measurements, a narrower beam will produce a smaller footprint on the sea bottom giving similar improvements. Theriault [1] characterized the spatial response of Doppler current profilers in both the three-beam and four-beam cases. The sidelobe levels in these beams are also a source of perturbation. In the case of water velocity measurement the maximum attainable range is affected due to the echo from the part of the sea bottom, or the surface if the instrument is pointing upwards, ensonified by sidelobes [2]. For speed measurements the echo from the sea bottom ensonified by the main lobe is perturbed by the echo from the part of the sea bottom ensonified by sidelobes.

In addition to these geometrical parameters that have to be accounted for in the design, experience has shown that there is an upper limit to the transmitted power above which nonlinear propagation of sound greatly affects the efficiency of the transducers used in the ADCPs [2]. Today's ADCPs are not operated in these upper power ranges. In fishery research the transmitted power to transducers used with echo sounders is also limited to avoid energy loss to frequency bands around higher harmonic frequencies and ensure accurate target strength estimation [3]. However nonlinear propagation of sound has seen many applications in underwater acoustics with parametric arrays [4] and medical imaging with tissue harmonic imaging (THI). The beam of the second harmonic signal used in tissue harmonic imaging shows a lot of beneficial geometrical properties, like a narrower main lobe and a high main-lobe-to-sidelobe ratio, that improve the image produced by echoes filtered around the second harmonic frequency [5]. In addition to previous successful uses of nonlinear sound propagation, the recent developments in transducer technology has led to very

wideband transducers that can technically transmit a pulse and record the echoes filtered around the fundamental and the second harmonic frequencies [6]. This has led us to investigating the possibility of using the second harmonic signal in conjunction with the fundamental signal to improve performance of ADCPs. This solution requires only one transceiver and the maximum range is defined by the maximum attainable range for the second harmonic signal. In addition it combines the geometrical properties of the second harmonic signal and an additional velocity estimate per ping. Using two transducers transmitting at the fundamental and the second harmonic frequencies or one transducer transmitting at the second harmonic frequency with a weighting that reduces sidelobe levels cannot combine all those advantages.

Depending on the type of applications that the ADCP is aimed at, the processing of the received signal differs. Three main types of echo processing are used: incoherent pulse processing, coherent pulse to pulse processing, and broadband signal processing. While incoherent pulse processing allows for a very large range it requires long averaging time to reduce absolute velocity error and is subject to a depth resolution-velocity error trade-off. It is best aimed at deep water low-precision applications. In [7] Theriault studies the performance of an incoherent Doppler profiler. At the opposite end of the scale the coherent pulse to pulse processing gives an excellent space-time resolution but is limited to depths of some tens of meters. It is best suited for shallow water applications requiring high resolution. Lohrmann and Nylund give a description of the performances and operational limitations of a pulse to pulse coherent system in [8]. The broadband signal processing is an intermediate solution that combines the advantages of incoherent and coherent pulse to pulse processing methods. It allows for large ranges in the hundreds of meters and a velocity variance and spatial resolution intermediate between the two first methods. Brumley *et al.* give a performance estimate of broadband signal processing and compare it to the other methods in [9]. To cover all types of applications, we study the advantages of combining the fundamental and second harmonic signals using all three processing methods mentioned.

In the first part of this article we examine the advantages that the geometry of the second harmonic signal beam provides. We show that the narrower main lobe and high main-lobe-to-sidelobe ratio of the second harmonic signal give an echo that is less spread in time than when using the fundamental signal and that the spread in speed estimate is also reduced. This in turn allows for a more precise determination of the time of arrival of the pulse and velocity estimation.

The second part studies the error reduction of the velocity estimate when combining echoes from the fundamental signal and the second harmonic signal for the three main processing methods: incoherent pulse processing, coherent pulse to pulse processing, and broadband signal processing.

In the last part, we use a simulator and a signal budget equation to estimate the maximum range attainable when using the second harmonic signal and find it comparable to the range specifications of commercial ADCPs transmitting at the same frequency.

II. Geometrical properties of the second harmonic signal beam

Propagation of sound is inherently nonlinear. In the second-order approximation for thermoviscous fluids such as water, nonlinear effects translate into a dependency of the sound propagation speed with the medium density [10]. The propagation velocity of sound increases where the medium is compressed and decreases where it expands. Because of that, the pressure peaks of a pulse travel faster than its troughs resulting in a distorted pulse. This distortion translates in the

frequency domain into energy transferred to harmonic frequency bands centered around multiples of the transmitted frequency. At low transmitted power level this energy transfer and the nonlinear effects are negligible but at high transmitted power the part of the signal in the higher harmonic frequency bands can be detected and used. In this paper the second harmonic signal, which is the part of the signal filtered around twice the transmitted frequency, is studied and compared against the fundamental signal, the part of the signal filtered around the transmitted frequency.

A. A narrower main lobe and lower sidelobes

The beam pattern of the second harmonic signal has been compared against the beam pattern of the fundamental signal in numerous papers [11–13]. It exhibits a narrower main lobe and a higher main-lobe-to-sidelobe ratio. A simulation of the pressure lateral beam profiles of the first and second harmonic signals is shown in Fig. 1. It uses a circular transducer of radius 82.5 mm with a transmit frequency of 153.6 kHz and an initial pressure of 100 kPa, which describe a typical ADCP [2]. The other parameters used in the simulations can be found in Table I. The simulation is based on an angular spectrum approach (ASA) and uses an operator splitting method [14, 15]. A pre-defined number of harmonic frequencies are taken into account in the computation that solves the propagation in the frequency domain. The first operator, the linear step, accounts for diffraction and attenuation. It consists of multiplying the spatial Hankel transform of the field at depth z for each frequency by a diffraction operator (Eq. (4) in [14]) and appending the losses due to absorption. The second operator, the nonlinear step, implements a solution to a lossless Burgers equation in the frequency domain (Eq. (3) in [15]). Applying both operators iteratively with a small step size simulates nonlinear propagation from the source plane.

Fig. 1 shows a 3 dB beamwidth of approximately 2.4° for the fundamental signal and 1.6° for the second harmonic signal and a ratio of main lobe to first sidelobe around 17 dB for the fundamental signal and 29 dB for the second harmonic signal. The lateral profile obtained with the same aperture transmitting at twice the frequency, 307.2 kHz, and filtered around the fundamental frequency is also shown in Fig. 1 as a comparison. As expected the 3 dB beamwidth is lower than for the second harmonic signal (1.4°) as well as the main-lobe-to-sidelobe ratio (15 dB).

In this article the examples are based on a piston transducer with a uniform excitation. Doppler logs also use weighted transducers that produce a beam pattern with lower sidelobes at the expense of a wider main lobe. For this kind of transducers the second harmonic signal also exhibits a narrower main lobe and a larger main-lobe-to-sidelobe ratio compared to the fundamental signal. We verified that using a transducer weighted with a Hanning window or a piston transducer with a uniform excitation the use of the second harmonic signal improved the Doppler log performances in a similar fashion.

The drawback of sidelobes in terms of range limitation for water velocity estimation and echo perturbations for travel speed estimation are illustrated in Fig. 2. In the case of water velocity estimation the echo from the bottom is much stronger than the back scattered pulse from volume scatterer limiting the effective vertical range to $z \cos\theta$ where z is the depth and θ the orientation angle of the transducer referred to the vertical [2]. In the case of speed estimation the sidelobes create perturbations for the detection of distance to bottom and increase the area over which velocity is averaged.

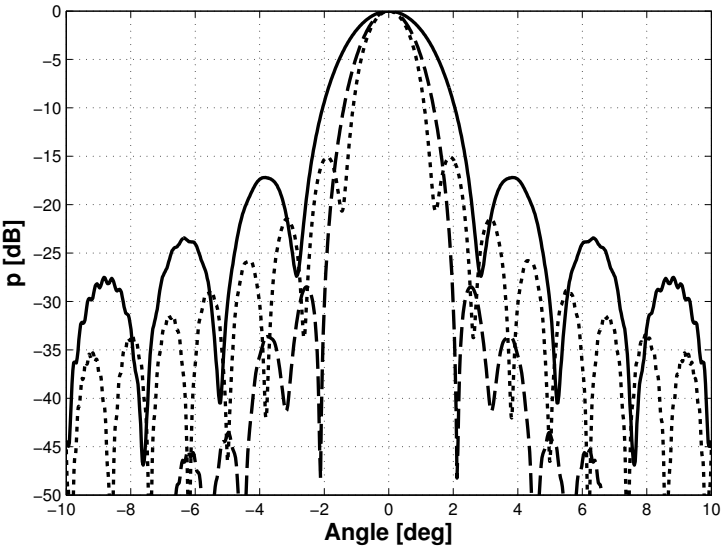

Fig. 1*: Simulated normalized lateral beam profiles for the fundamental signal (solid line), the second harmonic signal (dashed line), and the fundamental signal transmitted at twice the frequency (dotted line) generated by a circular transducer of radius 82.5 mm after 7 m propagation in seawater. The transmitted frequency is 153.6 kHz and 307.2 kHz for the fundamental signals and the input pressure is 100 kPa.*

To illustrate the effects of low sidelobes and a narrow main lobe, we first simulated the sound field created by a circular aperture transmitting a pulse and then estimated the signal received by this same transducer after reflection on a flat bottom. The configuration is the same as shown on Fig. 2 with θ = 30° and z = 7 m. The radius of the transducer is 82.5 mm, the transmitted frequency is 153.6 kHz, and the input pressure is 100 kPa. To first estimate the amplitude of the sound field reaching the sea bottom, the simulator is used to propagate the sound from the transducer to the plane containing the sea bottom. The part of the seafloor considered to compute the reflection of the signal is a square patch large enough to contain the footprint of a conical beam with an opening angle of 30°. Most of the signal energy is contained within this area. A grid is applied on the sea bottom and each element of the grid is assigned the same reflection coefficient. The fundamental and second harmonic signals reaching each grid element are propagated back to the transducer assuming a linear propagation and no absorption loss. Spherical spreading is assumed and the directivity of the transducer is taken into account at reception. For a linear propagation of a pulse of wavelength λ towards a circular piston of radius R the directivity function is given by [16]

$$b_r(\gamma) = \frac{2J_1[(2\pi R/\lambda)\sin\gamma]}{(2\pi R/\lambda)\sin\gamma}, \tag{1}$$

where J_1 is the Bessel function of the first kind of order one and γ is the angle between the main propagation axis of the transducer and the path from center of transducer to the sea bottom grid element. This allows to estimate the amplitude of the signal reflected by each element of the seafloor after reception for the fundamental and second harmonic signals.

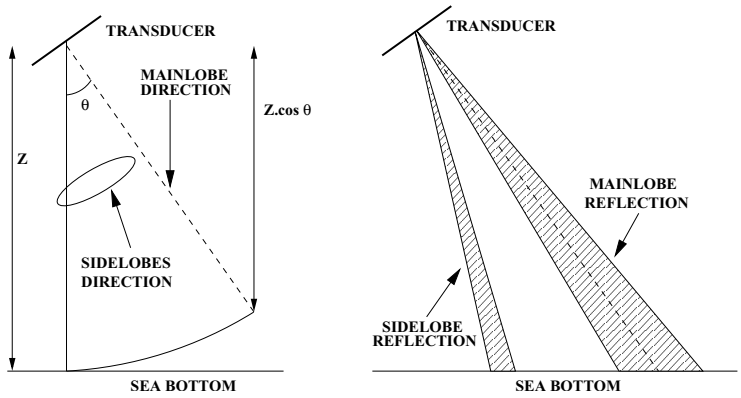

Fig. 2*: Left: range limitation to* $z\cos\theta$ *due to sea bottom reflection in the sidelobes direction when estimating water velocity. Right: increase of beam footprint where velocity is averaged creating larger spread in travel speed estimation.*

In addition to these signal amplitudes, the two-way time delays for each element of the sea bottom grid are computed. Summing the scaled and delayed signals reflected by each grid element gives an estimate of the shape of the recorded echo from the sea bottom. The shape of the echo from the sea bottom area when ensonified by a sinusoidal wave modulated by an envelope with smoothly tapered edges are shown in Fig. 3 for the fundamental signal and the second harmonic signal, respectively. The effects of a wide main lobe and high sidelobe levels are visible as the energy is more spread in time compared to the echo from the second harmonic signal. An easier way to visualize this effect is to compute the cumulative signals energy over time as shown in Fig. 3. The figure also shows the cumulative energy for the fundamental signal of a pulse transmitted at twice the frequency. The signal reaches 10% of its total energy at approximately 10.75 ms and 10.88 ms for the fundamental and second harmonic signals, respectively, while it reaches 90% of its total energy at 11.08 ms and 11.16 ms for the second harmonic and fundamental signals, respectively. The energy build-up in the case of the fundamental signal transmitted at twice the frequency is very close from the case of the second harmonic signal revealing a pulse slightly more compressed in time. This shows that the energy of the second harmonic signal is more concentrated in time allowing a more precise determination of time of arrival of the pulse, and Doppler frequency shift.

This example shows the advantages of a narrower main lobe and a larger main-lobe-to-sidelobe ratio in the case of travel speed estimation. In the case of current velocity estimation the reflecting surface should be replaced by a volume of water determined by a piece of spherical shell which center is the center of the transducer and of thickness $c\tau/2$, where c and τ are the speed of sound and pulse duration, respectively. In that case, the spatial extent of the beam as well as the pulse length determine how the energy is spread in time. The second harmonic signal gives similar advantages compared to the fundamental signal in this case too.

B. Doppler shift spreading

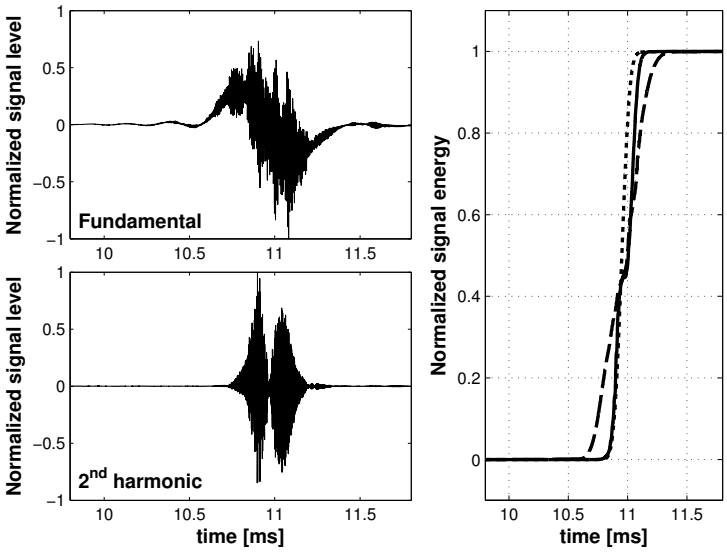

Fig. 3*: Top left: normalized fundamental signal received after echo from the sea bottom patch. Bottom left: normalized second harmonic signal received after echo from the sea bottom patch. Right: signal energy normalized to its maximum value for the fundamental signal (dashed line), the second harmonic signal (solid line), and the fundamental signal transmitted at twice the frequency (dotted line) over time.*

The received echo can be seen as a collection of reflections from point scatterers. Depending on the position of these point scatterers in the beam, the corresponding echo will have a varying Doppler shift. Fig. 4 shows the wave vector $\mathbf{k}$ of the reflected signal from a point scatterer P propagating back to the transducer, together with the particle velocity vector $\mathbf{v}$ assumed in the horizontal plane. In this figure x is the azimuth direction and y is the elevation direction.

The Doppler frequency shift produced by this point scatterer can be written as

$$f_d = \frac{\mathbf{k} \cdot \mathbf{v}}{\pi}. \tag{2}$$

Equation (2) shows that if the velocity vector $\mathbf{v}$ is assumed constant in the horizontal plane, the Doppler frequency shift differs for each point scatterer within the beam due to the variations in the direction of $\mathbf{k}$. This generates a spread in the Doppler shift at reception of the signal. A beam with a lower spatial extent should suffer from less spread in the Doppler shift.

Using the results from the simulation described in the previous section that estimates the amplitude of the signal reflected by a rectangular patch of sea bottom, the Doppler shift is calculated for each grid element. Each Doppler shifted signal is propagated back to the transducer also as previously described. Fig. 5 shows the spread in velocity estimate at 7 m depth for the fundamental and second harmonic signals as well as for the fundamental signal transmitted at twice the frequency when $|\mathbf{v}|$ = 2 m/s and the velocity vector $\mathbf{v}$ is parallel to the elevation direction, that is $v_x = 0$ in Fig. 4. According to (2) a spread in the Doppler frequency shift can be due to variations of the norm of the velocity vector or of the angle it makes with the wave vector $\mathbf{k}$. If the angle between

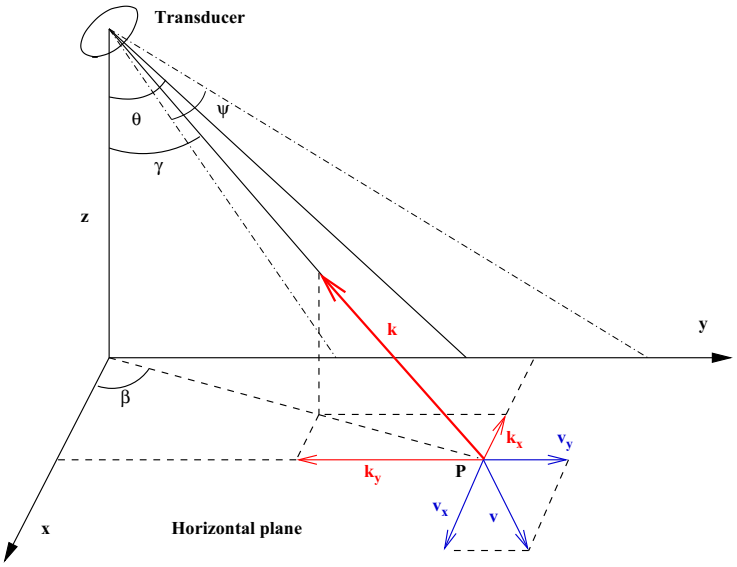

Fig. 4: *Wave number* $\mathbf{k}$ *of reflected signal by point scatterer* P*. The velocity vector* $\mathbf{v}$ *is assumed constant in the horizontal plane at depth* z*.*

the velocity and wave vectors is assumed equal to $\pi/2 + \theta$, the nominal Doppler shift is

$$f_{dNOM} = -\frac{|\mathbf{k}||\mathbf{v}|}{\pi} \sin\theta, \tag{3}$$

which corresponds to approximately -208 Hz and -415 Hz for the fundamental and second harmonic signals, respectively.

For all three signals the Doppler shift spectrum shows a main lobe and a decay with sidelobes. The main lobe for the fundamental signal is wider than for the second harmonic signal and the sidelobe levels are higher. The main lobe for the fundamental signal transmitted at twice the frequency is very close to the main lobe for the second harmonic signal but its sidelobe levels are higher. The shape of the Doppler shift spectra is closely related to the beam patterns of the transducer at fundamental and second harmonic frequencies as mentioned in [17].

The Doppler shift spectrum has a 3-dB bandwidth of about 14.9 Hz and 15.7 Hz for the fundamental and second harmonic signals, respectively, which corresponds to 14.4 cm/s and 7.6 cm/s when using (3). This shows that the geometrical properties of the second harmonic signal beam improve the precision of the velocity estimate. If the effect of the sidelobes in the Doppler spectrum are ignored, using the second harmonic signal produces the same spread in the Doppler shift as the fundamental signal transmitted at twice the frequency. However using the components around the fundamental and second harmonic frequencies of one received echo produces two velocity estimates per ping that can be combined for better precision as shown in the next section. This cannot be achieved by using only the fundamental signal transmitted at twice the frequency.

III. Velocity estimation error

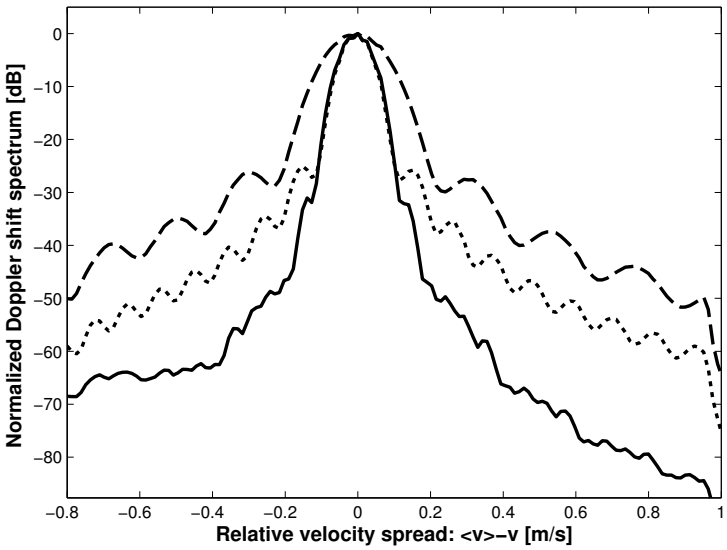

Fig. 5*: Normalized Doppler shift spectrum in dB at 7 m depth for the fundamental signal (dashed line), the second harmonic signal (solid line), and the fundamental signal transmitted at twice the frequency (dotted line) plotted against corresponding velocity spread when* $|\mathbf{v}|$ *= 2 m/s and* $\mathbf{v}$ *is parallel to the elevation direction.*

A. Incoherent Doppler profilers

One way to determine the velocity from the echo of the sea bottom or from a depth cell is to compute the frequency spectrum of the received signal and determine the signal frequency after Doppler shift. From the frequency, the radial velocity can be calculated using:

$$f_d = \frac{2fv}{c}, \tag{4}$$

where f_d is the Doppler frequency shift, f is the frequency of the transmitted signal, v is the sought radial component of the velocity, and c is the speed of sound. To determine the velocity in the depth cell situated at range r, the signal is time gated at time $t_r = 2r/c$ before frequency analysis. The size of the time window centered around t_r is usually the same as the transmitted pulse length T. This gives a range resolution of $L = cT/2$ and a frequency spectrum bandwidth of $1/T$. A lower limit for the error variance of an estimator for f_d is given by the Cramér-Rao bound. In the case of incoherent processing, and when the correlation time of the reverberation signal is assumed equal to the pulse length this limit is [18]

$$\sigma_f^2 = \frac{1}{(2\pi T)^2}\frac{1}{N_v}\frac{1}{I_v(\mathrm{SNR})}, \tag{5}$$

where σ_f is the standard deviation of the frequency estimator, N_v is number of independent depth cells considered during the processing time, and $I_v(\mathrm{SNR})$ is defined as

$$I_v(\mathrm{SNR}) = \frac{2}{\sqrt{\ln 2}} \int_{-\sqrt{\ln 2}}^{\sqrt{\ln 2}} \frac{x^2 dx}{\left[1 + \exp(x^2)/(\mathrm{SNR}\sqrt{2})\right]^2}. \tag{6}$$

The signal-to-noise ratio, SNR, is defined as the ratio of the energy of the reverberated signal to the noise energy where the noise bandwidth was assumed equal to the transmitted signal bandwidth, in this case $1/T$. Using (4), the standard deviation lower bound of the velocity estimate can be written as:

$$\sigma_v = \frac{c\sigma_f}{2f} = \frac{c}{4\pi f T} \frac{1}{\sqrt{N_v I_v(\mathrm{SNR})}} \tag{7}$$

The relation between the lower bounds for the standard deviation of the velocity estimate in the case of the fundamental signal σ_{v1} and in the case of the harmonic signal σ_{v2} is

$$\sigma_{v2} = \frac{\sigma_{v1}}{2} \sqrt{\frac{I_v(SNR_1)}{I_v(SNR_2)}} \tag{8}$$

where SNR_1 and SNR_2 are the signal-to-noise ratios for the fundamental and second harmonic signals, respectively. The function $I_v(\mathrm{SNR})$ tends towards 0 when SNR is very low, and towards 1 when SNR is very high. This means that in the case of high SNR for both the fundamental and second harmonic signals $\sigma_{v2} \approx 0.5\ \sigma_{v1}$. As an example, SNR_2 is taken equal to 15 dB, the lower bound of the useful range of signal-to-noise ratio in the case of an incoherent system [9], and SNR_1 is assumed to be 10 dB higher and equal to 25 dB. The function I_v was evaluated for both values of SNR_1 and SNR_2

$$I_v(SNR_1) \approx 0.85,\ I_v(SNR_2) \approx 0.80,\ \sigma_{v2} \approx 0.52\ \sigma_{v1}. \tag{9}$$

This shows that the standard deviation of the velocity estimate is reduced when using the second harmonic signal instead of the fundamental signal. Such a reduction improves the measurements by reducing the required averaging times, permitting the observation of smaller time scale effects. This conventional method assumes that echoes from separate pings are not correlated. It is called "incoherent" in opposition to the "coherent" method that evaluates the phase variations between two consecutive pulses.

B. Coherent Doppler profilers

In the "coherent" processing method the system transmits a series of single pulse pings with a shorter time interval and observes the phase changes from ping to ping at each range cell. By sampling each ping at the same depth the phase variation from ping to ping can be used to determine the velocity of the scatterer at that depth [19]

$$v = \frac{c\,(d\Phi/dt)}{4\pi f}, \tag{10}$$

where $d\Phi/dt$ is the time derivative of the signal phase. For this method, the echoes need to be coherent which means the time interval between consecutive recorded echoes should be below the decorrelation time. The signal phase variation can be estimated using for instance the covariance method [19,20]. In this method the echo from each consecutive pulse is sampled at fixed range r so that the same set of scatterers contribute to the selected part of the echo. The time interval between each sample is noted $\tau = 2r/c$ and the sampling frequency is the pulse repetition frequency (PRF). In this case the pulse length does not determine the bandwidth of the frequency spectrum and the standard deviation of the velocity estimate. The spectral bandwidth in this method, called the Doppler bandwidth and noted B thereafter, is due to the sources of phase noise "like turbulence within the sample volume, beam divergence, finite scatterer residence time, and acceleration during the averaging period" [9] and is greatly reduced compared to the signal bandwidth. To explain this we use the theory presented in [21] and start by defining $g(t)$ the analytical signal corresponding to the received signal. When sampling the series of pings at intervals τ we can define the two dimensional signal $z(s,t) = g(s+t)$ as the return after delay t from the pulse transmitted at time s. The time s is discrete and its values are incremented by τ. A two-dimensional Fourier transform of $z(s,t)$ can therefore be computed and gives a spectrum as a function of the range frequency f_r and Doppler frequency f_s. The obtained spectrum has a bandwidth along the range frequency equal to the bandwidth of the transmitted signal, $1/T$, but its bandwidth along the Doppler frequency, B, does not depend on signal duration. The fact that the standard deviation of the velocity estimate does not depend of the signal length allows one to transmit signals of short duration and improve the spatial resolution $L = cT/2$.

In [22] Zrnić gives an expression for the variance of the mean frequency estimate using the covariance method in the case where a Gaussian shaped power spectrum for the received echoes is assumed, and successive pairs of echoes are correlated. For large decorrelation time compared to ping interval, and even greater observation time, this expression can be simplified to

$$\sigma_f^2 \approx \frac{2\pi B\tau\sqrt{\pi}(\tau_c/\tau)^2 + 1/\mathrm{SNR}^2 + 2/\mathrm{SNR}}{8\pi^2 M\tau_c^2} \quad \text{when} \quad M\tau \gg 1/(2\pi B) \gg \tau, \tag{11}$$

where $1/(2\pi B)$ is the decorrelation time, M the number of pings, and τ_c is the time lag at which the auto-correlation is evaluated ($0 \leq \tau_c \leq \tau$). Two limit cases can be considered. In the first case we assume $1/\mathrm{SNR} \gg 2\pi B\tau$ and in the second case $1/\mathrm{SNR} \ll 2\pi B\tau$. Considering the first case, σ_f can be approximated to

$$\sigma_f^2 \approx \frac{1/\mathrm{SNR}^2 + 2/\mathrm{SNR}}{8\pi^2 M\tau_c^2}. \tag{12}$$

Using (4), the relation between the standard deviation for the velocity estimates obtained with the fundamental and second harmonic signals is

$$\sigma_{v2} = \frac{\sigma_{v1}}{2}\frac{\sqrt{1/\mathrm{SNR}_2^2 + 2/\mathrm{SNR}_2}}{\sqrt{1/\mathrm{SNR}_1^2 + 2/\mathrm{SNR}_1}}. \tag{13}$$

In the second case, we have [9]

$$\sigma_f^2 \approx \frac{\pi^{-1/2}B}{4M\tau} \tag{14}$$

and

$$\sigma_{v2} = \frac{\sigma_{v1}}{2}\sqrt{\frac{B_2}{B_1}}, \tag{15}$$

where B_1 and B_2 are the Doppler bandwidth in the case of the fundamental and second harmonic signals, respectively.

In the first case, the relation between the standard deviations σ_{v1} and σ_{v2} is very much dependent of the signal-to-noise ratios SNR_1 and SNR_2. As an example, if $\mathrm{SNR}_1 = 25$ dB and $\mathrm{SNR}_2 = 15$ dB we have

$$\sigma_{v2} \approx 0.92\,\sigma_{v1}. \tag{16}$$

In the second case assuming the source of phase noise only comes from the beam divergence, the Doppler bandwidth is approximately proportional to the product of the beamwidth by the transmitted frequency. Calling ξ_1 and ξ_2 the beamwidth for the fundamental and second harmonic signals, respectively, we can write

$$\sigma_{v2} = \sigma_{v1}\sqrt{\frac{\xi_2}{2\xi_1}} \tag{17}$$

Using the 3-dB beamwidths computed in Sec. II for ξ_1 and ξ_2 we have

$$\sigma_{v2} = \sigma_{v1}\sqrt{\frac{1.6}{2 \times 2.4}} \approx 0.58\,\sigma_{v1}. \tag{18}$$

This is valid in the simple case where the only source of phase noise considered is the beam divergense. If for instance the beam divergence is altered by turbulences, the dependence of the beamwidth is reduced and the ratio of the standard deviations gets closer to $1/\sqrt{2}$.

C. Estimator redundancy

When using both the fundamental and second harmonic signals, two velocity estimates can be computed. When the two estimates can be considered as independent statistical processes averaging both gives a combined variance

$$V_c = \frac{V_{v1} + V_{v2}}{4}, \tag{19}$$

where V_c, V_{v1}, and V_{v2} are the variances of the combined velocity estimates, the estimate using the fundamental signal, and the estimate using the second harmonic signal, respectively. In the case of incoherent pulses both estimates are independent and using the results of the numerical example in (9) we can write

$$\sigma_c \approx 0.56\,\sigma_{v1}, \tag{20}$$

where σ_c is the standard deviation of the combined estimate. In this particular case the variance when combining estimates from the fundamental and the second harmonic signals is slightly higher than when using the second harmonic signal alone.

In the case of coherent pulse processing since the beam geometries and the scatterer response are different from the fundamental signal to the second harmonic signal the two estimates can be

considered independent. Using (16) we can write in the case of low SNR:

$$\sigma_c \approx 0.68\, \sigma_{v1}. \tag{21}$$

In the case of high SNR, using (18), we have

$$\sigma_c \approx 0.58\, \sigma_{v1}. \tag{22}$$

In this case the standard deviation of the velocity estimate combining the fundamental and the second harmonic signals is lower than when using the second harmonic signal alone if the signal-to-noise ratio is low.

To summarize, the standard deviation for the velocity estimate is improved when using the second harmonic signal in place of the fundamental signal for sufficiently large SNR. As the SNR increases, this reduction in standard deviation increases. Combining the fundamental signal with the second harmonic signal can give an estimate with a further reduced standard deviation provided that the SNR does not reach a higher limit above which the standard deviation gets larger than the one obtained using the second harmonic signal only.

A limitation when using the combined estimate in the coherent case comes from the ambiguity velocity. Since the phase cannot be determined beyond the limits $[-\pi, \pi]$ without ambiguity, we get from (10) the maximum radial velocity that can be detected without ambiguity [23]

$$v_a = \frac{c}{4f\tau}. \tag{23}$$

This maximum velocity is decided by the frequency of the second harmonic signal and is therefore halved compared to the ambiguity velocity when using the fundamental signal only. Using the combined estimate or the estimate using the second harmonic signal together with the estimate using the fundamental signal gives a reduced standard deviation and the same ambiguity velocity as when using the fundamental signal alone.

D. Broadband Doppler profiler

To achieve coherent pulse to pulse processing, the inter-pulse delay τ must be limited to ensure a phase difference below π and to avoid echo decorrelation. In addition the echo from the previous pulse must have died out before the next pulse can be transmitted limiting the maximum attainable range to $r_a = c\tau/2$. This gives the range-velocity ambiguity relation

$$r_a v_a = \frac{c\tau}{2}\frac{c}{4f\tau} = \frac{\lambda c}{8}. \tag{24}$$

This is the main limitation for the coherent pulse to pulse signal processing. These limitations on range and velocity could be removed if the time between pulses could be smaller than the propagation time to maximum range. This can be done if the system receives echoes from two or more pulses for each ping. This concept lies behind the broadband Doppler current profilers [9]. Two pulses of duration T_p are sent with a time interval T_0. If T_0 is chosen small, the depth cell size $cT_0/2$ is reduced and the ambiguity velocity $c/(4fT_0)$ is increased. The ping interval τ can be

as large as necessary and the range is only limited by the SNR. Using the covariance method, the variance of the velocity estimate per ping in this case is inversely proportional to the averaging time-bandwidth product T_a/T_p, where T_a is the time for which covariance samples are averaged [9]. It would then be natural to try to reduce T_p to decrease the variance per ping but doing so would shorten the pulse and reduce the SNR impairing the maximum attainable range [24].

To increase the signal bandwidth without excessively decreasing the signal duration and SNR, phase coding can be used. Coded pulses composed of many closely spaced elements are transmitted. Such signals can have a long duration allowing to transmit the same energy as long uncoded pulses while providing a large bandwidth as short uncoded pulses. When phase coding is used, a simplified expression of the variance of the velocity estimate per ping given by Zrnić [22] is presented in [9]. For a two-pulse transmission and $T_a \leq T_0$ it is

$$V_f = \frac{1}{(2\pi T_0)^2} \left(\frac{1}{\rho^2} - 1 \right) \frac{C^2}{2M_a}, \tag{25}$$

where V_f is the Doppler frequency estimate variance, C is a correction coefficient for non-ideal aspects of the code and processing, M_a is the number of code elements in T_a, and ρ is the auto-correlation coefficient at lag T_0. Since the phase of the second harmonic signal can be assumed to be twice the phase of the fundamental signal, a phase coding modulating the phase of the fundamental signal with 0° and 180° is equivalent to no phase coding for the second harmonic signal. Assuming that coded pulses are contiguous with a pulse separation T_0, in the case of a two-pulse transmission the second harmonic signal is a sine pulse of length $2T_0$. Brumley *et al.* mention a numerical example of variance calculation in the case of a broadband coded pulse with a two-pulse transmission [9]. In their calculation $f = 600$ kHz, $M_a = 118$, $v_a = c/(4fT_0) = \pm 40$ cm/s, $\rho = 0.5$, and $C = 1.5$, which gives $V_f \approx 305$ Hz^2 with $c = 1479$ m/s and a speed standard deviation around 2.2 cm/s. If the second harmonic signal pulse is processed incoherently, using (7) it leads to a velocity standard deviation

$$\sigma_v = \frac{c}{4\pi 2f 2T_0} \frac{1}{\sqrt{N_v I_v(\mathrm{SNR}_2)}} = \frac{v_a}{4\pi \sqrt{N_v I_v(\mathrm{SNR}_2)}}. \tag{26}$$

Choosing $N_v = 1$ and $\mathrm{SNR}_2 = 15$ dB, we get

$$I_v(\mathrm{SNR}_2) \approx 0.80 \quad \text{and} \quad \sigma_v \approx 3.56 \text{ cm/s}. \tag{27}$$

Averaging both estimates as explained in the previous section gives the combined velocity standard deviation

$$\sigma_c = \frac{\sqrt{2.2^2 + 3.56^2}}{2} \approx 2.09 \text{ cm/s}, \tag{28}$$

which shows a slight reduction by a factor 0.95 compared to the velocity standard deviation obtained when using the fundamental signal only.

IV. Range performance

The question of the range performance when using the second harmonic signal obviously has to be addressed. The maximum range at which an ADCP can be used is determined when, due

to geometrical spreading and attenuation in seawater, the echo strength has dropped to a level comparable to the noise level [2]. Since the intensity of the transmitted pulse around the second harmonic frequency is much lower than around the fundamental frequency, it is expected that the maximum attainable range should be lower when using the second harmonic signal.

To estimate the range limitations, the KZKTexas Code [25, 26], which operates in the time domain, is used to simulate the pressure field. This simulator is equivalent to our implementation of the ASA simulator mentioned in Sec. II but is slightly faster and allows us to use a lateral sample size that increases with depth of propagation. This is well adapted to our case where we seek the pressure field contained within an opening angle along the propagation depth. The aim is to estimate the sound intensity of a pulse received by an ADCP transducer after being reverberated by the scatterers contained in the sea and filtered around the fundamental or the second harmonic frequencies. The pressure field is simulated up to a range of 500 m and the extent of the beam patterns is limited to 20° on each side of the main propagation axis where most of the energy is. This means that the depth cell at range r is modelled as a cylinder of diameter $D = 2r \tan 20°$ and height $cT/2$, where T is the pulse duration. The scatterer density is characterized by the volume scattering strength s_v which defines the part of the incident energy reverberated by each unit of volume. The volumic scatterers are assumed to reverberate the energy in an omnidirectional way and the propagation back to the receiver is assumed to be linear. Not all of this reflected energy is received due to the directivity of the receiver, so the beam pattern of the transducer at reception has to be taken into account. The reverberated intensity can therefore be defined for each depth cell at range r:

$$I_{rev}(z) = \int_0^{D/2} \left[b_t(z,r) b_r[\mathrm{atan}(r/z)] \frac{p(z)}{p_{ref}} \right]^2 s_v 2\pi \; r \; dr \; cT/2, \tag{29}$$

where $b_t(z,r)$ is the normalized beam pattern at transmission determined by simulation, b_r is the beam pattern at reception defined in (1), $p(z)$ is the axial pressure of the fundamental or second harmonic signal at range z, and p_{ref} is a reference pressure equal to 1 μPa. In (29) the intensity is referred to a reference intensity corresponding to a plane wave of pressure 1 μPa and the axial pressure $p(z)$ as well as the lateral profile $b_t(z,r)$ are computed by the KZKTexas code taking into account absorption and diffraction during transmission. Using the decibel (dB) notation we define the reverberation level RL as $\mathrm{RL} = 10 \log(I_{rev})$.

When the reverberated signal is travelling back to the receiver, the transmission losses TL due to geometrical spreading and absorption have to be taken into account. Considering a spherical spreading and an attenuation coefficient α in dB/m, we have using [27]

$$\mathrm{TL} = 20 \log z + \alpha z. \tag{30}$$

The total echo level EL recorded at the receiver is $\mathrm{EL} = \mathrm{RL} - \mathrm{TL}$.

Fig. 6 shows the echo level for fundamental and second harmonic signals in the case of a circular transducer of radius $R = 82.5$ mm transmitting a pulse at frequency 153.6 kHz with an input pressure $p_0 = 131$ kPa and receiving an echo from volumic reverberation. It also shows the echo level for the fundamental signal of a circular piston of radius $R = 66.5$ mm transmitting a pulse at the frequency of the second harmonic signal, 307.2 kHz with an input pressure of $p_0 = 93$ kPa. This is to compare the range performance of the second harmonic signal against the fundamental

signal at the same frequency. The value of the other simulation parameters are presented in Table I and are based on existing transducer data [2]. Typical values for the volume scattering strength were chosen from measurements of the San Diego coast [28]. It appears that we compare range performance for different transducer size and different input power but this is done to compare existing hardware. Had we compared the range performance using the same transducer size and input power only doubling the transmit frequency it would not have been representative of existing products.

Table I*: Parameters used to compute the echo level and to estimate the pressure profiles along depth using the simulator. The parameters marked with a † are used to compute the absorption in seawater according to the formula given in [29]*

Parameter	Value	
Source radius (R)	82.5 mm	66.5 mm
Frequency (f)	153.6 kHz	307.2 kHz
Input pressure (p_0)	131 kPa	93 kPa
Input power (P)	250 W	80 W
Volume scattering strength ($S_v = 10 \log s_v$)	-86 dB	-80 dB
Water density (ρ_0)	998 kg/m^3	
Sound speed (c)	1479 m/s	
Nonlinearity coefficient (β)	3.5	
Attenuation (α)		
Salinity†	34 ppt	
Depth†	100 m	
Temperature†	10°C	
pH†	7.7	
$\Rightarrow$ 0.045 dB/m at 153.6 kHz		
$\Rightarrow$ 0.076 dB/m at 307.2 kHz		
Pulse duration (T)	2 ms	

According to [2] the nominal range for an ADCP of radius $R = 82.5$ mm transmitting at 153.6 kHz with an input power of 250 W is 400 m. The horizontal line in Fig. 6 that intersects the echo level of the fundamental signal at 400 m range gives an estimate of the signal strength needed at reception. This level is around 35 dB. According to [30] the ambient noise above 100 kHz increase as 20 $\log f$ which places the minimum echo level for the second harmonic signal 6 dB above the 35 dB level required for the fundamental signal. For a minimal echo level around 41 dB, the maximum attainable range when using the second harmonic signal is around 221 m and around 243 m for the fundamental signal at 307.2 kHz.

In this particular case the results show that the range performance for the second harmonic signal is almost as good as for the fundamental signal transmitting at the second harmonic frequency, 307.2 kHz.

Although the obtained numbers for the maximum attainable range depend on the assumptions made for the model and on parameter values such as the reverberation strength or the the input pressure they show that there is a possible use for the second harmonic signal to improve the velocity

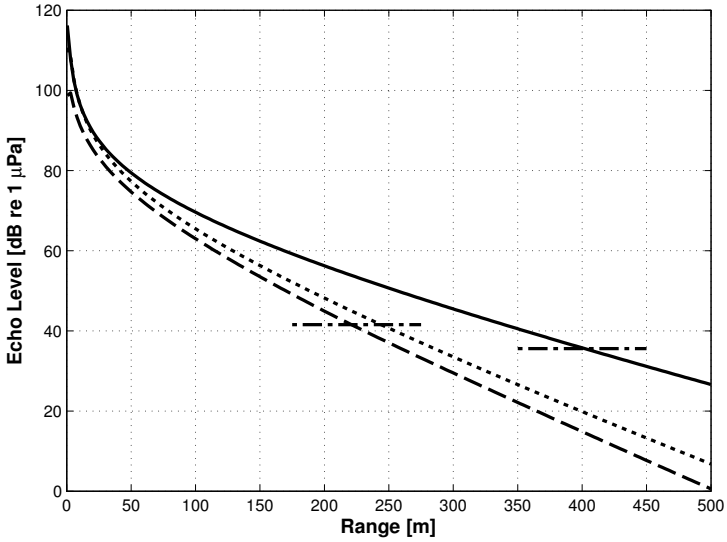

Fig. 6*: Echo level for the fundamental signal (solid line) and the second harmonic signal (dashed line) for a piston transducer of radius $R = 82.5$ mm transmitting a 2 ms pulse at 153.6 kHz with input pressure $p_0 = 131$ kPa, and echo level for fundamental signal (dotted line) for a piston transducer of radius $R = 66.5$ mm transmitting a 2 ms pulse at 307.2 kHz with input pressure $p_0 = 93$ kPa. The horizontal dash-dotted lines represent the echo level for the fundamental signal at 153.6 kHz at 400 m range (right most line) and the echo level 6 dB above this level (left most line). The intersections of the left most line with the echo levels for the second harmonic signal and fundamental signal at 307.2 kHz give the maximum attainable range in both cases.*

estimate given by commercial ADCPs.

V. Conclusions

In this article we have given quantitative proofs that the geometrical properties of the second harmonic signal give a more precise estimate of current or ship velocity compared to when using the fundamental signal with ADCPs. The narrower main lobe and larger main-lobe-to-sidelobe ratio allow to ensonify a smaller volume and reduce echoes from scatterers not situated in the main propagation direction. This in turn gives an echo more compressed in time and a smaller spread in Doppler frequency shift, which allows a better determination of the distance to scatterers and velocity estimate.

We have also shown that provided the signal-to-noise ratio is high enough using the second harmonic signal improves the standard deviation of the velocity estimate compared to when the fundamental signal is used. A numerical example showed that the standard derivation can be improved by a factor 0.52 when the echo is processed incoherently. Combining the estimates from the echo filtered around the fundamental and the second harmonic frequencies can also further decrease the standard deviation of the velocity estimate. Numerical examples show that the estimator redundancy decreases the standard deviation by a factor 0.68 in the case of pulse to pulse coherent processing and 0.95 in the case of broadband signal processing.

Finally the maximum attainable range for the second harmonic signal was estimated using a simulation of the pressure field and a signal budget equation. For a range limitation of 400 m for the fundamental signal transmitted at 153.6 kHz, the maximum attainable range using the second harmonic signal at 307.2 kHz is around 221 m for a piston transducer with uniform excitation.

All these properties combined with the new transducers technologies allowing one to receive the echo filtered both around the fundamental and the second harmonic frequencies show that the velocity estimates provided by ADCPs could be improved. Part of the benefits of combining echoes at two different frequencies is that it doubles the amount of information per ping.

The present paper only studies the case of 180-degree phase shift coding for broadband Doppler profilers that leads to no coding for the second harmonic signal. Other coding using 90-degree phase shift would result to a coded pulse at the second harmonic frequency. Although it is hard to estimate the value of the correction coefficient for the non-ideal aspect of the obtained code, the variance of the second harmonic estimate should be improved compared to an incoherent processing as presented. A possibility for future work could be the search for a coded pulse that would have similar properties when filtered around the fundamental and second harmonic frequencies. Trials at sea to validate the feasibility of the method is another possible future work.

Bibliography

[1] K. Theriault, "Incoherent multibeam Doppler current profiler performance: Part II–Spatial response," *IEEE J. Oceanic Eng.*, vol. 11, no. 1, pp. 16–25, Jan. 1986.

[2] R. Lee Gordon, *Acoustic Doppler Current Profiler Principles of Operation A Pracitcal Primer*, 2nd ed., RD Instruments, San Diego, CA, Jan. 1996.

[3] F. E. Tichy, H. Solli, and H. Klaveness, "Non-linear effects in a 200-kHz sound beam and the consequences for target-strength measurement," *ICES J. Mar. Sci.*, vol. 60, pp. 571–574, 2003.

[4] L. Bjørnø, "Forty years of nonlinear ultrasound," *Ultrasonics*, vol. 40, no. 1-8, pp. 11–17, 2002.

[5] F. A. Duck, "Nonlinear acoustics in diagnostic ultrasound," *Ultrasound Med. Biol.*, vol. 28, no. 1, pp. 1–18, 2002.

[6] B. Horvei and K. E. Nilsen, "A new high resolution wideband multibeam echo sounder for inspection work and hydrographic mapping," in *Procs. OCEANS 2010 MTS/IEEE*, Seattle, WA, Sep. 2010, pp. 1–7.

[7] K. Theriault, "Incoherent multibeam Doppler current profiler performance: Part I–Estimate variance," *IEEE J. Oceanic Eng.*, vol. 11, no. 1, pp. 7–15, Jan. 1986.

[8] A. Lohrmann and S. Nylund, "Pure coherent Doppler systems - how far can we push it?" in *Proc. IEEE/OES/CMTC 9th Working Conf. Current Meas. Tech.*, Charleston, SC, Mar. 2008, pp. 19–24.

[9] B. Brumley, R. Cabrera, K. Deines, and E. Terray, "Performance of a broad-band acoustic Doppler current profiler," *IEEE J. Oceanic Eng.*, vol. 16, no. 4, pp. 402–407, Oct. 1991.

[10] M. F. Hamilton and C. L. Morfey, "Model equations," in *Nonlinear Acoustics*, M. F. Hamilton and D. T. Blackstock, Eds. San Diego: Academic Press, Dec. 1998, ch. 3, pp. 41–63.

[11] T. Muir, "Nonlinear effects in acoustic imaging," *Acoust. Imag.*, vol. 9, pp. 93–109, 1980.

[12] M. Hamilton, J. Tjøtta, and S. Tjøtta, "Nonlinear effects in the farfield of a directive sound source," *J. Acoust. Soc. Am.*, vol. 78, no. 1, pp. 202–216, Jul. 1985.

[13] V. Humphrey, "Nonlinear propagation in ultrasonic fields: measurements, modelling and harmonic imaging," *Ultrasonics*, vol. 38, pp. 267–272, 2000.

[14] P. T. Christopher and K. J. Parker, "New approaches to the linear propagation of acoustic fields," *J. Acoust. Soc. Am.*, vol. 90, no. 1, pp. 507–521, Jul. 1991.

[15] ——, "New approaches to nonlinear diffractive field propagation," *J. Acoust. Soc. Am.*, vol. 90, no. 1, pp. 488–499, Jul. 1991.

[16] R. J. Urick, "Properties of transducer arrays: directivity index," in *Principles of underwater sound*, 3rd ed., R. J. Urick, Ed. McGraw-Hill Book Company, 1983, ch. 3, pp. 31–70.

[17] P. Denbigh, "Ship velocity determination by Doppler and correlation techniques," in *Proc. Inst. Elect. Eng. F*, vol. 131, no. 3. IEE, Jun. 1984, pp. 315–326.

[18] Y. Doisy, "Theoretical accuracy of Doppler navigation sonars and acoustic Doppler current profilers," *IEEE J. Oceanic Eng.*, vol. 29, no. 2, pp. 430–441, Apr. 2004.

[19] L. Zedel, A. Hay, R. Cabrera, and A. Lohrmann, "Performance of a single-beam pulse-to-pulse coherent Doppler profiler," *IEEE J. Oceanic Eng.*, vol. 21, no. 3, pp. 290–297, Jul. 1996.

[20] K. Miller and M. Rochwarger, "A covariance approach to spectral moment estimation," *IEEE Trans. Inform. Theory*, vol. 18, no. 5, pp. 588–596, Sep. 1972.

[21] D. Avitzour, "SNR/bandwidth tradeoff in coherent radar sampling," *IEEE Trans. Aerosp. Electron. Syst.*, vol. 26, no. 2, pp. 403–405, 1990.

[22] D. Zrnić, "Spectral moment estimates from correlated pulse pairs," *IEEE Trans. Aerosp. Electron. Syst.*, vol. AES-13, no. 4, pp. 344–354, Jul. 1977.

[23] A. Hay, L. Zedel, R. Craig, and W. Paul, "Multi-frequency,pulse-to-pulse coherent Doppler sonar profiler," in *Proc. IEEE/OES/CMTC 9th Working Conf. Current Meas. Tech.* Charleston, SC: IEEE, Mar. 2008, pp. 25–29.

[24] P. Wanis, B. Brumley, J. Gast, and D. Symonds, "Sources of measurement variance in broadband acoustic Doppler current profilers," in *Procs. OCEANS 2010 MTS/IEEE*, Seattle, WA, Sep. 2010.

[25] Y. Lee, R. Cleveland, and M. Hamilton, "KZKTexas," http://people.bu.edu/robinc/kzk/, date last viewed May 30, 2012, Oct. 1998.

[26] Y. Lee and M. Hamilton, "Time-domain modeling of pulsed finite-amplitude sound beams," *J. Acoust. Soc. Am.*, vol. 97, pp. 906–917, 1995.

[27] R. J. Urick, "Propagation of sound in the sea: transmission loss, I," in *Principles of underwater sound*, 3rd ed., R. J. Urick, Ed. McGraw-Hill Book Company, 1983, ch. 5, pp. 99–146.

[28] K. L. Deines, "Backscatter estimation using broadband acoustic Doppler current profilers," in *Proceedings of the IEEE Sixth Working Conference on Current Measurement*, San Diego, CA, Mar. 1999, pp. 249–253.

[29] M. A. Ainslie and J. G. McColm, "A simplified formula for viscous and chemical absorption in sea water," *J. Acoust. Soc. Am.*, vol. 103, no. 3, pp. 1671–1672, Mar. 1998.

[30] R. J. Urick, "The noise background of the sea: ambient-noise level," in *Principles of underwater sound*, 3rd ed., R. J. Urick, Ed. McGraw-Hill Book Company, 1983, ch. 7, pp. 202–236.

Paper III

Nonlinear acoustic wave equations with fractional loss operators

F. Prieur and S. Holm

Journal of the Acoustical Society of America, vol. 130, no. 3, pp. 1125-1132, September 2011.

Nonlinear acoustic wave equations with fractional loss operators

F. Prieur and S. Holm

Abstract— Fractional derivatives are well suited to describe wave propagation in complex media. When introduced in classical wave equations, they allow a modeling of attenuation and dispersion that better describes sound propagation in biological tissues. Traditional constitutive equations from solid mechanics and heat conduction are modified using fractional derivatives. They are used to derive a nonlinear wave equation which describes attenuation and dispersion laws that match observations. This wave equation is a generalization of the Westervelt equation, and also leads to a fractional version of the Khokhlov-Zabolotskaya-Kuznetsov and Burgers' equations.

I. Introduction

Fractional derivatives, whether the formal name is used or not, have been used for modeling heat transfer or diffusion [1, 2],seismic data [3], and sound wave propagation [4–6], only to name a few. They allow the description of the physics of complex media in solid and fluid mechanics. When modeling sound propagation, the use of fractional derivatives leads to models that better describe observations of attenuation and dispersion [7]. The wave equation for viscous losses involving integer order derivatives only, leads to an attenuation which is proportional to the square of the frequency. This does not always reflect reality. In, e.g., biological tissues [8], and in marine sediments [9], the frequency dependency of attenuation and dispersion is more complicated. Different forms of the wave equation have been proposed to reflect this complexity [4, 7, 10–12].

Nonlinear effects in sound wave propagation, may also be taken into account during numerical simulation. This is the case for the Bergen Code [13, 14], the KZKTexas code [15–17], and the angular spectrum method defined by Christopher and Parker [18, 19]. In the case of the angular spectrum approach, the attenuation is modeled as proportional to ω^y, with ω the angular frequency and y non-integer, allowing one to simulate attenuation in media like biological tissue. Time domain simulators can use multiple relaxation processes to approximate such attenuation both in the linear case [20] and the nonlinear case [21]. Typically, this requires two or more relaxation processes to model a power law over a restricted frequency range. Each process requires two parameters to be found from a curve fit. These parameters describe the pysics in the case of propagation in sea water or air. In more complex media, the link to the physics is not so direct.

Several simulators take a modified nonlinear wave equation as a starting point by replacing the traditional loss operator by fractional derivatives [7,22,23], or a convolution in time [24–26]. Their justification for modifying the standard wave equations is the ability of fractional derivatives to lead to a dispersion equation that better describes attenuation and dispersion. A wave equation based on fractional constitutive equations gives an alternative to modeling absorption and dispersion in complex media like biological tissues.

In this article, we aim at finding the source of the fractional derivative in the nonlinear wave equation. We derive a nonlinear wave equation using constitutive equations as a starting point. The aim of the article is to relate non-integer power absorption laws to more fundamental physical phenomena, rather than just the measured absorption characteristics. It also establishes a connection between fractional constitutive equations coming from different fields of physics describing mechanical stress or heat transfer. The constitutive equations come from the fractional Kelvin-Voigt model from solid mechanics [27, 28], and a fractional extension of the Gurtin Pipkin model from heat conduction [29, 30], while the other building equations come from fluid mechanics [31, 32].

We start by briefly recalling the definition and properties of the fractional derivative. Then, we derive a modified version of Euler's equation, and of the entropy equation, introducing fractional derivatives. We explain what these modifications are based on, using solid mechanics and heat diffusion theory. Combining these two equations, we get a wave equation by following the steps and approximations done in fluid mechanics theory. Thereafter, we show that the obtained wave equation is a generalization of the Westervelt equation, and that the dispersion equation can describe attenuation and dispersion for propagation in complex media such as biological tissues.

Finally, generalized forms of the Khokhlov-Zabolotskaya-Kuznetsov (KZK) and Burgers' equations using fractional derivatives are obtained.

II. Fractional derivative

The fractional derivative is an extension to integer order derivatives, and is best understood by looking at its Fourier transform in the frequency domain. For any positive integer n, the temporal Fourier transform of the nth order derivative of a function $f(t)$ satisfies the relation

$$\mathcal{F}\left\{\frac{d^n f}{dt^n}, \omega\right\} = (j\omega)^n \mathcal{F}\{f\}. \tag{1}$$

The fractional derivative of order γ, for γ real, can be seen as the operator whose Fourier transform satisfies Eq. (1), where n is replaced by γ. In the time domain, this corresponds to a convolution

$$\frac{d^\gamma f}{dt^\gamma} = \frac{1}{\Gamma(1-r)} \int_0^t \frac{1}{(t-\tau)^r} \frac{d^n}{dt^n} f(\tau) d\tau, \tag{2}$$

where $0 \leq n-1 < \gamma < n$, $r = \gamma - n + 1$, and $\Gamma(1-r)$ is the gamma function. Equation (2) is the definition of the fractional derivative given by Caputo [33, 34]. Fractional derivatives introduce a memory effect in the physical process they describe [28, 35]. The nth order derivative is convolved with a memory function

$$\frac{1}{\Gamma(1-r)} \frac{1}{t^r} \tag{3}$$

In the case where $r \to 1$ (no memory), the memory function tends towards a Dirac impulse function, and the order of the fractional derivative tends towards the integer n. In the case where $r \to 0$ (infinite memory), Eq. (2) tends towards an integration of the nth order derivative resulting in the $(n-1)$th order derivative.

Subsequently, the fractional integral of order α can also be defined as [34]

$$I^\alpha[f(t)] = \frac{1}{\Gamma(\alpha)} \int_0^t (t-\tau)^{(\alpha-1)} f(\tau) d\tau \quad \text{for} \quad 0 < \alpha. \tag{4}$$

Its Fourier transform satisfies the relation

$$\mathcal{F}\{I^\alpha[f(t)], \omega\} = (j\omega)^{-\alpha} \mathcal{F}\{f\}. \tag{5}$$

Hence fractional integrals and derivatives allow to model any power law in the frequency domain. Fractional integrals and derivatives can be combined, giving the property

$$\frac{d^\gamma}{dt^\gamma}[I^\alpha] = \begin{cases} \frac{d^{\gamma-\alpha}}{dt^{\gamma-\alpha}} & \text{if} \quad 0 < \alpha < \gamma \\ I^{\alpha-\gamma} & \text{if} \quad 0 < \gamma < \alpha \end{cases} \tag{6}$$

Fractional derivatives have been introduced in solid mechanics to more appropriately describe the stress-strain relations [28], or heat transfers [1] in viscoelastic media. This will be used here as

a starting point to modify the constitutive equations.

III. From fractional constitutive equations to fractional Euler's and entropy equations

The basic equations that the nonlinear wave equation derived in this paper is built upon are: the equation of continuity, expressing the conservation of mass; the equation of state, expressing the thermodynamic state of the fluid; Euler's equation, that translates the conservation of momentum; and the entropy equation, expressing the conversion of energy in an irreversible process. The last two equations, Euler's equation, and the entropy equation, are the equations that we will modify by introducing fractional derivatives.

A. Euler's equation

In this section, we describe how the expression of the stress tensor can be described by the fractional Kelvin-Voigt model, and how this leads to a form of Euler's equation with fractional derivatives. Following the expression of Euler's equation in Eq. (15.5) of Landau and Lifshitz [31], we have

$$\rho\left(\frac{\partial v_i}{\partial t}+v_k\frac{\partial v_i}{\partial x_k}\right)=\frac{\partial \sigma_{ik}}{\partial x_k}=-\frac{\partial p}{\partial x_i}+\frac{\partial \sigma'_{ik}}{\partial x_k} \tag{7}$$

where ρ is the density, v_i the components of the particle speed vector, t and x_i the temporal and spatial coordinates, and p the total pressure. σ_{ik}, and σ'_{ik} represent the stress tensor, and viscous stress tensor, respectively. Using Eqs. (15.2) and (15.3) of Ref. [31],

$$\begin{aligned}\sigma_{ik}&=-p\delta_{ik}+\sigma'_{ik} \\ &=-p\delta_{ik}+\eta\left(\frac{\partial v_i}{\partial x_k}+\frac{\partial v_k}{\partial x_i}-\frac{2}{3}\delta_{ik}\frac{\partial v_l}{\partial x_l}\right)+\zeta\delta_{ik}\frac{\partial v_l}{\partial x_l},\end{aligned} \tag{8}$$

where η, and ζ are the shear and bulk viscosity coefficients respectively, and are independent of velocity. This is the same relation established by Markham *et al.* [27] in their Eq. (13.3). In their article, they refer to the physical model as Stokes's model. Further on, approximating the static total pressure by the inviscid total pressure, they get the relation

$$p\approx K\frac{\rho_e}{\rho_o}, \tag{9}$$

where K is the Young's modulus, ρ_e the excess density, and ρ_0 the equilibrium density. And finally, they get Eq. (14.2):

$$\sigma_{ik}=-K\frac{\rho_e}{\rho_0}\delta_{ik}+\eta\left(\frac{\partial v_i}{\partial x_k}+\frac{\partial v_k}{\partial x_i}-\frac{2}{3}\delta_{ik}\frac{\partial v_l}{\partial x_l}\right)+\zeta\delta_{ik}\frac{\partial v_l}{\partial x_l}. \tag{10}$$

Using a linear form of the equation of continuity (a full nonlinear form is presented in Sec. IV)

$$\frac{\partial \rho_e}{\partial t} = -\rho_0 \frac{\partial v_i}{\partial x_i}, \tag{11}$$

we get the constitutive equation

$$\sigma_{ik} = K\delta_{ik}\frac{\partial u_i}{\partial x_k} + \eta\left(\frac{\partial v_i}{\partial x_k} + \frac{\partial v_k}{\partial x_i} - \frac{2}{3}\delta_{ik}\frac{\partial v_l}{\partial x_l}\right) + \zeta\delta_{ik}\frac{\partial v_l}{\partial x_l} \tag{12}$$

where u_i are the components of the displacement vector field, and $v_i = \partial u_i/\partial t$.
Comparing this relation to the Kelvin-Voigt model [11, 28] (or Stokes's model as referred to by Markham *et al.* [27]) described by the stress-strain relation

$$\sigma = K\left[\epsilon + \tau_\sigma \frac{\partial \epsilon}{\partial t}\right] \tag{13}$$

where $\epsilon = \partial u/\partial x$ is the strain, u the displacement, and τ_σ the creep time, we can match the component of the normal stress tensor: $-p\delta_{ik} = K\epsilon$, and of the viscous stress tensor: $\sigma'_{ik} = K\tau_\sigma \partial\epsilon/\partial t$.

The theory presented by Markham *et al.* [27] is remarkable in that it relates Eq. (8) to Eq. (13) via Eq. (12), bridging the gap between the stress-strain formulations used in fluid mechanics, and solid mechanics. The equivalence of both formulations for the stress-strain relation is not often found in the literature.

The Kelvin-Voigt model is one of many stress-strain relations. Other models such as Maxwell's model, and the standard linear solid model, also called Zener model, are often employed, each describing the material properties differently. A thorough review of those models was given by Rossikhin and Shitikova [28], where they also discuss a generalization of each model using fractional derivatives. The Kelvin-Voigt model may be generalized using fractional derivatives [11, 28]:

$$\sigma = K\left[\epsilon + \tau_\sigma^\gamma \frac{\partial^\gamma \epsilon}{\partial t^\gamma}\right] \quad \text{for} \quad 0 < \gamma \leq 1, \tag{14}$$

where $\partial^\gamma/\partial t^\gamma$ describes the fractional time-derivative of order γ as defined in Eq. (2). Since the strain rate is $\partial\epsilon/\partial t = \partial v/\partial x$, when considering a one-dimensional deformation, Eq. (14) becomes

$$\begin{aligned} \sigma &= K\left[\epsilon + \tau_\sigma^\gamma I^{1-\gamma}\left(\frac{\partial v}{\partial x}\right)\right] \quad \text{for} \quad 0 < \gamma < 1, \\ &= K\left[\epsilon + \tau_\sigma \frac{\partial v}{\partial x}\right] \quad \text{for} \quad \gamma = 1, \end{aligned} \tag{15}$$

where $I^{1-\gamma}$ is the fractional integral of order $1-\gamma$ as defined in Eq. (4). Introducing the fractional integral in Eq. (7), Euler's equation can be generalized to

$$\rho\left(\frac{\partial v_i}{\partial t} + v_k\frac{\partial v_i}{\partial x_k}\right) = -\frac{\partial p}{\partial x_i} + \tau^{\gamma-1} I^{1-\gamma}\left(\frac{\partial \sigma'_{ik}}{\partial x_k}\right) \tag{16}$$

where τ is a time constant characteristic of the creep time. Replacing σ'_{ik} by its expression using Eq. (8) , and assuming the viscosity coefficients η, and ζ to be constant, Eq. (16) may, in vector notation, be written as

$$\rho\left[\frac{\partial \mathbf{v}}{\partial t} + (\mathbf{v}\cdot\boldsymbol{\nabla})\mathbf{v}\right] = -\boldsymbol{\nabla}p + \tau^{\gamma-1}\eta I^{1-\gamma}(\Delta\mathbf{v}) + \tau^{\gamma-1}(\zeta + \frac{1}{3}\eta)I^{1-\gamma}[\boldsymbol{\nabla}(\boldsymbol{\nabla}\cdot\mathbf{v})], \qquad (17)$$

which is a fractional integral generalization of Navier-Stokes equation. In this work, bold face symbols designate vectors. Eq. (17) can be simplified the same way as Hamilton and Morfey [32] do in the case of thermoviscous fluids to get Eq. (32) in Ref. [32]. We obtain the fractional Euler's equation

$$\rho_0\frac{\partial \mathbf{v}}{\partial t} = -\boldsymbol{\nabla}p' + (\zeta + \frac{4}{3}\eta)\tau^{\gamma-1}I^{1-\gamma}(\Delta\mathbf{v}) - \frac{\rho_0}{2}\boldsymbol{\nabla}v^2 - \rho'\frac{\partial \mathbf{v}}{\partial t} \qquad (18)$$

where $\rho' = \rho - \rho_0$, and $p' = p - p_0$ represent the dynamic density and pressure, which describe small disturbances relative to the equilibrium values ρ_0 and p_0.

B. The entropy equation

The constitutive equation linking heat flux to temperature gradient has evolved in a similar manner as the stress-strain relation. In 1958, Cattaneo [36] and Vernotte [37] modified the Fourier law to allow for a finite speed of propagation of disturbances. Indeed, as it is well explained in the introductions of Refs. [38] and [39], when very small time scales are considered, or when the materials have "a non-homogeneous inner structure" [38], like biological tissues, the assumption of matter as a continuum fails. The classical descriptions for energy transport (e.g., Fourier law) are no longer applicable. The Cattaneo-Vernotte equation modifies the Fourier law "to account for the time lag between the temperature gradient and the heat flux induced by it" [39]. The modification consists of the addition of the second term on the left-hand side in the following equation:

$$\mathbf{q} + \tau_{cv}\frac{\partial \mathbf{q}}{\partial t} = -\kappa\boldsymbol{\nabla}T, \qquad (19)$$

where $\mathbf{q}$ is the heat flux, T the absolute temperature, κ the thermal conductivity, and τ_{cv} is a relaxation time. In 1968, Gurtin and Pipkin [29] introduced a more general time-non-local relation (of which the Cattaneo-Vernotte equation is a particular case), linking heat flux transfer and temperature gradient

$$\mathbf{q}(t) = \int_0^\infty K(\tau)\boldsymbol{\nabla}T(t-\tau)d\tau. \qquad (20)$$

Assuming that the media is initially at constant temperature, that is $\nabla T(t) = 0$ for $t < 0$, Eq. (20) can be written

$$\mathbf{q}(t) = -\int_0^t K(t-\tau)\boldsymbol{\nabla}T(\tau)d\tau. \qquad (21)$$

This is the model that we adopt for the heat flux in the case of propagation in biological tissues whose structure is non-homogeneous. An extension of the model defined by Gurtin and Pipkin can be written using fractional integral notation [30]. Indeed if the heat flux relaxation function is

defined as

$$K(t-\tau) = \frac{\kappa}{\Gamma(\alpha-1)}(t-\tau)^{\alpha-2} \quad \text{for} \quad 1 < \alpha \leq 2, \tag{22}$$

the heat flux equation can be written

$$\mathbf{q}(t) = -\kappa I^{\alpha-1} \boldsymbol{\nabla} T(t), \tag{23}$$

where $I^{\alpha-1}$ represents the fractional integral of order $\alpha - 1$ as defined in Eq. (4). Eq. (23) is thus the fractional constitutive equation describing the heat flux. Combined with the thermal energy equation

$$\boldsymbol{\nabla} \cdot \mathbf{q}(t) = -\rho c_p \frac{\partial T}{\partial t}, \tag{24}$$

where c_p is the specific heat capacity at constant pressure, it leads to a fractional heat equation which was formulated around the nineties in Refs. [1] and [2]. In one space dimension, it reads

$$\frac{\partial^2 T}{\partial x^2} = \frac{1}{D}\frac{\partial^\alpha T}{\partial t^\alpha} \quad \text{with} \quad D = \frac{\kappa}{\rho c_p} > 0, \tag{25}$$

where D is the thermal diffusivity. In Refs. [1] and [2], Eq. (25) is defined for $0 < \alpha \leq 2$. For $0 < \alpha \leq 1$, it is a fractional diffusion equation and for $1 < \alpha \leq 2$, it is a fractional wave equation. In Ref. [40], Nigmatullin explained how fractional derivatives appeared when describing diffusion in a medium of fractal geometry. In this work, we consider Eq. (25) as a fractional wave equation expressed in three space dimensions:

$$\nabla^2 T = \frac{1}{D}\frac{\partial^\alpha T}{\partial t^\alpha}, \quad \text{with} \quad 1 < \alpha \leq 2. \tag{26}$$

Due to the non-integer integral in Eq. (23), the unit of the thermal conductivity κ is $\mathrm{W{\cdot}s^{1-\alpha}/(Km)}$, and in Eq. (26), the unit of the thermal diffusivity D (Ref. [41]) is $\mathrm{m^2/s^\alpha}$. Equation (26) can then be written as

$$\nabla^2 T = \frac{\tau_{th}^{\alpha-2}}{c_0^2}\frac{\partial^\alpha T}{\partial t^\alpha}, \quad \text{with} \quad 1 < \alpha \leq 2, \tag{27}$$

where τ_{th} is a relaxation time characteristic of the medium [36].

In Eq. (33) of Ref. [32], Hamilton and Morfey use a simplified version of the entropy equation:

$$\rho_0 T_0 \frac{\partial s}{\partial t} = \kappa \nabla^2 T, \tag{28}$$

where T_0 and ρ_0 are the equilibrium temperature and density, respectively, and s the entropy per unit mass. This equation expresses the thermal losses in a thermoviscous fluid as a function of temperature, and is a valid approximation well away from solid boundaries [32]. In combination with Eq. (27) we obtain the fractional entropy equation:

$$\rho_0 T_0 \frac{\partial s}{\partial t} = \frac{\kappa \tau_{th}^{\alpha-2}}{c_0^2}\frac{\partial^\alpha T}{\partial t^\alpha}. \tag{29}$$

IV. Fractional wave equation

In this section, we use the fractional versions of Euler's equation (18) and the entropy equation (29), to obtain a wave equation with fractional derivatives. Following the approximations to the second order [42] of Hamilton and Morfey [32], the fractional Euler's equation (18), can be simplified as follows:

$$\rho_0 \frac{\partial \mathbf{v}}{\partial t} = -\boldsymbol{\nabla} p - \frac{\tau^{\gamma-1}}{\rho_0 c_0^2}(\zeta + \frac{4}{3}\eta)\frac{\partial^\gamma}{\partial t^\gamma}\boldsymbol{\nabla} p - \boldsymbol{\nabla}\mathcal{L}, \tag{30}$$

where $\mathcal{L}$ is the second-order Lagrangian density defined as

$$\mathcal{L} = \frac{1}{2}\rho_0 v^2 - \frac{p^2}{2\rho_0 c_0^2}. \tag{31}$$

The prime notation for p' used in Eq. (18) has been dropped, but p still represents the dynamic pressure from this point on. Approximations to the second order as in Ref. [32], lead to the following form of the continuity equation:

$$\frac{\partial \rho'}{\partial t} + \rho_0 \boldsymbol{\nabla}\cdot\mathbf{v} = \frac{1}{\rho_0 c_0^4}\frac{\partial p^2}{\partial t} + \frac{1}{c_0^2}\frac{\partial \mathcal{L}}{\partial t}. \tag{32}$$

This equation is nonlinear, and will be one of the contributors to the nonlinear term in the final wave equation.

We introduce the equation of state as a Taylor series of $P(\rho, s)$ about the equilibrium state (ρ_0, s_0), where terms of third order are neglected [32]:

$$p = c_0^2\rho' + \frac{c_0^2}{\rho_0}\frac{B}{2A}\rho'^2 + \left(\frac{\partial P}{\partial s}\right)_{\rho,0} s', \tag{33}$$

with B/A the medium parameter of nonlinearity, and $s' = s - s_0$ the dynamic entropy. This equation is also nonlinear and is the other contributor to the nonlinear term of the final wave equation. Introducing $T' = T - T_0$, and integrating Eq. (29) with respect to time gives

$$\rho_0 T_0 s' = \frac{\kappa\tau_{th}^{\alpha-2}}{c_0^2}\frac{\partial^{\alpha-1}T'}{\partial t^{\alpha-1}}, \tag{34}$$

which is used to eliminate s' in favor of T' in Eq. (33). Following the steps described by Hamilton and Morfey (see Ref. [32] for detailed description), we get the following equation:

$$\rho' = \frac{p}{c_0^2} - \frac{1}{\rho_0 c_0^4}\frac{B}{2A}p^2 - \frac{\kappa\tau_{th}^{\alpha-2}}{\rho_0 c_0^4}\left(\frac{1}{c_v} - \frac{1}{c_p}\right)\frac{\partial^{\alpha-1}p}{\partial t^{\alpha-1}}, \tag{35}$$

where c_v and c_p are the heat capacity per unit of mass at constant volume and pressure, respectively. Subtracting the time derivative of Eq. (32) from the divergence of Eq. (30), and using Eq. (35) to

eliminate ρ', we get

$$\begin{aligned}\Box^2 p + \frac{\tau^{\gamma-1}}{\rho_0 c_0^2}\left(\zeta + \frac{4}{3}\eta\right)\frac{\partial^\gamma}{\partial t^\gamma}\nabla^2 p \\ + \frac{\kappa\tau_{th}^{\alpha-2}}{\rho_0 c_0^4}\left(\frac{1}{c_v} - \frac{1}{c_p}\right)\frac{\partial^{\alpha+1} p}{\partial t^{\alpha+1}} = -\frac{\beta}{\rho_0 c_0^4}\frac{\partial^2 p^2}{\partial t^2} - \left(\nabla^2 + \frac{1}{c_0^2}\frac{\partial^2}{\partial t^2}\right)\mathcal{L},\end{aligned} \tag{36}$$

where

$$\Box^2 = \nabla^2 - \frac{1}{c_0^2}\frac{\partial^2}{\partial t^2} \tag{37}$$

is the d'Alembertian operator, and

$$\beta = 1 + \frac{B}{2A} \tag{38}$$

is the medium coefficient of nonlinearity. The expression for β regroups contributions to nonlinear propagation coming both from the equation of state, and the equation of continuity. Discarding the term containing $\mathcal{L}$, we get a fractional wave equation:

$$\Box^2 p + \frac{\tau^{\gamma-1}}{\rho_0 c_0^2}\left(\zeta + \frac{4}{3}\eta\right)\frac{\partial^\gamma}{\partial t^\gamma}\nabla^2 p + \frac{\kappa\tau_{th}^{\alpha-2}}{\rho_0 c_0^4}\left(\frac{1}{c_v} - \frac{1}{c_p}\right)\frac{\partial^{\alpha+1} p}{\partial t^{\alpha+1}} = -\frac{\beta}{\rho_0 c_0^4}\frac{\partial^2 p^2}{\partial t^2}. \tag{39}$$

For clarity, the following notations are introduced:

$$L_v = \frac{\tau^{\gamma-1}}{\rho_0 c_0^2}\left(\zeta + \frac{4}{3}\eta\right) \tag{40}$$

$$L_t = -\frac{\kappa\tau_{th}^{\alpha-2}}{\rho_0 c_0^2}\left(\frac{1}{c_v} - \frac{1}{c_p}\right), \tag{41}$$

$$L_v > L_t.$$

Equation (39) may then be expressed as a fractional form of the Westervelt equation

$$\Box^2 p + L_v\frac{\partial^\gamma}{\partial t^\gamma}\nabla^2 p - \frac{L_t}{c_0^2}\frac{\partial^{\alpha+1} p}{\partial t^{\alpha+1}} = -\frac{\beta}{\rho_0 c_0^4}\frac{\partial^2 p^2}{\partial t^2}, \tag{42}$$

which we will call the fractional Westervelt equation of the first form. The first term on the left hand side of Eq. (42) characterizes diffraction. The second and third terms characterize attenuation coming from the fractional Euler's equation and the fractional entropy equation respectively. The term on the right hand side characterizes nonlinearity, and comes from the continuity equation and the equation of state.

In order to get a fractional form of the Westervelt equation with a non-integer frequency power attenuation law, we note that $\gamma = 1$ and $\alpha = 2$ in Eq. (42) leads to the Westervelt equation (see next section). Thus, in that case, the fractional orders are linked. We generalize this link by setting $\gamma = \alpha - 1 = y - 1$ with $1 < y \leq 2$. The same assumption is implicitly done in the derivation of the fractional forms of the Westervelt and Burgers' equations [22, 26]. This leads to the fractional Westervelt equation of the second form:

$$\Box^2 p + L_v\frac{\partial^{y-1}}{\partial t^{y-1}}\nabla^2 p - \frac{L_t}{c_0^2}\frac{\partial^{y+1} p}{\partial t^{y+1}} = -\frac{\beta}{\rho_0 c_0^4}\frac{\partial^2 p^2}{\partial t^2}. \tag{43}$$

Even if it is difficult to find physical data on material properties to justify this assumption, except for $\gamma = 1$, it is reasonable to assume that γ and α are strongly linked. Indeed, the fractional integrals in the stress-strain relation, or the heat flux equation are both due to internal structures or inhomogeneities in the material. The nature of the media dictates the order of the fractional integrals in both equations. Eq. (43) is the form of the fractional wave equation we use in the rest of the article.

V. Comparison with Westervelt equation

In the case of propagation in classical thermoviscous fluids, the stress tensor is described by Eq. (8). This leads to the non-fractional form of the Euler's equation: Eq. (18), where $\gamma = 1$. The entropy equation has also its non-fractional form when using Fourier law as a constitutive equation. It is obtained by setting $\alpha = 2$ in Eq. (29). Equation (39) then becomes

$$\Box^2 p + \frac{1}{\rho_0 c_0^2}\left(\zeta + \frac{4}{3}\eta\right)\frac{\partial}{\partial t}\nabla^2 p + \frac{\kappa}{\rho_0 c_0^4}\left(\frac{1}{c_v} - \frac{1}{c_p}\right)\frac{\partial^3 p}{\partial t^3} = -\frac{\beta}{\rho_0 c_0^4}\frac{\partial^2 p^2}{\partial t^2} \tag{44}$$

The low-frequency regime covers the applications involving compressional waves, while the high-frequency regime applies mostly to shear waves [11]. This article is mainly oriented towards applications of compressional waves, and low frequencies. In this regime, $\nabla^2 p$ can be approximated by $c_0^{-2}\partial^2 p/\partial t^2$. Equation (44) then gives the Westervelt equation

$$\Box^2 p + \frac{\delta}{c_0^4}\frac{\partial^3 p}{\partial t^3} = -\frac{\beta}{\rho_0 c_0^4}\frac{\partial^2 p^2}{\partial t^2}, \tag{45}$$

where

$$\delta = \frac{1}{\rho_0}\left(\zeta + \frac{4}{3}\eta\right) + \frac{\kappa}{\rho_0}\left(\frac{1}{c_v} - \frac{1}{c_p}\right) \tag{46}$$

is the diffusivity of sound. This shows that Eqs. (39), (42), and (43) are fractional generalizations of the Westervelt equation.

VI. Dispersion equation

To find the frequency dependence of attenuation and propagation velocity, a dispersion equation can be derived from Eq. (43). Using the principle of superposition the Fourier transform in space and time of a harmonic plane wave solution, $v(x,t) = \exp[j(\omega t - kx)]$, gives the dispersion equation for any wave. Since the principle of superposition assumes linearity, the nonlinear term has to be excluded in Eq. (43). Using the Fourier transform's property of fractional derivatives given in Eq. (1), we get

$$k = \frac{\omega}{c_0}\sqrt{\frac{1 + L_t e^{j(y-1)\pi/2}\omega^{y-1}}{1 + L_v e^{j(y-1)\pi/2}\omega^{y-1}}} = \frac{\omega}{c(\omega)} - j\alpha(\omega). \tag{47}$$

Simplifications in the low frequency regime give the following expressions [11]:

$$\begin{aligned} \alpha(\omega) &= \frac{1}{c_0}\left(\frac{L_t}{2} - \frac{L_v}{2}\right)\cos\left(\frac{y\pi}{2}\right)|\omega|^y, \\ c(\omega) &\approx c_0\left[1 - \left(\frac{L_t}{2} - \frac{L_v}{2}\right)\sin\left(\frac{y\pi}{2}\right)\omega^{y-1}\right], \end{aligned} \tag{48}$$

These expressions lead to a velocity dispersion relation that satisfies the Kramers-Kronig relation [43], and confirm that it fulfils the causality requirement. The expressions for $\alpha(\omega)$ and $c(\omega)$ describe observations in biological tissues [8] that the Westervelt equation fails to explain. For values of y between 1 and 2, the attenuation is proportional to ω^y, which covers the vast majority of attenuation laws for propagation in biological tissues [8]. For illustration, the frequency dependency for the attenuation, and the velocity dispersion are shown on Figs. 1, and 2 respectively, for different values of y. There is a singularity for y = 1 as discussed in Ref. [11] that is why values for y in the range 1.1 to 2 are plotted . In these examples, the time constants involved in L_v and L_t have been chosen identical. The following values were set for the plots: $\tau = 10^{-10}$ s, c_0 = 1500 m/s, $\alpha = 1.2$ dB/cm at 1 MHz for y = 1.1, and $\omega \leq 3.10^7$ rad/s . The figures show the low-frequency regime, that is $\omega\tau \ll 1$. Figs. 1 and 2 show attenuation and phase velocity dispersion for y = 1.1 that is comparable to the measurements made by Kremkau et al [44] on human brains and to previous illustrations of attenuation and dispersion frequency dependencies [12, 23, 45].

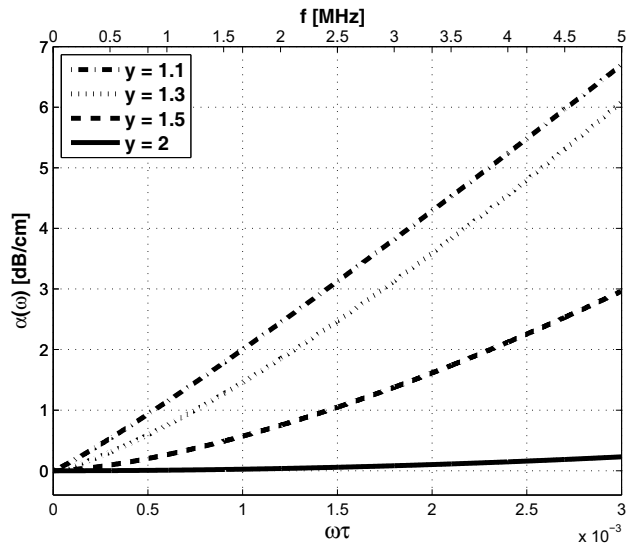

Fig. 1*: Attenuation $\alpha(\omega)$ as a function of $\omega\tau$ for different values of y*

VII. Generalized KZK and Burgers' equations

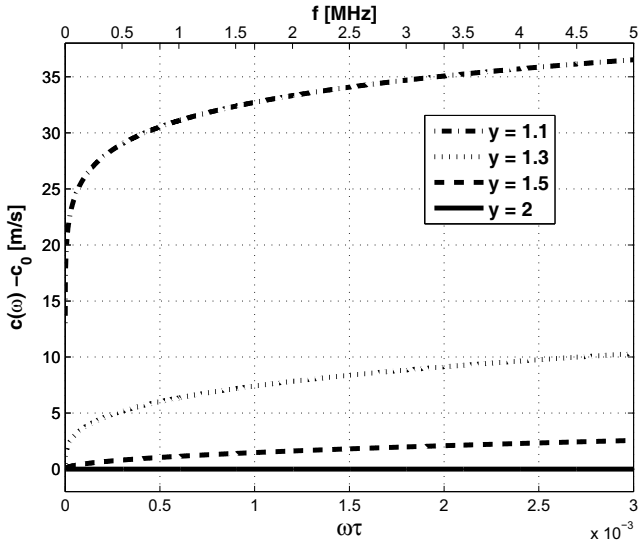

Fig. 2*: Velocity dispersion $c(\omega) - c_0$ as a function of $\omega\tau$ for different values of y*

A. KZK equation

Again, starting from Eq. (43), when approximating $\nabla^2 p$ by $c_0^{-2}\partial^2 p/\partial t^2$ in the low-frequency domain, we get

$$\Box^2 p + \frac{L_v - L_t}{c_0^2}\frac{\partial^{y+1} p}{\partial t^{y+1}} = -\frac{\beta}{\rho_0 c_0^4}\frac{\partial^2 p^2}{\partial t^2}. \tag{49}$$

Introducing the retarded time coordinate $\tau_r = t - z/c_0$, and following the same steps as Hamilton and Morfey in Ref. [32], Eq. (49) can be approximated to

$$\nabla_\perp^2 p - \frac{2}{c_0}\frac{\partial^2 p}{\partial z \partial \tau_r} + \frac{L_v - L_t}{c_0^2}\frac{\partial^{y+1} p}{\partial \tau_r^{y+1}} = -\frac{\beta}{\rho_0 c_0^4}\frac{\partial^2 p^2}{\partial \tau_r^2}, \tag{50}$$

where $\nabla_\perp^2 = \partial^2/\partial x^2 + \partial^2/\partial y^2$ is the Laplacian that operates in the plane perpendicular to the axis of the beam. This approximation is valid for well collimated sound beams satisfying the relation $ka \gg 1$ where k is the wave number, and a the characteristic radius of the source. Eq. (50) is a fractional derivative generalization of the KZK (Khokhlov-Zabolotskaya-Kuznetsov) equation. For $y = 2$, $\delta = c_0^2(L_v - L_t)$, and we obtain the KZK equation

$$\frac{\partial^2 p}{\partial z \partial \tau_r} - \frac{c_0}{2}\nabla_\perp^2 p - \frac{\delta}{2c_0^3}\frac{\partial^3 p}{\partial \tau_r^3} = \frac{\beta}{2\rho_0 c_0^3}\frac{\partial^2 p^2}{\partial \tau_r^2}. \tag{51}$$

B. Burgers' equation

Likewise, re-writing Eq. (49) in one spatial dimension, we get

$$\left(\frac{\partial^2}{\partial z^2} - \frac{1}{c_0^2}\frac{\partial^2}{\partial t^2}\right) p + \frac{L_v - L_t}{c_0^2}\frac{\partial^{y+1} p}{\partial t^{y+1}} = -\frac{\beta}{\rho_0 c_0^4}\frac{\partial^2 p^2}{\partial t^2}. \tag{52}$$

Introducing the retarded time coordinate τ_r, it becomes

$$\frac{\partial^2 p}{\partial z^2} - \frac{2}{c_0}\frac{\partial^2 p}{\partial z \partial \tau_r} + \frac{L_v - L_t}{c_0^2}\frac{\partial^{y+1} p}{\partial \tau_r^{y+1}} = -\frac{\beta}{\rho_0 c_0^4}\frac{\partial^2 p^2}{\partial \tau_r^2}. \tag{53}$$

The first term on the left can be neglected when using second-order approximations as done by Hamilton and Morfey in [32]. An integration with respect to τ_r gives

$$\frac{\partial p}{\partial z} - \frac{L_v - L_t}{2c_0}\frac{\partial^y p}{\partial \tau_r^y} = \frac{\beta}{2\rho_0 c_0^3}\frac{\partial p^2}{\partial \tau_r} = \frac{\beta p}{\rho_0 c_0^3}\frac{\partial p}{\partial \tau_r}. \tag{54}$$

Equation (54) is a fractional derivative generalization of the Burgers' equation. For $y = 2$, we obtain the Burgers' equation

$$\frac{\partial p}{\partial z} - \frac{\delta}{2c_0^3}\frac{\partial^2 p}{\partial \tau_r^2} = \frac{\beta p}{\rho_0 c_0^3}\frac{\partial p}{\partial \tau_r}. \tag{55}$$

VIII. Conclusion

Fractional derivatives are introduced in the constitutive equations by use of previous studies on stress-strain relations in solid mechanics, and heat conduction mechanisms linking to different areas of physics. The nonlinear wave equation obtained from these building equations leads to a frequency-dependent attenuation and dispersion that fit observations [8, 44]. This work justifies why the modifications of the wave equation using fractional derivative, as done in the existing literature, are legitimate. These modifications have been done empirically in view of the observed attenuation or dispersion power laws. Such modifications do not always guarantee the causality of the solution. Since our fractional wave equation is derived from constitutive equations, its causality is assured.

We have shown that the Westervelt equation is a particular case of our wave equation, which may be simplified into a fractional KZK equation. Therefore, fractional derivatives offer an alternative to multiple relaxations used for time-domain simulators like the KZKTexas code [15] to approximate attenuation and dispersion in biological tissue. The fractional derivative can for instance be solved in the time domain by using a backward difference power series [10] or the Grünwald-Letnikov formulation [23]. Using the constitutive equations as a starting point, instead of an approximated wave equation could also be an alternative to simulate sound propagation in non-homogeneous media.

The fractional wave equation introduced requires 9 constants to describe attenuation and dispersion: 2 for the relaxation times, 2 for the order of the fractional derivatives, 2 for the viscosities,

2 for the heat capacities, and 1 for the thermal conductivity. A model using 2 relaxation processes requires 5 constants [21]: 2 for the relaxation frequencies, 2 for the relaxation dispersion, and 1 for the thermoviscous prefactor. However, the thermoviscous prefactor can be expressed using the diffusivity of sound which is a combination of 5 constants: 2 for the viscosities, 2 for the heat capacities, and 1 for the thermal conductivity, bringing the total number of constants to 9. The complexity of a model using fractional equations should therefore not exceeed the complexity of existing models based on multiple relaxation processes.

This article also calls for a better determination of the time constants involved in the fractional loss operators, and maybe measurements establishing a link between the order of the fractional integrals in the stress-strain relation and the heat flux equation. This, in turn, would lead to a better understanding of the attenuation and dispersion mechanisms that happen in hybrid media, like biological tissues, which fall between solids and fluids.

Bibliography

[1] F. Mainardi, "The fundamental solutions for the fractional diffusion-wave equation," *Appl. Math. Lett.*, vol. 9, no. 6, pp. 23–28, 1996.

[2] W. R. Schneider and W. Wyss, "Fractional diffusion and wave equations," *J. Math. Phys.*, vol. 30, pp. 134–144, 1989.

[3] C. G. Koh and J. M. Kelly, "Application of fractional derivatives to seismic analysis of base-isolated models," *Earthquake Eng. Struct. Dyn.*, vol. 19, no. 2, pp. 229–241, 1990.

[4] T. L. Szabo, "Time domain wave equations for lossy media obeying a frequency power law," *J. Acoust. Soc. Am.*, vol. 96, pp. 491–500, 1994.

[5] M. J. Buckingham, "Theory of acoustic attenuation, dispersion, and pulse propagation in unconsolidated granular materials including marine sediments," *J. Acoust. Soc. Am.*, vol. 102, pp. 2579–2596, 1997.

[6] G. V. Norton and J. C. Novarini, "Including dispersion and attenuation directly in the time domain for wave propagation in isotropic media," *J. Acoust. Soc. Am.*, vol. 113, pp. 3024–3030, 2003.

[7] W. Chen and S. Holm, "Fractional Laplacian time-space models for linear and nonlinear lossy media exhibiting arbitrary frequency power-law dependency," *J. Acoust. Soc. Am.*, vol. 115, no. 4, pp. 1424–1430, 2004.

[8] F. A. Duck, "Acoustic properties of tissue at ultrasonic frequencies," in *Physical properties of tissues - A comprehensive reference book*. San Diego, CA: Academic Press, 1990, ch. 4, pp. 98–108.

[9] A. C. Kibblewhite, "Attenuation of sound in marine sediments: A review with emphasis on new low-frequency data," *J. Acoust. Soc. Am.*, vol. 86, pp. 716–738, 1989.

[10] M. G. Wismer, "Finite element analysis of broadband acoustic pulses through inhomogenous media with power law attenuation," *J. Acoust. Soc. Am.*, vol. 120, pp. 3493–3502, 2006.

[11] S. Holm and R. Sinkus, "A unifying fractional wave equation for compressional and shear waves," *J. Acoust. Soc. Am.*, vol. 127, pp. 542–548, 2010.

[12] B. E. Treeby and B. T. Cox, "Modeling power law absorption and dispersion for acoustic propagation using the fractional Laplacian," *J. Acoust. Soc. Am.*, vol. 127, pp. 2741–2748, 2010.

[13] J. Berntsen, "On the use of the Bergen code," http://folk.uib.no/nmajb/Bergencode.html, date last viewed Aug 16, 2010, Mar. 2000.

[14] ——, "Numerical calculations of finite amplitude sound beams," *Frontiers of Nonlinear Acoustics: Proceedings of the 12th ISNA, edited by MF Hamilton and DT Blackstock (Elsevier Science, New York)*, pp. 191–196, 1990.

[15] Y. S. Lee, R. Cleveland, and M. F. Hamilton, "KZKTexas," http://people.bu.edu/robinc/kzk/, date last viewed May 30, 2012, Oct. 1998.

[16] Y. S. Lee and M. F. Hamilton, "Time-domain modeling of pulsed finite-amplitude sound beams," *J. Acoust. Soc. Am.*, vol. 97, pp. 906–917, 1995.

[17] R. J. Zemp, J. Tavakkoli, and R. S. C. Cobbold, "Modeling of nonlinear ultrasound propagation in tissue from array transducers," *J. Acoust. Soc. Am.*, vol. 113, pp. 139–152, 2003.

[18] P. T. Christopher and K. J. Parker, "New approaches to the linear propagation of acoustic fields," *J. Acoust. Soc. Am.*, vol. 90, no. 1, pp. 507–521, Jul. 1991.

[19] ——, "New approaches to nonlinear diffractive field propagation," *J. Acoust. Soc. Am.*, vol. 90, no. 1, pp. 488–499, Jul. 1991.

[20] M. Tabei, T. D. Mast, and R. C. Waag, "Simulation of ultrasonic focus aberration and correction through human tissue," *J. Acoust. Soc. Am.*, vol. 113, no. 2, pp. 1166–1176, 2002.

[21] X. Yang and R. O. Cleveland, "Time domain simulation of nonlinear acoustic beams generated by rectangular pistons with application to harmonic imaging," *J. Acoust. Soc. Am.*, vol. 117, no. 1, pp. 113–123, 2005.

[22] M. Ochmann and S. Makarov, "Representation of the absorption of nonlinear waves by fractional derivatives," *J. Acoust. Soc. Am.*, vol. 94, pp. 3392–3399, 1993.

[23] M. Liebler, S. Ginter, T. Dreyer, and R. E. Riedlinger, "Full wave modeling of therapeutic ultrasound: Efficient time-domain implementation of the frequency power-law attenuation," *J. Acoust. Soc. Am.*, vol. 116, pp. 2742–2750, 2004.

[24] J. Tavakkoli, D. Cathignol, R. Souchon, and O. A. Sapozhnikov, "Modeling of pulsed finite-amplitude focused sound beams in time domain," *J. Acoust. Soc. Am.*, vol. 104, pp. 2061–2072, 1998.

[25] J. P. Remenieras, O. Bou Matar, V. Labat, and F. Patat, "Time-domain modeling of nonlinear distortion of pulsed finite amplitude sound beams," *Ultrasonics*, vol. 38, no. 1–8, pp. 305–311, 2000.

[26] G. V. Norton and R. D. Purrington, "The Westervelt equation with viscous attenuation versus a causal propagation operator: A numerical comparison," *J. Sound Vib.*, vol. 327, no. 1–2, pp. 163–172, 2009.

[27] J. J. Markham, R. T. Beyer, and R. B. Lindsay, "Absorption of sound in fluids," *Rev. Mod. Phys.*, vol. 23, no. 4, pp. 353–411, 1951.

[28] Y. A. Rossikhin and M. V. Shitikova, "Applications of fractional calculus to dynamic problems of linear and nonlinear hereditary mechanics of solids," *Appl. Mech. Rev.*, vol. 50, pp. 15–67, 1997.

[29] M. E. Gurtin and A. C. Pipkin, "A general theory of heat conduction with finite wave speeds," *Arch. Ration. Mech. Anal.*, vol. 31, no. 2, pp. 113–126, 1968.

[30] Y. Z. Povstenko, "Two-dimensional axisymmetric stresses exerted by instantaneous pulses and sources of diffusion in an infinite space in a case of time-fractional diffusion equation," *Int. J. Solids Struct.*, vol. 44, no. 7-8, pp. 2324–2348, 2007.

[31] L. D. Landau and E. M. Lifshitz, "Viscous fluids," in *Fluid Mechanics*, 2nd ed., ser. Course of theoretical physics. Oxford, UK: Pergamon Press, 1987, vol. 6, ch. 2, pp. 44–48.

[32] M. F. Hamilton and C. L. Morfey, "Model equations," in *Nonlinear Acoustics*, M. F. Hamilton and D. T. Blackstock, Eds. San Diego: Academic Press, Dec. 1998, ch. 3, pp. 41–63.

[33] M. Caputo, "Linear models of dissipation whose Q is almost frequency independent-II," *Geophys. J. R. Astron. Soc.*, vol. 13, no. 5, pp. 529–539, 1967.

[34] I. Podlubny, "Fractional derivatives and integrals," in *Fractional Differential Equations*, ser. Mathematics in science and engineering. San Diego, CA: Academic Press, 1999, vol. 198, ch. 2, pp. 41–117.

[35] Y. A. Rossikhin and M. V. Shitikova, "Application of Fractional Calculus for Dynamic Problems of Solid Mechanics: Novel Trends and Recent Results," *Appl. Mech. Rev.*, vol. 63, pp. 1–52, 2010.

[36] C. Cattaneo, "Sur une forme de l'équation de la chaleur éliminant le paradoxe d'une propagation instantanée (A form of heat equation which eliminates the paradox of instantaneous propagation)," *C.R. Acad. Sci.*, vol. 247, pp. 431–433, 1958.

[37] P. Vernotte, "Les paradoxes de la théorie continue de l'équation de la chaleur (Paradoxes in the continuous theory of the heat equation)," *C.R. Acad. Sci.*, vol. 246, no. 22, pp. 3154–3155, 1958.

[38] H. Herwig and K. Beckert, "Experimental evidence about the controversy concerning fourier or non-fourier heat conduction in materials with a nonhomogeneous inner structure," *Heat Mass Transfer*, vol. 36, no. 5, pp. 387–392, 2000.

[39] V. V. Kulish and V. B. Novozhilov, "The relationship between the local temperature and the local heat flux within a one-dimensional semi-infinite domain of heat wave propagation," *Math. Probl. Eng.*, vol. 2003, no. 4, pp. 173–179, 2003.

[40] R. R. Nigmatullin, "The realization of the generalized transfer equation in a medium with fractal geometry," *Phys. Status Solidi B*, vol. 133, no. 1, pp. 425–430, 1986.

[41] O. P. Agrawal, "Solution for a fractional diffusion-wave equation defined in a bounded domain," *Nonlin. Dyn.*, vol. 29, no. 1, pp. 145–155, 2002.

[42] S. I. Aanonsen, T. Barkve, J. Naze Tjøtta, and S. Tjøtta, "Distortion and harmonic generation in the nearfield of a finite amplitude sound beam," *J. Acoust. Soc. Am.*, vol. 75, pp. 749–768, 1984.

[43] K. R. Waters, J. Mobley, and J. G. Miller, "Causality-imposed (Kramers-Kronig) relationships between attenuation and dispersion," *IEEE Trans. Ultrason. Ferroelectr. Freq. Control*, vol. 52, no. 5, pp. 822–823, 2005.

[44] F. W. Kremkau, R. W. Barnes, and C. P. McGraw, "Ultrasonic attenuation and propagation speed in normal human brain," *J. Acoust. Soc. Am.*, vol. 70, pp. 29–37, 1981.

[45] M. O'Donnell, E. T. Jaynes, and J. G. Miller, "Kramers-Kronig relationship between ultrasonic attenuation and phase velocity," *J. Acoust. Soc. Am.*, vol. 69, pp. 696–701, 1981.

Paper IV

A more fundamental approach to the derivation of nonlinear acoustic wave equations with fractional loss operators

F. Prieur, G. Vilenskiy , and S. Holm

Journal of the Acoustical Society of America, Revised version submitted June 15, 2012.

A more fundamental approach to the derivation of nonlinear acoustic wave equations with fractional loss operators

F. Prieur, G. Vilenskiy, and S. Holm

Abstract— A corrected derivation of nonlinear wave propagation equations with fractional loss operators is presented. The fundamental approach is based on fractional formulations of the stress-strain and heat flux definitions but uses the energy equation and thermodynamic identities to link density and pressure instead of an erroneous fractional form of the entropy equation as done in "Nonlinear acoustic wave equations with fractional loss operators" [J. Acoust. Soc. Am. 130(3), 1125-1132 (2011)]. The loss operator of the obtained nonlinear wave equations differs from the previous derivations as well as the dispersion equation, but when approximating for low frequencies the expressions for the frequency dependent attenuation and velocity dispersion remain unchanged.

I. Introduction

Fractional derivatives introduced in physical models can describe sound attenuation in complex media. When introduced into the constitutive equations, they build a wave equation in which attenuation obeys a frequency power law [1] characteristic of many media [2]. Fractional derivatives have also been shown to be closely related to the multiple relaxation model of Nachman *et al.* [3,4].

This paper builds on an article from Prieur and Holm [5] that derives nonlinear wave equations with fractional loss operators and presents a corrected derivation. More precisely, it uses the same fractional models for the stress-strain relation and the heat flux definition, but instead of establishing a fractional form of the entropy equation, it uses the energy equation together with the appropriate generic thermodynamic identities to express the density as a function of pressure using fractional derivatives.

The reason why we prefer this alternative approach is as follows. In media where the stress tensor and heat flux are described by the fractional Kelvin-Voigt model and the fractional Fourier's law, respectively, using the conventional entropy equation may result in a negative entropy production rate. This situation is different from that of the classical Navier-Stokes and Fourier equations, where the use of the conventional Gibbs definition of the entropy results in a positive entropy production rate. Consequently, in general the conventional local equilibrium hypothesis which is used for Newtonian fluids does not work here, and an extension of the conventional irreversible thermodynamics approach is required. Although non-equilibrium thermodynamics is a vibrant and rapidly expanding field of research [6], to the authors' knowledge, there exists no such extended thermodynamic model for the above mentioned fractional constitutive equations in the literature. Derivation of fractional wave equations directly from the equations of mass, momentum and energy conservation alleviates the indeterminacy of the entropy equation, to a certain extent.

This more physically straightforward approach leads to a different form for the fractional loss operator and for the dispersion relation than in Ref. [5] because it does not employ the incorrect version of the fractional entropy equation postulated in Eq. (29) of Ref. [5]. The expressions for the attenuation and velocity dispersion, however, remain the same in the low frequency approximation.

In the first part of this article, we recall the fractional constitutive equations. We then derive an expression of the density as a function of pressure using fractional derivatives and explain why it is more rigorous than the approach used in Ref. [5]. Finally, the corrected form of the nonlinear wave equations with fractional loss operators are presented.

II. Fractional constitutive equations

The approach in the paper of Prieur and Holm [5], which introduces fractional loss operators in nonlinear wave equations, is based on the fractional version of two constitutive equations. The first equation describes the relation between stress and the corresponding strain. It is a generalization of the Kelvin-Voigt model:

$$\sigma = K\left[\epsilon + \tau_\sigma^\gamma \frac{\partial^\gamma \epsilon}{\partial t^\gamma}\right] \quad \text{for} \quad 0 < \gamma \leq 1, \tag{1}$$

where σ is the stress, K is the Young's modulus, ϵ is the strain, and τ_σ is the creep time. It is valid for low and intermediate frequencies [1]. Here $\partial^\gamma/\partial t^\gamma$ describes the fractional time-derivative of order γ. The Caputo fractional derivative of order γ of a function f is defined by [7]

$$\frac{d^\gamma f}{dt^\gamma} = \frac{1}{\Gamma(1-r)} \int_0^t \frac{1}{(t-\tau)^r} \frac{d^n}{dt^n} f(\tau) d\tau, \tag{2}$$

where n is an integer, $0 \leq n-1 < \gamma < n$, $r = \gamma - n + 1$, and $\Gamma(1-r)$ is the gamma function. The second constitutive equation defines the heat flux and is a generalization of the Gurtin-Pipkin model. It is written as

$$\mathbf{q}(t) = -\tau_{th}^{1-\alpha} \kappa I^{\alpha-1} \boldsymbol{\nabla} T(t) \quad \text{for} \quad 1 < \alpha \leq 2, \tag{3}$$

where $\mathbf{q}$ is the heat flux, T the absolute temperature, κ is the thermal conductivity, $I^{\alpha-1}$ represents the fractional integral of order $\alpha - 1$ and τ_{th} is a thermal relaxation time characteristic of the medium. The fractional integral of order α of a function f is defined by [7]

$$I^\alpha[f(t)] = \frac{1}{\Gamma(\alpha)} \int_0^t (t-\tau)^{(\alpha-1)} f(\tau) d\tau \quad \text{for} \quad 0 < \alpha. \tag{4}$$

The first constitutive equation, Eq. (1) leads to a fractional form of the momentum equation [5]:

$$\rho_0 \frac{\partial \mathbf{v}}{\partial t} = -\boldsymbol{\nabla} p' + (\zeta + \frac{4}{3}\eta) \tau^{\gamma-1} I^{1-\gamma} (\nabla^2 \mathbf{v}) - \frac{\rho_0}{2} \boldsymbol{\nabla} v^2 - \rho' \frac{\partial \mathbf{v}}{\partial t}, \tag{5}$$

where $\mathbf{v}$ is the velocity vector, $v = |\mathbf{v}|$, η and ζ are the shear and bulk viscosity coefficients, respectively, $\rho' = \rho - \rho_0$, and $p' = p - p_0$ represent the dynamic density and pressure, which describe small disturbances relative to the equilibrium values ρ_0 and p_0. The second constitutive equation was used in Ref. [5] to get to a fractional form of the entropy equation. In the next sections, we show a more rigorous approach for this step.

III. The problem of the entropy equation

A general form of the entropy equation as it appears in conventional fluid mechanics can be found by combining Eqs. (2.25) and (2.28) from Ref. [8] with the help of Eq. (2.29)

$$\rho T \left(\frac{\partial s}{\partial t} + \mathbf{v} \cdot \boldsymbol{\nabla} s \right) = -\boldsymbol{\nabla} \cdot \mathbf{q} + \Phi, \tag{6}$$

where ρ is the density, s the specific entropy, and Φ represents the work of the dissipative stresses.

For Newtonian fluids Φ is strictly positive and guarantees a positive entropy production rate. However, in the case of a stress tensor defined using fractional derivatives as in Eq. (1), Φ is given

by the following expression

$$\begin{aligned}\Phi &\equiv \tau^{\gamma-1}\sum_{i=1}^{3}\sum_{k=1}^{3}\frac{\partial v_i}{\partial x_k}I^{1-\gamma}\left(\sigma'_{ik}\right)\\ &= \frac{\tau^{\gamma-1}}{\Gamma\left(1-\gamma\right)}\sum_{i=1}^{3}\sum_{k=1}^{3}\frac{\partial v_i\left(t\right)}{\partial x_k}\int_0^t \sigma'_{ik}(\tau)(t-\tau)^{-\gamma}d\tau,\end{aligned} \tag{7}$$

where σ'_{ik} is the viscous stree tensor as defined in Eq. (8) of Ref. [5]. Contrary to the conventional Navier-Stokes hydrodynamics, here Φ is not a positive quadratic form of $\partial v_i/\partial x_k$ as shown in Eq. (2.30) of Ref. [8]. Because of the presence of the integral operator over time, here the expression for Φ can, in principle, be of any sign depending on the current value of t and the previous history of the system's time evolution. Generally speaking, this situation can be resolved by employment of the methods which constitute the subject of extended thermodynamics (see Ref. [6] for an in-depth discussion), where it is shown that an additional entropy production term must be present on the right-hand side of the entropy equation to compensate for the negative Φ and ensure that the rate of entropy production is positive. Detailed discussion of this theoretical approach can be found in monograph [6], and is omitted here both because it goes beyond the scope of this paper and due to its complexity.

In the absence of function Φ (e.g. in a stagnant fluid) the rate of entropy production which corresponds to the term $-\boldsymbol{\nabla}\cdot\mathbf{q}$ may also become negative, implying that the entropy equation requires appropriate correction if the Gurtin-Pipkin model is used instead of the classical Fourier's law. For Cattaneo's law of heat conduction, which is a special case of the Gurtin-Pipkin model, the structure of this corrective term was worked out in Ref. [6]. However, to the best of our knowledge, it still remains unknown for the Gurtin-Pipkin model.

Neglecting Φ, the correcting terms that ensure a positive entropy production rate, and the term in $\mathbf{v}\cdot\boldsymbol{\nabla}s$ we obtain the following version of the fractional entropy equation using Eq. (3)

$$\rho T\frac{\partial s}{\partial t} = -\boldsymbol{\nabla}\cdot\mathbf{q} = \tau_{th}^{1-\alpha}\kappa I^{\alpha-1}\nabla^2 T. \tag{8}$$

This linearized entropy equation differs from Eq. (29) in Ref. [5] by the presence of the Laplacian operator. Since the corrective term in the entropy equation is unknown in the case of a non-Newtonian media, the equation linking the density to the pressure must be found by a different method from what was done in Ref. [5]. It can be shown that Eq. (8) is consistent with the second order accurate fractional wave equation derived by this alternative method.

IV. The fractional thermodynamic equation of state

The chosen alternative way of getting a fractional relation between density and pressure without using the entropy equation has its starting point in the following two thermodynamic identities, the caloric and thermodynamic equations of state, respectively [9]:

$$de = \left(c_p - b\frac{p}{\rho}\right)dT + \left(\frac{p}{\rho^2 c_T^2} - b\frac{T}{\rho}\right)dp, \tag{9}$$

and

$$d(1/\rho) = b\frac{dT}{\rho} - \frac{dp}{\rho^2 c_T^2}, \tag{10}$$

where e is the specific internal energy, c_p is the specific heat capacity at constant pressure, b is the coefficient of thermal expansion, and c_T is the sound speed at constant temperature. Using Eqs. (9) and (10) in the conventional energy equation [9],

$$\rho\left(\frac{de}{dt} + p\frac{d(1/\rho)}{dt}\right) = -\boldsymbol{\nabla}\cdot\mathbf{q} + \Phi, \tag{11}$$

we get

$$\rho\left(c_p\frac{dT}{dt} - b\frac{T}{\rho}\frac{dp}{dt}\right) = -\boldsymbol{\nabla}\cdot\mathbf{q} + \Phi, \tag{12}$$

where Φ corresponds now to the work of dissipative stresses in the case of a fractional stress-strain relation. Replacing the heat flux by its fractional definition, Eq. (3) we get:

$$\rho\left(c_p\frac{dT}{dt} - b\frac{T}{\rho}\frac{dp}{dt}\right) = \tau_{th}^{1-\alpha}\kappa I^{\alpha-1}\nabla^2 T + \Phi. \tag{13}$$

Using Eq. (13) and the thermodynamic identities [9]

$$\frac{b^2 T}{c_p - c_v} = \frac{1}{c_T^2} \quad \text{and} \quad \frac{c_s^2}{c_T^2} = \frac{c_p}{c_v}, \tag{14}$$

where c_v is the specific heat capacity at constant volume, and c_s is the sound speed at constant entropy, the thermodynamic equation of state, Eq. (10), can be re-written

$$\frac{d\rho}{dt} = \frac{1}{c_s^2}\frac{dp}{dt} - \frac{b}{c_p}(\tau_{th}^{1-\alpha}\kappa I^{\alpha-1}\nabla^2 T + \Phi). \tag{15}$$

Assume now, that the viscosities involved in the expression of Φ and the thermal conductivity κ are small and that their contribution is of the same order of magnitude as the amplitude of the sound wave velocity. As Φ is proportional to a viscosity multiplied by the square of a velocity, it is of the third order and can be neglected in both Eqs. (13) and (15). We then obtain from Eq. (13) to the leading order and from Eq. (15) to the second order,

$$\frac{dT}{dt} = \frac{bT}{\rho c_p}\frac{dp}{dt} \quad \text{and} \quad \frac{d\rho}{dt} = \frac{1}{c_s^2}\frac{dp}{dt} - \frac{b}{c_p}\tau_{th}^{1-\alpha}\kappa I^{\alpha-1}\nabla^2 T. \tag{16}$$

Combining those two equations and using the identities in Eq. (14), we get

$$c_s^2\frac{d\rho}{dt} = \frac{dp}{dt} - \left(\frac{1}{c_v} - \frac{1}{c_p}\right)\frac{\tau_{th}^{1-\alpha}\kappa}{\rho} I^{\alpha-1}\nabla^2 p. \tag{17}$$

We then use an expansion of $c_s^2(\rho, T)$ in a power series of the density perturbation ρ' to get to the second order

$$c_s^2(\rho_0, T)\frac{d\rho}{dt} = \frac{dp}{dt} - \frac{\partial c_s^2}{\partial\rho}(\rho_0, T_0)\rho'\frac{d\rho}{dt} - \left(\frac{1}{c_v} - \frac{1}{c_p}\right)\frac{\tau_{th}^{1-\alpha}\kappa}{\rho_0} I^{\alpha-1}\nabla^2 p. \tag{18}$$

In addition, we know from Eq. (15) that to the leading order $d\rho/dt = c_s^{-2}(\rho_0, T)dp/dt$ which after integration gives $\rho' = c_s^{-2}(\rho_0, T_0)p'$, and Eq. (18) becomes

$$\frac{d\rho}{dt} = \frac{1}{c_s^2(\rho_0, T)}\frac{dp}{dt} - \frac{\partial c_s^2}{\partial \rho}(\rho_0, T_0)\frac{p'}{c_s^6(\rho_0, T_0)}\frac{dp}{dt} - \frac{1}{c_s^2(\rho_0, T_0)}\left(\frac{1}{c_v} - \frac{1}{c_p}\right)\frac{\tau_{th}^{1-\alpha}\kappa}{\rho_0} I^{\alpha-1}\nabla^2 p. \quad (19)$$

To keep the second order accuracy, the convective time derivative d/dt must be replaced in Eq. (19) by $(\partial/\partial t + \mathbf{v}\cdot\boldsymbol{\nabla})$ in the term on the left-hand side and the first term on the right hand side but can be substituted by $\partial/\partial t$ in the other terms. Using an expansion of $c_s^{-2}(\rho_0, T)$ in a power series of the temperature perturbation T', to the second order the term in $\mathbf{v}.\boldsymbol{\nabla}\rho$ cancels out with the term in $\mathbf{v}\cdot\boldsymbol{\nabla}p/c_s^2(\rho_0, T_0)$ and we get

$$\frac{\partial \rho}{\partial t} = \frac{1}{c_s^2}\frac{\partial p}{\partial t} - \left(\frac{1}{c_s^4}\frac{\partial c_s^2}{\partial T}T' + \frac{1}{c_s^6}\frac{\partial c_s^2}{\partial \rho}p'\right)\frac{\partial p}{\partial t} - \frac{1}{c_s^2}\left(\frac{1}{c_v} - \frac{1}{c_p}\right)\frac{\tau_{th}^{1-\alpha}\kappa}{\rho_0} I^{\alpha-1}\nabla^2 p, \quad (20)$$

where c_s^2 and its derivatives are all taken in (ρ_0, T_0). Using Eq. (16) to replace T' by $bT_0p'/\rho_0 c_p$ we get

$$\frac{\partial \rho}{\partial t} = \frac{1}{c_s^2}\frac{\partial p}{\partial t} - \frac{1}{c_s^4}\left\{\frac{bT_0}{\rho_0 c_p}\frac{\partial c_s^2}{\partial T} + \frac{1}{c_s^2}\frac{\partial c_s^2}{\partial \rho}\right\}p'\frac{\partial p}{\partial t} - \frac{1}{c_s^2}\left(\frac{1}{c_v} - \frac{1}{c_p}\right)\frac{\tau_{th}^{1-\alpha}\kappa}{\rho_0} I^{\alpha-1}\nabla^2 p. \quad (21)$$

Using the identity of equilibrium thermodynamics [9]

$$ds = -\frac{c_p - c_v}{\rho b T}d\rho + \frac{c_v}{T}dT, \quad (22)$$

together with those in Eq. (14), it can be shown that the constant term in curly brackets in Eq. (21) is equal to $c_s^{-2}(\partial c_s^2/\partial\rho)_s$. Using the following definitions [2]:

$$A \equiv \rho_0 c_s^2 \quad \text{and} \quad B \equiv \rho_0^2\left(\frac{\partial c_s^2}{\partial \rho}\right)_s, \quad (23)$$

an integration in time gives

$$\rho' = \frac{1}{c_s^2}p' - \frac{1}{\rho_0 c_s^4}\frac{B}{2A}p'^2 - \frac{\tau_{th}^{1-\alpha}\kappa}{\rho_0 c_s^2}\left(\frac{1}{c_v} - \frac{1}{c_p}\right) I^{\alpha}\nabla^2 p'. \quad (24)$$

Equation (24) expresses the density as a function of pressure and is the corrected form of Eq. (35) in Ref. [5] where the fractional time derivative is now replaced by a fractional time integral and a Laplacian. The presented derivation does not assume validity of the equation of state for ideal gas in order to establish a relation between pressure and density as done in other works [8, 10, 11].

V. Nonlinear wave equations with fractional loss operators

As mentioned in Ref. [5], the fractional momentum equation can be simplified to

$$\rho_0\frac{\partial \mathbf{v}}{\partial t} = -\boldsymbol{\nabla}p - \frac{\tau^{\gamma-1}}{\rho_0 c_0^2}(\zeta + \frac{4}{3}\eta)\frac{\partial^\gamma}{\partial t^\gamma}\boldsymbol{\nabla}p - \boldsymbol{\nabla}\mathcal{L}, \quad (25)$$

where $\mathcal{L}$ is the second-order Lagrangian density defined as:

$$\mathcal{L} = \frac{1}{2}\rho_0 v^2 - \frac{p^2}{2\rho_0 c_0^2}, \tag{26}$$

and we use the notation of Ref. [5]. A second order approximation of the equation of continuity gives

$$\frac{\partial \rho'}{\partial t} + \rho_0 \boldsymbol{\nabla} \cdot \mathbf{v} = \frac{1}{\rho_0 c_0^4}\frac{\partial p^2}{\partial t} + \frac{1}{c_0^2}\frac{\partial \mathcal{L}}{\partial t}. \tag{27}$$

Subtracting the time derivative of Eq. (27) from the divergence of Eq. (25), and using the new expression for ρ presented in Eq. (24) where $c_s(\rho_0, T)$ is replaced by c_0 we get:

$$\begin{aligned} \Box^2 p &+ \frac{\tau^{\gamma-1}}{\rho_0 c_0^2}\left(\zeta + \frac{4}{3}\eta\right)\frac{\partial^\gamma}{\partial t^\gamma}\nabla^2 p \\ &+ \frac{\kappa \tau_{th}^{1-\alpha}}{\rho_0 c_0^2}\left(\frac{1}{c_v} - \frac{1}{c_p}\right)\frac{\partial^{2-\alpha}}{\partial t^{2-\alpha}}\nabla^2 p \\ &= -\frac{\beta}{\rho_0 c_0^4}\frac{\partial^2 p^2}{\partial t^2} - \left(\nabla^2 + \frac{1}{c_0^2}\frac{\partial^2}{\partial t^2}\right)\mathcal{L}, \end{aligned} \tag{28}$$

where the d'Alembertian operator $\Box^2$ and the medium coefficient of nonlinearity β are defined as in Ref. [5]. After neglecting the term containing $\mathcal{L}$ and defining

$$L_v = \frac{\tau^{\gamma-1}}{\rho_0 c_0^2}\left(\zeta + \frac{4}{3}\eta\right) \quad \text{and} \quad L_t = -\frac{\kappa \tau_{th}^{1-\alpha}}{\rho_0 c_0^2}\left(\frac{1}{c_v} - \frac{1}{c_p}\right), \tag{29}$$

we get a corrected version of the fractional Westervelt equation of the first form

$$\Box^2 p + L_v \frac{\partial^\gamma}{\partial t^\gamma}\nabla^2 p - L_t \frac{\partial^{2-\alpha}}{\partial t^{2-\alpha}}\nabla^2 p = -\frac{\beta}{\rho_0 c_0^4}\frac{\partial^2 p^2}{\partial t^2}. \tag{30}$$

Note that the dependency on the order of the fractional operator α in the heat flux equation, Eq. (3), is now different compared to Ref. [5]. In addition the third term on the left-hand side of Eq. (30) involves both temporal and spatial derivatives while in Ref. [5], it only involved temporal derivatives. By setting $\gamma = 1$ and $\alpha = 1$, we get the correct form of Eq. (44) in Ref. [5]

$$\Box^2 p + \frac{1}{\rho_0 c_0^2}\left(\zeta + \frac{4}{3}\eta\right)\frac{\partial}{\partial t}\nabla^2 p + \frac{\kappa}{\rho_0 c_0^2}\left(\frac{1}{c_v} - \frac{1}{c_p}\right)\frac{\partial}{\partial t}\nabla^2 p = -\frac{\beta}{\rho_0 c_0^4}\frac{\partial^2 p^2}{\partial t^2}, \tag{31}$$

which leads to the Westervelt equation when using the low frequency approximation, and Eqs. (1) and (3) describe the traditional Kelving-Voigt model and the Fourier's law, respectively. Due to the incorrect form of Eq. (42) the value for α leading to the Westervelt equation was erroneously set to 2 in Ref. [5]. We generalize the link between the fractional orders by setting $\gamma = 2 - \alpha = y - 1$ and get the correct version of the Westervelt equation of the second form, Eq. (43) in Ref. [5],

$$\Box^2 p + (L_v - L_t)\frac{\partial^{y-1}}{\partial t^{y-1}}\nabla^2 p = -\frac{\beta}{\rho_0 c_0^4}\frac{\partial^2 p^2}{\partial t^2}. \tag{32}$$

This gives the corrected dispersion relation, Eq. (47) of Ref. [5],

$$k = \frac{\omega}{c_0}\sqrt{\frac{1}{1 + (L_v - L_t)e^{j(y-1)\pi/2}\omega^{y-1}}}, \tag{33}$$

which leads to the unchanged Eq. (48) in the same reference, expressing the frequency dependency of the attenuation and phase velocity.

VI. Conclusion

An updated form for nonlinear wave equations with fractional loss operators has been presented. The derivation is based on constitutive equations describing the stress-strain relation and the relation between the heat flux and the temperature. Instead of establishing a fractional form of the entropy equation from the heat flux definition, the energy equation and conventional thermodynamic identities are used to get an expression of the density as a function of pressure including fractional derivatives. This approach is more general and does not use the approximation of the medium as an ideal gas to link the entropy to the pressure.

This derivation is physically more consistent and gives a corrected form for the fractional loss operators of the nonlinear equations presented previously. The loss operator coming from thermal damping involves both spatial and temporal derivatives while in the previous formulation it only involves temporal derivatives. Although the dispersion equation also differs from the previous derivation, after low frequency approximation the expressions of the frequency dependent attenuation and dispersion remain unchanged.

Bibliography

[1] S. Holm and S. P. Näsholm, "A causal and fractional all-frequency wave equation for lossy media," *J. Acoust. Soc. Am*, vol. 130, no. 4, pp. 2195–2202, Oct. 2011.

[2] F. A. Duck, "Acoustic properties of tissue at ultrasonic frequencies," in *Physical properties of tissues - A comprehensive reference book*. San Diego, CA: Academic Press, 1990, ch. 4, pp. 98–108.

[3] A. I. Nachman, J. F. Smith III, and R. C. Waag, "An equation for acoustic propagation in inhomogeneous media with relaxation losses," *J. Acoust. Soc. Am*, vol. 88, no. 3, pp. 1584–1595, Sep. 1990.

[4] S. P. Näsholm and S. Holm, "Linking multiple relaxation, power-law attenuation, and fractional wave equations," *J. Acoust. Soc. Am*, vol. 130, no. 5, pp. 3038–3045, Nov. 2011.

[5] F. Prieur and S. Holm, "Nonlinear acoustic wave equations with fractional loss operators," *J. Acoust. Soc. Am*, vol. 130, no. 3, pp. 1125–1132, Sep. 2011.

[6] G. Lebon, D. Jou, and J. Casas-Vázquez, *Understanding Non-equilibrium Thermodynamics: Foundations, Applications, Frontiers*. Berlin Heidelberg: Springer-Verlag, 2008, ch. 7, pp. 179–213.

[7] I. Podlubny, "Fractional derivatives and integrals," in *Fractional Differential Equations*, ser. Mathematics in science and engineering. San Diego, CA: Academic Press, 1999, vol. 198, ch. 2, pp. 41–117.

[8] B. O. Enflo and C. M. Hedberg, "Physical theory of nonlinear acoustics," in *Theory of Nonlinear Acoustics in Fluids*, ser. Fluid mechanics and its applications. New York, NY: Kluwer academic publishers, 2002, vol. 67, ch. 2, pp. 13–24.

[9] L. D. Landau and E. M. Lifshitz, "Statistical physics," in *Course of Theoretical Physics*, 3rd ed., E. M. Lifshitz and L. P. Pitaevskii, Eds. Oxford, UK: Pergamon Press, 1980, vol. 5, ch. 2, pp. 51–55.

[10] M. F. Hamilton and C. L. Morfey, "Model equations," in *Nonlinear Acoustics*, M. F. Hamilton and D. T. Blackstock, Eds. San Diego, CA: Academic Press, Dec. 1998, ch. 3, pp. 41–63.

[11] V. P. Kuznetsov, "Equations of nonlinear acoustics," *Sov. Phys. Acoust*, vol. 16, no. 4, pp. 467–470, 1971.

Paper V

Fast simulation of second harmonic ultrasound field using a quasi-linear method

F. Prieur, T. F. Johansen , S. Holm, and H. Torp

Journal of the Acoustical Society of America, , vol. 131, no. 6, pp. 4365-4375, June 2012.

Fast simulation of second harmonic ultrasound field using a quasi-linear method

F. Prieur, T. F. Johansen , S. Holm, and H. Torp

Abstract— Nonlinear propagation of sound has been exploited in the last 15 years in medical ultrasound imaging through tissue harmonic imaging (THI). THI creates an image by filtering the received ultrasound echo around the second harmonic frequency band. This technique produces images of enhanced quality due to reduced body wall reverberation, lower perturbations from off-axis echoes, and multiple scattering of reduced amplitude. In order to optimize the image quality it is essential to be able to predict the amplitude level and spatial distribution of the propagating ultrasound pulse. A method based on the quasi-linear approximation has been developed to quickly provide an estimate of the ultrasound pulse. This method does not need to propagate the pulse stepwise from the source plane to the desired depth, it directly computes a transverse profile at any depth from the definitions of the transducer and the pulse. The computation handles three spatial dimensions which allows for any transducer geometry. A comparison of pulse forms, transverse profiles, as well as axial profiles obtained by this method and state-of-the-art simulators, the KZK-Texas code, and Abersim, shows a satisfactory match. The computation time for the quasi-linear method is also smaller than the time required by the other methods.

I. Introduction

Nonlinear propagation of sound has, for the last 15 years, proved to be crucial for enhancing image quality in medical ultrasound imaging. A consequence of nonlinearity is the appearance of energy around the harmonic frequency bands as the signal propagates. In tissue harmonic imaging (THI), the image reconstruction is made from receiving signals in the second harmonic frequency band. In many clinical applications, THI results in enhanced image quality compared to reconstructing the image from echoes in the transmitted frequency band. THI has been shown to improve endocardial border definition [1, 2] and measurements of heart functions [3]. THI has also shown promising image improvements for, e.g., liver [4] and kidney [5] examination. Duck [6] presents a comprehensive review explaining why THI allows for better image quality.

A number of simulators have been developed to model nonlinear propagation of sound. Christopher and Parker [7, 8] developed a method based on an angular spectrum approach. But simulation of short pulses as the one used in medical ultrasound imaging requires a large number of harmonics rendering the computation time prohibitive. The KZKTexas code [9, 10] does not have this limitation because it solves the propagation in the time domain. However it uses multiple relaxation processes to simulate power law attenuation as in biological tissue. This requires a number of parameters (typically five when using two relaxation processes) increasing the complexity of the method. Both methods use the operator splitting approach and therefore require stepwise propagation from the source to the depth of interest. In this article, the focus is on fast simulators.

The quasi-linear theory has been used previously to attempt a more computational effective solution. Yan and Hamilton [11] recently presented a method based on the quasi-linear assumption that allows one to model body wall aberrations by use of phase screens. The method is presented in the case of continuous wave excitation and can propagate the wave from phase screen to phase screen. In 2011, Du and Jensen [12] published their findings on a possible nonlinear extension to the Field II simulator [13, 14]. They use the quasi-linear theory and consider pulsed excitation. However, they dismiss interactions between the temporal frequency components of the transmitted pulse and propagate each of them individually. This puts a limitation on the pulse bandwidth for which the method is valid. A work worth mentioning, though not exactly based on the quasi-linear theory, is the article from Jing *et al.* [15] where they present an improvement to the classical angular approach methods by finding an implicit solution for the nonlinear term. Though continuous wave is often assumed in their paper, the method includes the case of pulsed excitation. Of special interest is the approximation made to this implicit solution that corresponds to neglecting back propagation. Finally, the work of Varray *et al.* [16] also shows an application of the quasi-linear approximation by finding a solution to the Westervelt equation. They use what they define as the generalized angular spectrum approach to simulate the second harmonic signal in a medium where the nonlinear parameter varies. Unlike in Refs. [11] and [12], they neglect the terms due to back propagation as in Ref. [15]. This method uses stepwise propagation since the medium is inhomogeneous.

In this article, we present a method for nonlinear pulsed wave propagation based on the quasi-linear theory. It does not require stepwise propagation and simulates the pulse in the frequency domain allowing a trivial modeling of attenuation. Some theory of the described method as well

as simulation results were previously presented in conference proceedings papers [17, 18]. This article brings additional explanations on the physics behind the solution and on the implementation details of the simulator. It also compares a new implementation of the solutions with recognized simulators and measurements by establishing lateral and axial pressure profiles. The main advantage of the method is that it allows a fast estimation of the amplitude of the pulse at any depth. The objective of the algorithm is that it should be fast enough to allow a medical scanner to adjust its setup parameters as the user adjusts imaging parameters, without noticeable delay for the user. This is important in all harmonic imaging modes, but in particular those where several transmit focus zones are used to create an image using a montage process [19]. In that case an approximation to dynamically focused transmission is performed by acquiring several sub-images at individual transmission focal points. Each sub-image is only used around its focal point and mounted next to the other sub-images to form a new image with improved transmit focusing. It is imperative that the user does not notice any gain variation across the cuts, thus rendering the montage process invisible. As the user adjusts setup parameters, e.g., for increasing the frame rate by using fewer sub-images, the ultrasound scanner needs to estimate the proper transmit level and receive gain to use as a function of depth. The fast pressure amplitude estimate provided by the presented method is therefore an adapted solution to this problem.

The first part of this article presents theoretical solutions to a nonlinear wave equation using quasi-linearity and their formulations in our simulator. In the second part, we describe the implementation of the simulator and quantify its computational requirements. In the third part, the performance of the simulator are evaluated and compared to well established simulators both in terms of accuracy and speed. In the last part of the article, the limitations of the simulator are discussed and some conclusions are drawn.

II. Theory

A. Wave equation and quasi-linearity

The nonlinear propagation of sound in an absorbing fluid can be described by the following wave equation

$$\nabla^2 p - \frac{1}{c_0^2}\frac{\partial^2 p}{\partial t^2} + \mathcal{L}(p) = -\frac{\beta}{\rho_0 c_0^4}\frac{\partial^2 p^2}{\partial t^2}, \tag{1}$$

where ∇^2 is the Laplacian operator, p, c_0, ρ_0, and β represent the acoustic pressure, the sound speed, the medium density, and the coefficient of nonlinearity, respectively. The first two terms on the left-hand side of Eq. (1) represent the diffraction. The linear operator $\mathcal{L}(p)$ represents the losses. In the case where $\mathcal{L}(p) = \frac{\delta}{c_0^4}\frac{\partial^3 p}{\partial t^3}$, with δ the diffusivity of sound, Eq. (1) is the Westervelt equation [20] and the loss operator describes thermoviscous losses proportional to the square of the frequency. Attenuation in complex media like biological tissues obeys a frequency power law. In that case, $\mathcal{L}(p)$ can be described by a convolution between p and a kernel function [21] or equivalently, by fractional derivatives [22]. The use of fractional derivatives to describe attenuation in complex media has recently been shown to be linked to the use of multiple relaxation processes [23]. The term on the right-hand side of Eq. (1) represents the nonlinearity of propagation. In the quasi-linear

theory, it is considered as a small correction to the linear equation. The acoustic pressure is written $p = p_1 + p_2$. The pressure p_1 represents the sound pressure at the fundamental frequency f_0. While p_2 is the sound pressure of the second harmonic signal at frequency $2f_0$ and the harmonic signals of higher order are neglected. The fundamental signal pressure p_1 satisfies the linear propagation equation and the second harmonic signal pressure p_2 satisfies the nonlinear propagation equation, where p is approximated to p_1 in the nonlinear term [24]

$$\nabla^2 p_1 - \frac{1}{c_0^2}\frac{\partial^2 p_1}{\partial t^2} + \mathcal{L}(p_1) = 0, \tag{2}$$

$$\nabla^2 p_2 - \frac{1}{c_0^2}\frac{\partial^2 p_2}{\partial t^2} + \mathcal{L}(p_2) = -\frac{\beta}{\rho_0 c_0^4}\frac{\partial^2 p_1^2}{\partial t^2}. \tag{3}$$

The right-hand side of Eq. (3) appears as a perturbation term and can be understood as a source term for p_2 originating from p_1.

B. Angular spectrum approach

When transmitting a pulse of frequency f_0, an angular spectrum approach which decomposes the pulse into monochromatic plane waves is used. This allows the definition of the complex pressure $P(x, y, z)$ as a sum of complex exponential functions

$$p(x, y, z, t) = \frac{1}{2}P(x, y, z, t) + c.c., \tag{4}$$

where $c.c.$ stands for complex conjugate. The method consists of taking a three-dimensional Fourier transform along the time t, and the spatial directions x and y (transverse space), when z is the main propagation direction. The Fourier transform of the complex pressure $P(x, y, z, t)$ is defined as

$$\hat{P}(\mathbf{k}, z) = \iiint P(x, y, z, t)e^{-j(\omega t + k_x x + k_y y)}dtdxdy, \tag{5}$$

where $\mathbf{k}$ is a vector with coordinates $(\omega/c_0, k_x, k_y)$, with ω, k_x, and k_y the temporal angular frequency, and transverse wave numbers in x and y directions, respectively. Using the properties of the Fourier transform of a derivative and of a product, Eqs. (2) and (3) can be written

$$\frac{\partial^2 \hat{P}_1(\mathbf{k}, z)}{\partial z^2} + K^2(\mathbf{k})\hat{P}_1(\mathbf{k}, z) = 0, \tag{6}$$

$$\frac{\partial^2 \hat{P}_2(\mathbf{k}, z)}{\partial z^2} + K^2(\mathbf{k})\hat{P}_2(\mathbf{k}, z) = \frac{\beta\omega^2}{2\rho_0 c_0^4}\hat{P}_1(\mathbf{k}, z) \otimes \hat{P}_1(\mathbf{k}, z). \tag{7}$$

In these equations, $\hat{P}_1$ and $\hat{P}_2$ are the Fourier transforms of the complex pressure P_1 and P_2, respectively, and the symbol $\otimes$ represents a convolution along the three dimensions of $\mathbf{k}$. The imaginary part of $K(\mathbf{k})$ represents the attenuation and is the formulation of the loss operator $\mathcal{L}$ in the frequency domain. Knowing that attenuation in biological tissue obeys a frequency power law

proportional to f^b with $1 \leq b < 2$, we can write

$$K(\mathbf{k}) = \sqrt{k^2 - k_x^2 - k_y^2} - ja(f/10^6)^b, \tag{8}$$

where a is the attenuation factor in neper for a wave of 1 MHz traveling 1 m. The imaginary part of $K(\mathbf{k})$ can be appended *ad hoc* to reflect measured attenuation for a given medium [7]. A more fundamental way to obtain it is to model losses in complex media using fractional derivatives as explained in Ref. [22]. Doing so also gives an expression for the dispersion of the phase velocity that always accompanies a frequency power law attenuation as shown in Eq. (48) of the same reference. In medical ultrasound, the variations of the phase velocity with frequency are very small [25], the effects of dispersion are therefore neglected in the simulations.

In the very near field, the transverse components of the wave numbers k_x and k_y can have large values leading to $k^2 < k_x^2 + k_y^2$ which translates as the presence of evanescent waves. In that case, K is imaginary and those waves are quickly attenuated.

C. Solutions for the angular spectrum approach

A solution of Eq. (6) is

$$\hat{P}_1(\mathbf{k}, z) = \hat{P}_1(\mathbf{k}, z_0)e^{-jK(\mathbf{k})(z-z_0)}. \tag{9}$$

Note that the sign convention in the exponential in Eq. (9) was chosen in conjunction with the sign convention for the imaginary part of $K(\mathbf{k})$ in Eq. (8) to avoid divergence when $z \to \infty$.

The solution of Eq. (7) is the sum of the solution when the right side of the equation is set to zero, $\hat{P}_{2h}$, and a particular solution, $\hat{P}_{2p}$. The homogeneous solution $\hat{P}_{2h}$ has the same form as Eq. (9). To find $\hat{P}_{2p}$, one can express Eq. (7) in terms of an integral equation using one-dimensional Green's functions. As shown by Jing *et al.* in the appendix of Ref. [15], taking into account that they use the opposite sign convention for $K(\mathbf{k})$, the Green's functions in the case of a half space defined by the source plane can be written as

$$G(z, z', \mathbf{k}) = \frac{e^{-jK(\mathbf{k})(z+z')} - e^{-jK(\mathbf{k})(z-z')}}{2jK(\mathbf{k})}, \quad 0 \leq z' \leq z, \tag{10}$$

$$G(z, z', \mathbf{k}) = \frac{e^{-jK(\mathbf{k})(z+z')} - e^{-jK(\mathbf{k})(z'-z)}}{2jK(\mathbf{k})}, \quad z \leq z'. \tag{11}$$

This gives for $\hat{P}_{2p}$

$$\begin{aligned}\hat{P}_{2p}(\mathbf{k}, z) = \frac{jM}{2K(\mathbf{k})}\Bigg(&\int_0^z e^{-jK(\mathbf{k})(z-z')}F(\hat{P}_1)dz' - \int_0^z e^{-jK(\mathbf{k})(z+z')}F(\hat{P}_1)dz' \\ &+ \int_z^{+\infty} e^{-jK(\mathbf{k})(z'-z)}F(\hat{P}_1)dz' - \int_z^{+\infty} e^{-jK(\mathbf{k})(z+z')}F(\hat{P}_1)dz'\Bigg),\end{aligned} \tag{12}$$

where $M = \beta\omega^2/(2\rho_0 c_0^4)$ and $F(\hat{P}_1) = \hat{P}_1(\mathbf{k}, z') \otimes \hat{P}_1(\mathbf{k}, z')$. Jing *et al.* [15] verified numerically that in the weakly nonlinear case the three last integrals in Eq. (12) could be neglected. We can give

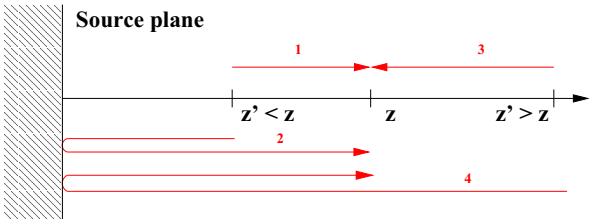

Fig. 1: *Four types of contributions of local sources. Path 1 forms the dominant contributions, all other paths come from back propagation and can be neglected.*

a physical explanation for this. The first integral represents the local sources situated between the source plane and the observation point z propagating forward (path 1 in Fig. 1). It is the dominant contribution. The third integral represents the local sources situated beyond the observation point and back propagating (path 3 in Fig. 1). The second and fourth integrals represent, respectively, the local sources situated between the source and the observation point z, and the sources beyond the observation point. Radiation from both reach the observation point z due to back propagation and reflection on the source plane (paths 2 and 4 in Fig. 1). Neglecting back propagation gives

$$\hat{P}_{2p}(\mathbf{k}, z) \approx \frac{jM}{2K(\mathbf{k})} \int_0^z e^{-jK(\mathbf{k})(z-z')} F(\hat{P}_1) dz' \tag{13}$$

Given that $\hat{P}_{2p}(\mathbf{k}, 0) = 0$, and assuming that

$$\hat{P}_2(\mathbf{k}, 0) = \hat{P}_{2h}(\mathbf{k}, 0) + \hat{P}_{2p}(\mathbf{k}, 0) = 0, \tag{14}$$

we get $\hat{P}_{2h}(\mathbf{k}, z) = 0$. The solution to Eq. (7) therefore reduces to its particular solution, $\hat{P}_2(\mathbf{k}, z) = \hat{P}_{2p}(\mathbf{k}, z)$.

Let us now use the expression for $\hat{P}_1(\mathbf{k}, z)$, given by Eq. (9), to express $\hat{P}_2$ as a function of the linear field $\hat{P}_1$ at depth z_0

$$\begin{aligned} \hat{P}_2(\mathbf{k}, z) = \frac{jM}{2K(\mathbf{k})} \int_0^z \int_{-\infty}^{+\infty} \hat{P}_1(\mathbf{k}', z_0) \hat{P}_1(\mathbf{k} - \mathbf{k}', z_0) e^{-jK(\mathbf{k}')(z'-z_0)} e^{-jK(\mathbf{k}-\mathbf{k}')(z'-z_0)} \\ \times e^{-jK(\mathbf{k})(z-z')} dz' \frac{d\mathbf{k}'}{(2\pi)^3}. \end{aligned} \tag{15}$$

Following an integration along z' from the source plane to the point z of interest, we get [17]

$$\begin{aligned} \hat{P}_2(\mathbf{k}, z) = \frac{jM}{2K(\mathbf{k})} \int_{-\infty}^{+\infty} \hat{P}_1(\mathbf{k}', z_0) \hat{P}_1(\mathbf{k} - \mathbf{k}', z_0) \\ \times H(\mathbf{k}, \mathbf{k}', z, z_0) \frac{d\mathbf{k}'}{(2\pi)^3}, \end{aligned} \tag{16}$$

where

$$H(\mathbf{k}, \mathbf{k}', z, z_0) = z e^{-jK(\mathbf{k})(z-z_0)} e^{j\Lambda(\mathbf{k},\mathbf{k}')(z_0 - z/2)} \mathrm{sinc}\left[\Lambda(\mathbf{k}, \mathbf{k}') \frac{z}{2\pi}\right], \tag{17}$$

and

$$\Lambda(\mathbf{k},\mathbf{k}') = -K(\mathbf{k}) + K(\mathbf{k}') + K(\mathbf{k}-\mathbf{k}'), \tag{18}$$

$$\mathrm{sinc}(x) = \frac{\sin(\pi x)}{\pi x}. \tag{19}$$

Equations (16)−(19) show that the pressure P_2 can be evaluated at any depth from the expression of $\hat{P}_1(\mathbf{k}, z_0)$. This allows for a fast simulation of lateral profiles or pulse shape at any depth without the need for stepwise propagation. The conditions of application for this method are a quasi-linear propagation with $p_1 \gg p_2$, and a homogeneous medium.

D. Linear field evaluation in the focal plane

1) The Fraunhofer approximation:

Although Eq. (9) is correct for any z_0, numerical evaluation is simplified when z_0 is taken as the focal depth. Indeed, in the focal plane of a focused two-dimensional (2D) array the spatial Fourier transform of the wave is proportional to the transducer's aperture function $A(x, y)$. This can be seen when looking at the Fraunhofer approximation of the Huygens principle. The Fraunhofer approximation is valid in the far field of an unfocused transducer or at the focal depth d of a focused transducer and is written for a monochromatic wave of frequency f according to Ref. [26]

$$\begin{aligned} P_1(x,y,d) \approx & \frac{f\cdot\exp(j\omega d/c_0)\exp\left[\frac{j\omega}{2dc_0}(x^2+y^2)\right]}{jc_0 d} \\ & \times \iint A(x_0,y_0)e^{-j\frac{\omega}{c_0 d}(x_0 x+y_0 y)}dx_0 dy_0, \end{aligned} \tag{20}$$

which can be re-arranged as

$$\begin{aligned} P_1(x,y,d) \approx & \frac{dc_0 f\cdot\exp(j\omega d/c_0)\exp\left[\frac{j\omega}{2dc_0}(x^2+y^2)\right]}{j\omega^2} \\ & \times \iint A\left(-\frac{k_x dc_0}{\omega},-\frac{k_y dc_0}{\omega}\right)e^{j(k_x x+k_y y)}dk_x dk_y, \end{aligned} \tag{21}$$

with $k_x = -x_0\omega/(c_0 d)$ and $k_y = -y_0\omega/(c_0 d)$. The integral can be seen as the inverse Fourier transform of the aperture function $A(-k_x dc_0/\omega, -k_y dc_0/\omega)$. The phase term dependent on x and y in front of the integral indicates that $A(-k_x dc_0/\omega, -k_y dc_0/\omega)$ represents the pressure field on a paraboloid with z as its symmetry axis, and that a phase correction is needed to get the field in a transverse plane. Neglecting the proportionality factor and the phase factor which is independent of x and y, a spatial Fourier transform gives

$$\hat{P}_1(k_x,k_y,d) \propto A\left(-\frac{k_x dc_0}{\omega},-\frac{k_y dc_0}{\omega}\right)\otimes\hat{C}(\omega,k_x,k_y), \tag{22}$$

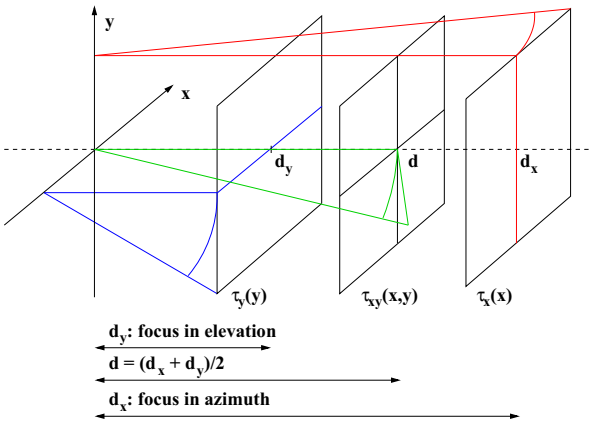

Fig. 2: *Delays $\tau_x(x)$ and $\tau_y(y)$ to focus a 1D array at d_x in azimuth and d_y in elevation, respectively. Delay $\tau_{xy}(x, y)$ to focus a 2D array at focal distance d.*

with

$$\hat{C}(\omega, k_x, k_y) = \mathcal{F}\left\{\exp\left[\frac{j\omega}{2dc_0}(x^2 + y^2)\right]\right\}, \tag{23}$$

where $\mathcal{F}$ designates the 2D spatial Fourier transform in the transverse plane (x, y). Generalizing to the case of a pulse, and assuming the aperture is symmetric along x and y directions giving $A(-x, -y) = A(x, y)$, we get the result

$$\hat{P}_1(\mathbf{k}, d) \propto \hat{P}(\omega) A\left(\frac{k_x dc_0}{\omega}, \frac{k_y dc_0}{\omega}\right) \otimes \hat{C}(\omega, k_x, k_y), \tag{24}$$

where $\hat{P}(\omega)$ is the temporal Fourier transform of the transmitted pulse.

2) When azimuth and elevation focal distances differ:

In the case of transducers with a different focal point in azimuth and elevation as in one-dimensional (1D) arrays for medical imaging [27], the correction is slightly different. We define d_x and d_y the focal distances in azimuth and elevation directions, respectively, as shown in Fig. 2. The distance d is defined as $d = (d_x + d_y)/2$. The pressure field at distance d is approximated by the pressure emitted by a 2D array with d as focus distance. The aperture function of such a transducer is equivalent to the aperture function of the aperture phase shifted to remove the delays responsible for the azimuth and elevation foci to d_x and d_y and replace them with a delay corresponding to a 2D array focused at distance d as described in the previous section. The corresponding delays τ_x, τ_y, and τ_{xy} are defined as

$$\tau_x(x) = \frac{d_x - \sqrt{d_x^2 - x^2}}{c_0}, \tag{25}$$

$$\tau_y(y) = \frac{d_y - \sqrt{d_y^2 - y^2}}{c_0}, \quad \text{and} \tag{26}$$

$$\tau_{xy}(x, y) = \frac{d - \sqrt{d^2 - x^2 - y^2}}{c_0}. \tag{27}$$

The phase shifted aperture function is

$$A'(x,y) = A(x,y)e^{-j\omega\Delta(x,y)/c_0}, \tag{28}$$

where $\Delta(x,y) = \tau_{xy}(x,y) - \tau_x(x) - \tau_y(y)$. Applying the theory described in the previous section, we can write the Fourier transform of the pressure field of a 1D array as

$$\hat{P}_1(\mathbf{k},d) \approx \hat{P}(\omega)A'\left(\frac{k_x dc_0}{\omega}, \frac{k_y dc_0}{\omega}\right) \otimes \hat{C}(\omega,k_x,k_y) \tag{29}$$

III. Implementation

A. Discretizaton

A numerical evaluation of the solution for $\hat{P}_1$, and $\hat{P}_2$ developed in the previous section was implemented using MATLAB® (version 2008b, The MathWorks, Natick, MA). The temporal and spatial frequency domains are defined by the discretization size and the number of samples. The sampling frequency f_s is chosen to satisfy the Nyquist criteria $f_s \geq 2f_{\max}$, where $f_{\max}$ is the largest temporal or spatial frequency. Since both the fundamental and second harmonic fields can be treated as a monofrequency wave modulated by an envelope characterized by the pulse bandwidth B, the maximum frequency can be taken equal to B when working in the temporal frequency domain. The pulse bandwidth B is approximated equal for the fundamental and harmonic fields.

For the spatial frequencies, as shown in Fig. 3 the maximum radial frequencies are approximated to

$$k_{xm} = \frac{\omega_m}{c_0}\frac{D_x}{d} \tag{30}$$

$$k_{ym} = \frac{\omega_m}{c_0}\frac{D_y}{d} \tag{31}$$

for x and y spatial directions, respectively, where ω_m is the maximum temporal radial frequency, and D_x and D_y are the aperture dimensions along x and y, respectively. For the fundamental and harmonic fields, respectively, ω_m should be set to $2\pi(f_0 + B/2)$ and $2\pi(2f_0 + B/2)$, in Eqs. (30) and (31).

The number of samples for temporal and spatial frequencies are determined by the spatial extent for the simulation set by the user. If L_x, L_y, and L_z define the spatial extent in x, y, and z directions, respectively, we have

$$N_x = L_x 2(k_{xm}/2\pi) = L_x\frac{D_x}{c_0 d}\frac{\omega_m}{\pi}, \tag{32}$$

$$N_y = L_y 2(k_{ym}/2\pi) = L_y\frac{D_y}{c_0 d}\frac{\omega_m}{\pi}, \tag{33}$$

$$N_t = \frac{L_z}{c_0}2B, \tag{34}$$

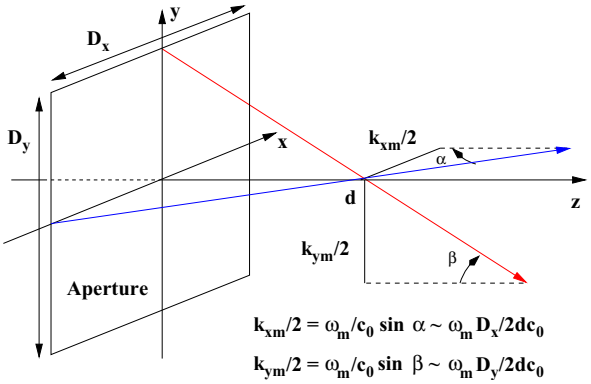

Fig. 3: *Determination of maximum spatial radial frequencies k_{xm} and k_{ym} in x and y directions, respectively.*

where N_x, N_y, and N_t are the number of samples in the spatial and temporal frequency domains, respectively. The simulation domain characterized by L_x and L_y has to be taken large enough to avoid perturbations at large depths from source replica that appear due to spatial aliasing when using the discrete Fourier transform [28]. Using Eqs. (32)−(34), it is easy to see that the sample counts and computational burden will be directly linked to the temporal bandwidth of the transmitted pulse B as well as the ratios of the aperture size to the focal distance D_x/d and D_y/d. A short pulse with a large bandwidth and a large aperture strongly focused are therefore expected to require a relatively long simulation time.

B. Harmonic field computation

While the computation of the fundamental field P_1 is straightforward, the convolution in Eq. (16) is the most computer intensive operation in the evaluation of the harmonic field P_2. If the simulated aperture is assumed symmetric along the x and y axis, the field needs only to be calculated in one quadrant of the transverse plane of interest. The field in the three other quadrants can be deduced by symmetry. In that case, the convolution is estimated using $N_x/2{\cdot}N_y/2{\cdot}N_t$ sums involving matrices whose size increases by one for each sum. The number of operations is therefore of the order of $N_x^2 \cdot N_y^2 \cdot N_t^2$. As an example, we consider a pulse transmitted at frequency $f_0 = 2$ MHz, with a bandwidth $B = 1$ MHz, and an aperture of dimension $D_x = 2$ cm, and $D_y = 2$ cm with a focus distance of $d = 6$ cm. The pulse duration is approximately $1/B = 1$ μs, hence $L_z = 3{\cdot}c_0/B \approx 0.45$ cm is adequate. The transverse dimensions are defined as $L_x = 3$ cm, and $L_y = 3$ cm. We have for the harmonic field

$$N_x = L_x \frac{2D_x(2f_0 + B/2)}{c_0 d} = 60, \tag{35}$$

$$N_y = L_y \frac{2D_y(2f_0 + B/2)}{c_0 d} = 60, \tag{36}$$

$$N_t = L_z \frac{2B}{c_0} = 6, \tag{37}$$

when $c_0 = 1500$ m/s. This gives a number of operations for the convolution of the order of 466×10^6.

IV. Performance of the method

In this section we check the accuracy of the described method, from here on referred to as the quasi-linear (QL) method, for the case of an annular array and a rectangular phased array. For the annular array, the results are compared against the output of the KZKTexas code and a simulation package for three-dimensional (3D) nonlinear wave propagation of wide band pulses from arbitrary transducers called Abersim [29–31]. For the rectangular array, the results are compared against Abersim and measurements. We then compare the time requirements when using each method.

A. Results accuracy

1) Annular array:

An annular array of radius 10 mm and focal distance 60 mm was simulated using the QL method. The results were compared to the results of the KZKTexas code and Abersim. The transmitted pulse had a frequency of 2.2 MHz and a duration of approximately 2 μs. The propagation medium was water, and losses due to thermoviscous effects were neglected. The pulse generated by the QL method in the source plane was used as an input to the KZKTexas code and Abersim. Its maximum input pressure was 92 kPa.

Figure 4 compares the lateral distribution of the pulse normalized root mean square (RMS) obtained by all methods for the fundamental and second harmonic signals at depths 30 mm and 60 mm. The RMS values were computed over the time range $-6\ \mu\text{s} \leq t \leq 6\ \mu\text{s}$, and the pulses were centered at $t = 0\ \mu$s.

Axial profiles for the fundamental and second harmonic signals were also computed using all three methods and are shown in Fig. 5.

The pulse at focus distance ($z = 60$ mm) using all three methods is shown in Fig. 6. It is built by adding the components of the pulse around the fundamental and second harmonic frequency bands.

The pulse RMS fields obtained using the QL simulator for the fundamental and the second harmonic signals can be compared to the results given by the KZKTexas code and Abersim in Fig. 7. The differences between the profiles obtained by the QL simulator and the other methods are displayed in Fig. 8 and never exceed 8 dB over the displayed area.

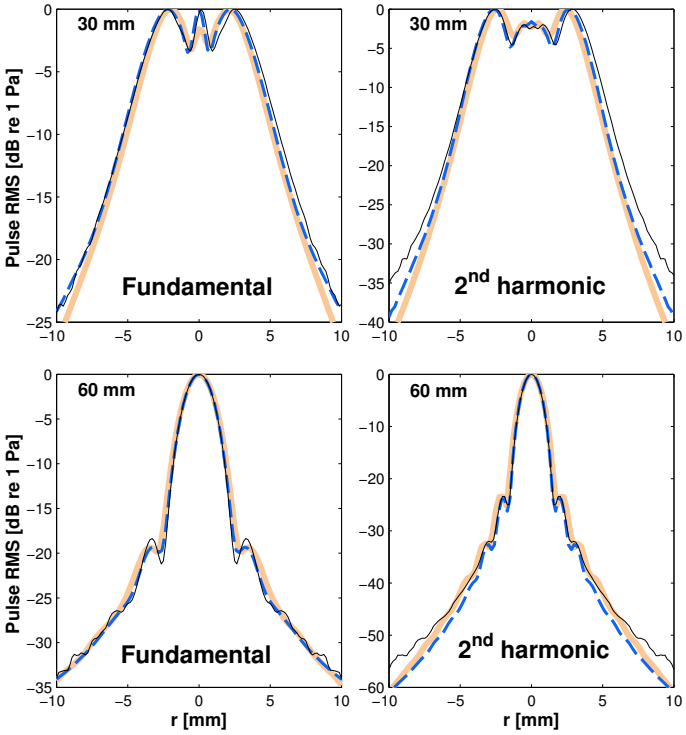

Fig. 4: *Lateral profiles for the fundamental and second harmonic signals at 30 mm (top) and 60 mm depth (bottom). Thick, dashed, and thin lines show the results from the QL simulator, the KZKTexas code, and Abersim, respectively.*

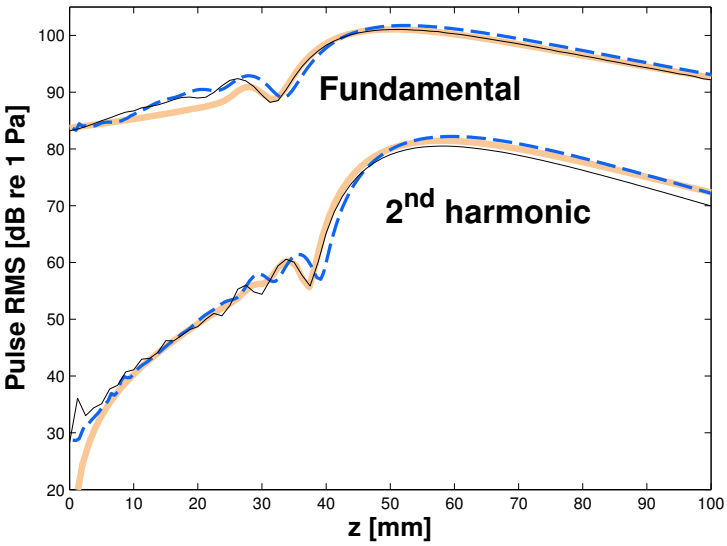

Fig. 5: *Axial profiles for the fundamental and second harmonic signals for an annular array. Thick, dashed, and thin lines show the results from the QL simulator, the KZKTexas code, and Abersim, respectively.*

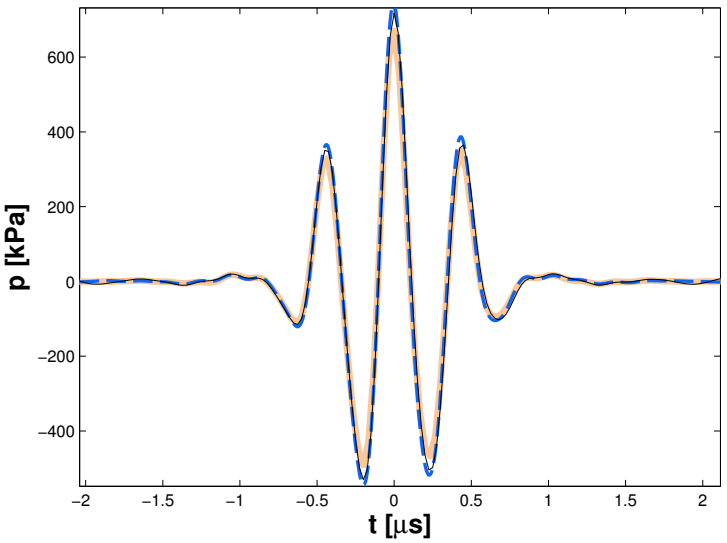

Fig. 6: *Pulse at focus depth. Thick, dashed, and thin lines show the results from the QL simulator, the KZKTexas code, and Abersim, respectively.*

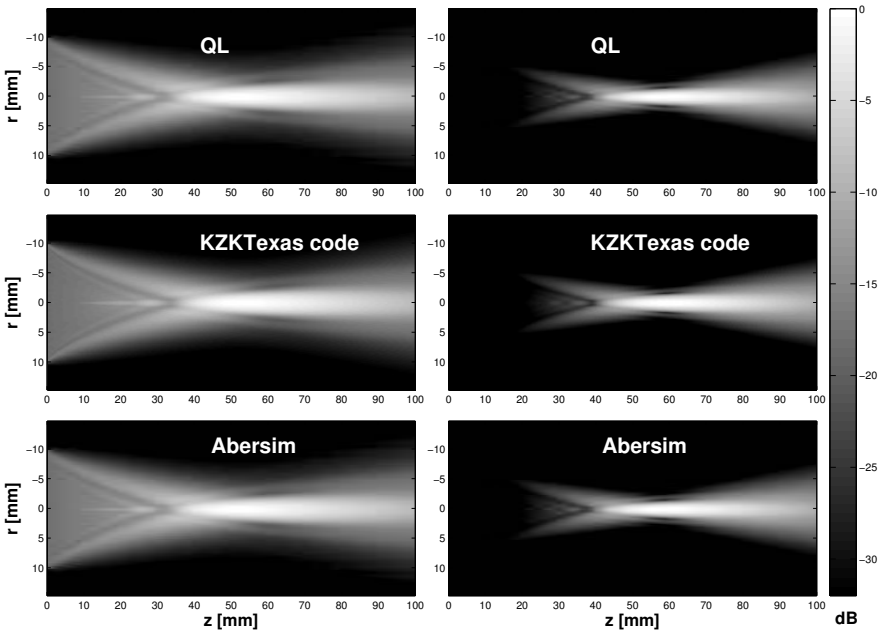

Fig. 7: *Pulse RMS in decibels normalized for the fundamental (left) and second harmonic (right) signals calculated by the QL simulator, the KZKTexas code, and Abersim.*

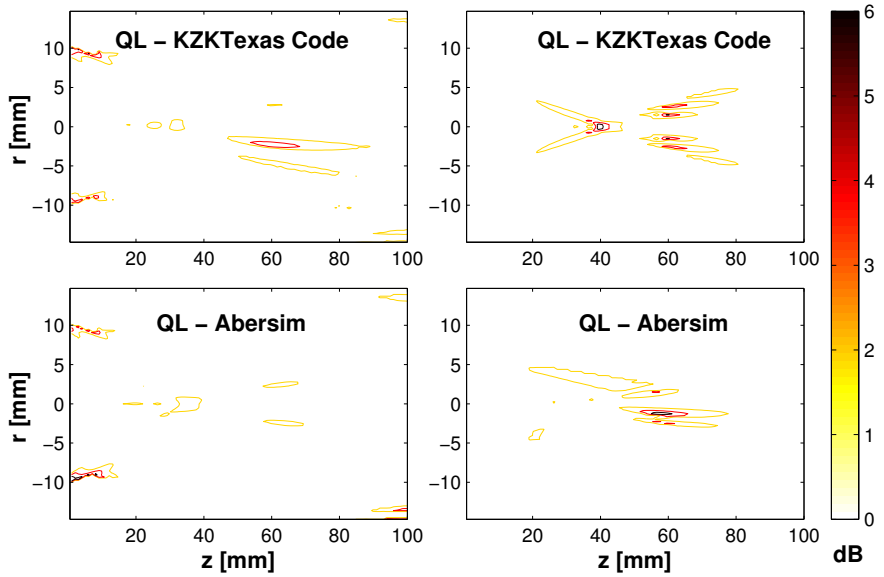

Fig. 8: *Difference between the RMS pressure fields expressed in decibel for the fundamental (left) and second harmonic (right) signals. The top and bottom row show the differences between the profiles obtained by the QL simulator and those obtained by the KZKTexas code and Abersim, respectively.*

The lateral profiles show a good match between the QL method, Abersim, and the KZKTexas code. At 30 mm depth the mismatch averaged over the lateral extent -10 mm $\leq r \leq 10$ mm is below 1.5 dB for the fundamental signal and 3.5 dB for the second harmonic signal. At the focal point at 60 mm the averaged mismatch is below 1 dB and 2.2 dB for the fundamental and second harmonic signal, respectively. The axial profiles show an average mismatch below 1.1 dB and 1.5 dB for the fundamental and second harmonic signal, respectively. The pulse shapes at focus can hardly be distinguished from each other. When considering pressure levels above 50 kPa, the mismatch averaged over the time range -1 μs $\leq t \leq 1$ μs between the QL method and the other methods is below 16 kPa or 14%. This shows that the quasi-linear approximation is valid in this case and that the energy contained outside the fundamental and second harmonic frequency bands can be neglected. Finally, the pulse RMS fields show that the axial and lateral matches are similar away from the propagation axis or at other depths.

2) Rectangular array:

Measurements were done using a M3S phased array connected to a Vivid 7 scanner (GE Vingmed Ultraound AS, Horten, Norway). The transmitted field was recorded in a water tank by a HGL-0085 hydrophone (Onda, Sunnyvale, CA) connected to a digital oscilloscope of type 42 XS (LeCroy, Chestnut Ridge, NY). The fixed focal distance in elevation was 70 mm and the focal distance in azimuth was set to 50 mm. The center frequency of the transmitted pulse was 2.1 MHz. To compare the measurements with the QL method and Abersim, simulations were run considering a rectangular array of dimensions 18 mm in azimuth (x) and 11.5 mm in elevation (y) with the same focus distances as the M3S phase array. In this case, in order to guarantee proper modeling of the pulse, the measurements of the transmitted pulse at depth $z = 60$ mm were used as an input to the QL method. The pulse back propagated to the source plane by the QL method was then used as an input to Abersim. Its maximum input pressure was 147 kPa. The propagation medium was water, and losses due to thermoviscous effects were neglected.

Lateral profiles for the fundamental and second harmonic signals obtained by the QL method and Abersim at both focus depths are compared against the measurements in Fig. 9. As in the case of the annular array, the RMS values were computed over the time range -1.6 μs $\leq t \leq 1.6$ μs, and the pulses were centered around $t = 0$ μs.

Figure 10 compares the axial profiles and Fig. 11 compares the on-axis pulses at both focal depths obtained by the three methods. As in the case of the circular array, the on-axis pulses are built by adding the components of the pulses around the fundamental and second harmonic frequency bands.

The comparison of the lateral profiles show a good agreement. The average mismatch at 50 mm depth when the QL method is compared to the measurements and Abersim is below 3.5 dB and 2.3 dB, respectively. At 70 mm, the mismatch with the measurements and Abersim is below 1.3 dB and 1.4 dB, respectively. The average mismatch for the axial profiles is below 0.7 kPa or 0.7% for the fundamental signal and below 1.6 kPa or 2% for the second harmonic signal. The observant reader will notice that the maximum pressure levels are reached at slightly larger depth in the case of the measurements compared to what the simulations give. This mismatch of approximately 2 mm can be explained by the positioning uncertainty of the measurement setup. The simulation results for the pulse shape at focus depths also match well with the measurements. When considering pressure levels above 100 kPa, the relative mismatch at 50 mm depth averaged over the time range -1.6 μs $\leq t \leq 1.6$ μs is below 6% and 25% when comparing the QL method to Abersim or to the

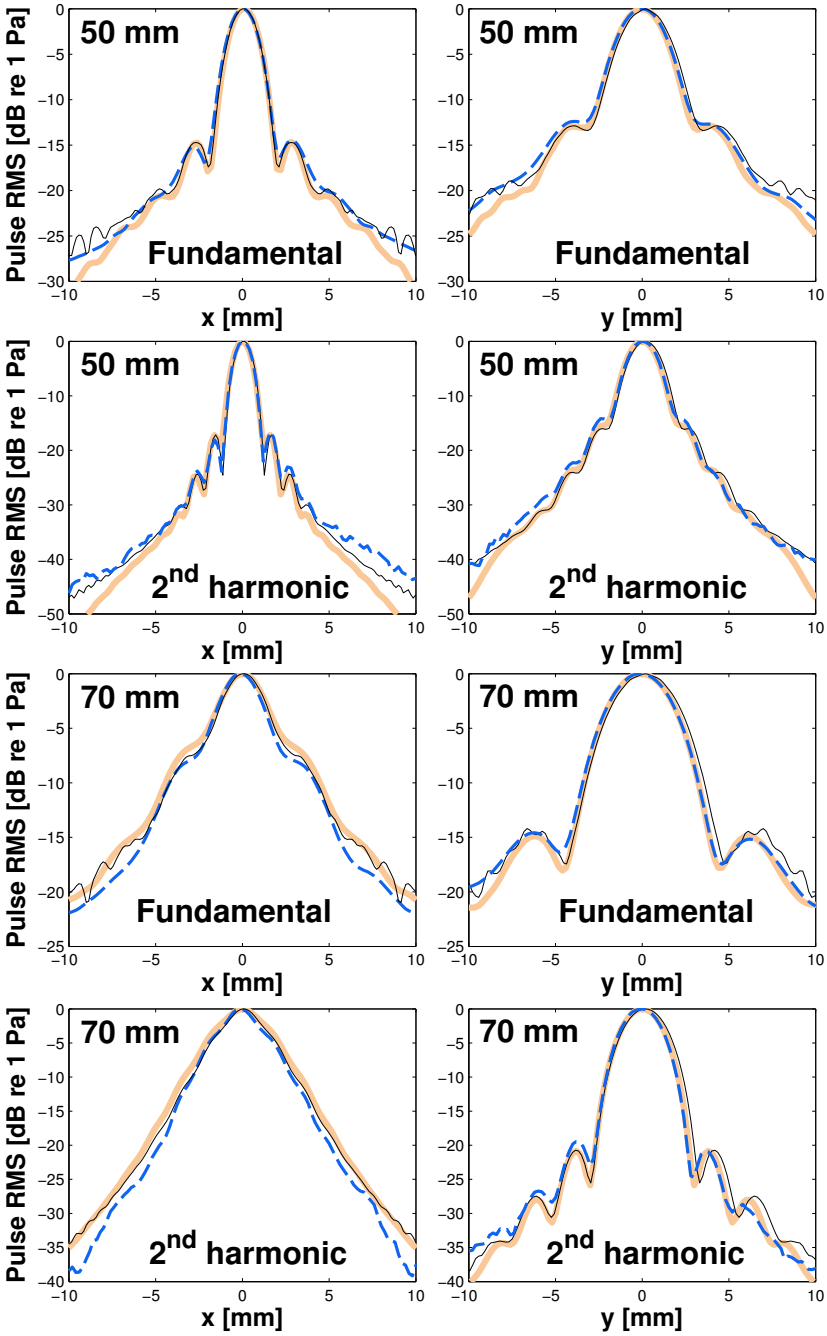

Fig. 9: *Lateral profiles at azimuth focus depth, $z = 50$ mm (first two rows) and elevation focus depth, $z = 70$ mm (last two rows), for fundamental and second harmonic signals, along the azimuth (left) and elevation (right) directions. Thick, dashed, and thin lines show the results for the QL simulator, the measurements, and Abersim respectively*

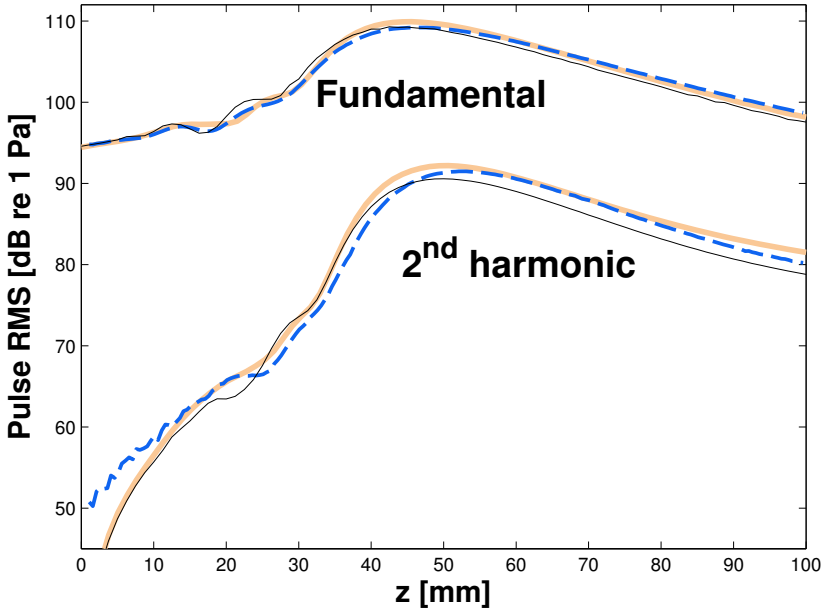

Fig. 10: *Axial profiles obtained by the QL method (thick), measurements (dashed), and Abersim (thin) for the fundamental and second harmonic signals*

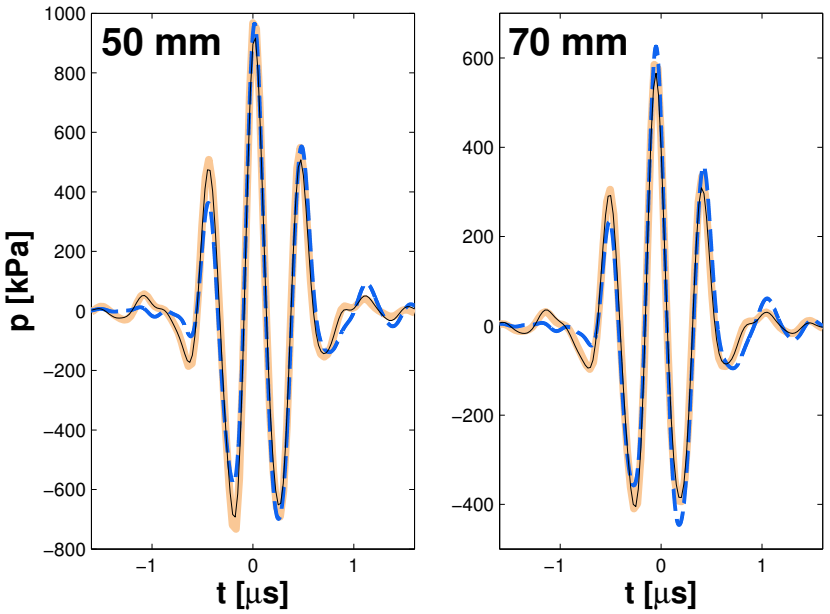

Fig. 11: *Pulses obtained by the QL method (thick), measurements (dashed), and Abersim (thin) at the azimuth (left) and elevation (right) focus depths. Note the different vertical scales.*

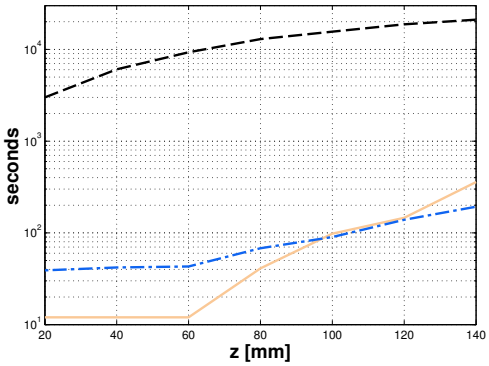

Fig. 12*: Execution time required by the QL method (solid), the KZKTexas code (dash-dotted), and Abersim (dashed) to generate a lateral profile at different depths.*

measurements, respectively. At 70 mm depth, the averaged mismatch is below 3% and 19% when comparing to Abersim and to the measurements, respectively.

B. Speed evaluation

We compared the execution time of the QL simulator, the KZKTexas code, and Abersim. The time required for each method to produce a lateral profile for different depths was recorded and is shown in Fig. 12. The transducer and pulse used in the simulations were the same as described in Sec. IV A 1 for the case of the annular array with a focal distance of 60 mm. The machine used to run the simulations had 8 GB of memory and ran on an Intel (Intel, Santa Clara, CA) eight core 64-bit processor at 2.9 GHz clock frequency under the operating system Linux Red Hat (Red Hat, Raleigh, NC) release 5.7. We used version R2008b of MATLAB.

For this comparison, the spatial extent of the simulations was set to the minimum size required to avoid perturbations from source replicas generated by the discrete spatial Fourier transform. The spatial extent of the simulations therefore increased with depth beyond the focus depth. This is the reason why the simulation time increases for the QL method for depth beyond the focus depth ($z > 60$ mm) although no stepwise propagation from the source is required. The simulation spatial extent for the QL method and KZKTexas code were taken equal for each depth.

C. Limitations of the method

Since the quasi-linear assumption is valid only in the case of weak nonlinearity, it is expected that the QL method should give less accurate results in the case of strong linearity. Figure 13 shows the maximum negative pressure of the on-axis pulse at focus as a function of the maximum pressure of the pulse at transmission given by measurements and the QL simulator. The measurements were done with the same setup as described in Sec. IV A 2 with the azimuth focus set to 70 mm instead of 50 mm. The comparison is done for the fundamental and the second harmonic signals.

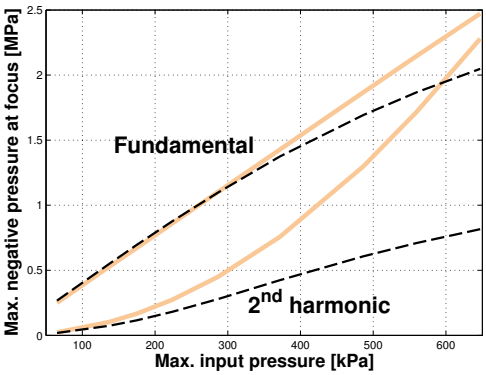

Fig. 13*: Maximum negative pressure at focal depth as a function of the maximum input pressure of the transmitted pulse for the fundamental and second harmonic signals. Solid and dashed lines show the results for the QL method, and the measurements, respectively.*

Figure 13 shows that the maximum negative pressure level estimated by the QL method is linearly proportional to the input pressure for the fundamental signal while for the second harmonic signal it is proportional to the input pressure level squared. This is predicted by the quasi-linear theory as shown by Eqs. (9) and (16).

V. Discussion

The results given by the QL simulator appear to be comparable to the results given by recognized simulators such as the KZKTexas code and Abersim. It is quite difficult to compare the speed of each method due to the differences in their way of operating. The KZKTexas code and Abersim propagate the field stepwise from the source plane to the desired depth while the QL method estimates the field at any depth without stepwise propagation. While Abersim and the QL method propagate the field in 3D allowing for any transducer geometry, the KZKTexas code propagates the field in 2D limiting its use to axisymmetric transducers. The KZKTexas code is written in Fortran and compiled, Abersim is a mix of compiled C routines and MATLAB code, and the QL method is written in MATLAB code only. In addition, the parameter values used in each method like the propagation step size or the spatial extent of the simulation influence the execution time. For the QL method and the KZKTexas code, one can define the spatial extent of the simulation. An increase of the simulation's spatial extent has a greater impact on the execution time of the QL method compared to the KZKTexas code since it applies to both the elevation and azimuth directions while it only affects the lateral direction for the KZKTexas code. This explains why the increase in execution time with depth is greater for the QL method than for the KZKTexas code.

Despite all these differences, Fig. 12 gives an indication of the relative speed performance of our implementation of the QL method. It is clearly the fastest way to estimate a lateral profile for depths below the focus point. The QL method is up to 1000 times faster than Abersim for simulation depths below focus depth, and around 100 times faster beyond focus depth. The speed performance degrades if the spatial extent of the simulation becomes increasingly large. It should be mentioned that no particular effort was made to optimize the execution speed of the QL method.

To further improve its speed, the code could be translated to C language and compiled or a faster 2D version could be written for axisymmetric transducers.

The quasi-linear theory neglects the harmonic signals of order greater than two. This is where the method encounters some limitations. In practice, the energy transferred to harmonic signals of order greater than two increases with the input pressure level. The consequences of this is that the QL method over-estimates the levels of the fundamental and second harmonic signals at high input pressure level as shown in Fig. 13. In this particular case, the fundamental signal starts to get over-estimated for input pressure levels larger than about 350 kPa while the second harmonic signal starts to get over-estimated for input pressure levels larger than about 160 kPa. These maximum input pressure values are only representative of the chosen model and can also vary with parameters such as the aperture apodization, the focal distance, or the attenuation in the medium. Beyond these levels the harmonic signals of order greater than two cannot be neglected and the quasi-linear method is less adapted. This limitation on the input pressure level can be somewhat relaxed if one is only interested in the lateral pressure profiles as their shape is less affected by the over-estimation previously mentioned.

If the limitation on the input power imposed by the quasi-linear assumption can be satisfied in many cases in medical ultrasound imaging, the assumption that the pulse propagates in a homogeneous medium however is rarely satisfied. It is a drawback that the method cannot model reverberation as well as phase and amplitude aberrations. However, if the simulator is used to predict the pulse pressure level in the case when several focal depths are used in order to build an image from partial images, the presented model assuming a propagation in a homogeneous media might give sufficient precision.

VI. Conclusion

In this work, we have explained the theory and the physics that allow us to quickly estimate at any depth the pressure pulse transmitted by a transducer of arbitrary geometry. The solution is based on the quasi-linear theory and approximates the pulse by the sum of its components around the fundamental and the second harmonic frequency bands. The method does not require a step-wise propagation from the source plane and provides a full 3D estimate of the pulse in a transverse plane. The only inputs to the simulator are the aperture geometry with its weighting and the pulse shape and amplitude at focus depth. An obvious potential application for this simulator is medical ultrasound imaging. For this purpose, the simulator can model 1D arrays with different azimuth and elevation focus depths.

The accuracy and speed performance of the simulator has been compared to recognized state-of-the-art simulators: the KZKTexas code for axisymmetric transducers and Abersim for transducers of arbitrary geometry. Measurements were also compared to the results given by our method. These comparisons showed a relative mismatch between pulse shape estimates below 14% and allow us to conclude that the presented method is faster than the other methods, up to 1000 times faster than Abersim for moderate depth, and around 100 times faster at large depths.

The method encounters limitations in speed performance for depths well beyond the focal depth. In that case, the full 3D computation in a large discretization plane increases the computation time. The input pressure must also be kept below an upper limit otherwise the method over-estimates the pressure levels.

The implementation of the method that has been tested is not optimized for computation time. It is written in MATLAB code and is interpreted, not compiled. Some further work could consist of optimizing the method and possibly implementing it using graphical processing units. Another interesting future test would be to compare the results of the simulator with measurements of sound propagation in a medium resembling biological tissue.

Bibliography

[1] H. Becher, K. Tiemann, T. Schlosser, C. Pohl, N. C. Nanda, M. A. Averkiou, J. Powers, and B. Lüderitz, "Improvement in endocardial border delineation using tissue harmonic imaging," *Echocardiogr.*, vol. 15, no. 5, pp. 511–517, 1998.

[2] R. J. Graham, W. Gallas, J. S. Gelman, L. Donelan, and R. E. Peverill, "An assessment of tissue harmonic versus fundamental imaging modes for echocardiographic measurements," *J. Am. Soc. Echocardiogr.*, vol. 14, no. 12, pp. 1191–1196, 2001.

[3] G. A. Whalley, G. D. Gamble, H. J. Walsh, S. P. Wright, S. Agewall, N. Sharpe, and R. N. Doughty, "Effect of tissue harmonic imaging and contrast upon between observer and test-retest reproducibility of left ventricular ejection fraction measurement in patients with heart failure," *Eur. J. Heart Failure*, vol. 6, no. 1, pp. 85–93, 2004.

[4] S. Tanaka, O. Oshikawa, T. Sasaki, T. Ioka, and H. Tsukuma, "Evaluation of tissue harmonic imaging for the diagnosis of focal liver lesions," *Ultrasound Med. Biol.*, vol. 26, no. 2, pp. 183–187, 2000.

[5] T. Schmidt, C. Hohl, P. Haage, M. Blaum, D. Honnef, C. Weiss, G. Staatz, and R. W. Günther, "Diagnostic accuracy of phase-inversion tissue harmonic imaging versus fundamental B-mode sonography in the evaluation of focal lesions of the kidney," *AJR, Am. J. Roentgenol.*, vol. 180, no. 6, pp. 1639–1647, 2003.

[6] F. A. Duck, "Nonlinear acoustics in diagnostic ultrasound," *Ultrasound Med. Biol.*, vol. 28, no. 1, pp. 1–18, 2002.

[7] P. T. Christopher and K. J. Parker, "New approaches to the linear propagation of acoustic fields," *J. Acoust. Soc. Am.*, vol. 90, no. 1, pp. 507–521, Jul. 1991.

[8] ——, "New approaches to nonlinear diffractive field propagation," *J. Acoust. Soc. Am.*, vol. 90, no. 1, pp. 488–499, Jul. 1991.

[9] Y. S. Lee, R. Cleveland, and M. F. Hamilton, "KZKTexas," http://people.bu.edu/robinc/kzk/, (Last viewed May 30, 2012), Oct. 1998.

[10] Y. S. Lee and M. F. Hamilton, "Time-domain modeling of pulsed finite-amplitude sound beams," *J. Acoust. Soc. Am.*, vol. 97, pp. 906–917, 1995.

[11] X. Yan and M. F. Hamilton, "Angular spectrum decomposition analysis of second harmonic ultrasound propagation and its relation to tissue harmonic imaging," in *Proceedings of the*

4th International Workshop on Ultrasonic and Advanced Methods for Nondestructive Testing and Material Characterization, N. Dartmouth, MA, Jun. 2006, pp. 11–24.

[12] Y. Du, H. Jensen, and J. A. Jensen, "Angular spectrum approach for fast simulation of pulsed non-linear ultrasound fields," in *Proc. IEEE Ultrason. Symp. 2011*, Orlando, FL, Oct. 2011.

[13] J. A. Jensen, "Field: A program for simulating ultrasound systems," *Med. Biol. Eng. Comput.*, vol. 34, Suppl. 1, pt. 1, pp. 351–353, 1996.

[14] J. A. Jensen and N. B. Svendsen, "Calculation of pressure fields from arbitrarily shaped, apodized, and excited ultrasound transducers," *IEEE Trans. Ultrason. Ferroelectr. Freq. Control*, vol. 39, no. 2, pp. 262–267, 1992.

[15] Y. Jing, M. Tao, and G. T. Clement, "Evaluation of a wave-vector-frequency-domain method for nonlinear wave propagation," *J. Acoust. Soc. Am.*, vol. 129, no. 1, pp. 32–46, Jan. 2011.

[16] F. Varray, A. Ramalli, C. Cachard, P. Tortoli, and O. Basset, "Fundamental and second-harmonic ultrasound field computation of inhomogeneous nonlinear medium with a generalized angular spectrum method," *IEEE Trans. Ultrason. Ferroelectr. Freq. Control*, vol. 58, no. 7, pp. 1366–1376, Jul. 2011.

[17] H. Torp, T. F. Johansen, and J. S. Haugen, "Nonlinear wave propagation - A fast 3D simulation method based on quasi-linear approximation of the second harmonic field," in *Proc. IEEE Ultrason. Symp. 2002*, vol. 1, Munich, Germany, Oct. 2002, pp. 567–570.

[18] S. Dursun, T. Varslot, T. F. Johansen, B. Angelsen, and H. Torp, "Fast 3D simulation of 2nd harmonic ultrasound field from arbitrary transducer geometries," in *Proc. IEEE Ultrason. Symp. 2005*, vol. 4, Rotterdam, Netherlands, Sep. 2005, pp. 1964–1967.

[19] J. Lu, H. Zou, and J. F. Greenleaf, "Biomedical ultrasound beam forming," *Ultrasound Med. Biol.*, vol. 20, no. 5, pp. 403–428, 1994.

[20] M. F. Hamilton and C. L. Morfey, "Model equations," in *Nonlinear Acoustics*, M. F. Hamilton and D. T. Blackstock, Eds. San Diego, CA: Academic, Dec. 1998, ch. 3, pp. 41–63.

[21] T. L. Szabo, "Time domain wave equations for lossy media obeying a frequency power law," *J. Acoust. Soc. Am.*, vol. 96, pp. 491–500, Jul. 1994.

[22] F. Prieur and S. Holm, "Nonlinear acoustic wave equations with fractional loss operators," *J. Acoust. Soc. Am.*, vol. 130, no. 3, pp. 1125–1132, Sep. 2011.

[23] S. P. Näsholm and S. Holm, "Linking multiple relaxation, power-law attenuation, and fractional wave equations," *J. Acoust. Soc. Am.*, vol. 130, no. 5, pp. 3038–3045, Nov. 2011.

[24] M. F. Hamilton, "Sound beams," in *Nonlinear Acoustics*, M. F. Hamilton and D. T. Blackstock, Eds. San Diego, CA: Academic, Dec. 1998, ch. 8, pp. 233–261.

[25] M. Odonnell, E. T. Jaynes, and J. G. Miller, "Kramers-kronig relationship between ultrasonic attenuation and phase velocity," *J. Acoust. Soc. Am.*, vol. 69, no. 3, pp. 696–701, Mar. 1981.

[26] J. W. Goodman, "Fresnel and Fraunhofer diffraction," in *Introduction to Fourier optics*, 3rd ed. Greenwood Village, CO: Roberts & Company, 2005, ch. 4, pp. 74–75.

[27] D. G. Wildes, R. Y. Chiao, C. M. W. Daft, K. W. Rigby, L. S. Smith, and K. E. Thomenius, "Elevation performance of 1.25D and 1.5D transducer arrays," *IEEE Trans. Ultrason. Ferroelectr. Freq. Control*, vol. 44, no. 5, pp. 1027–1037, Sep. 1997.

[28] P. Wu, R. Kazys, and T. Stepinski, "Analysis of the numerically implemented angular spectrum approach based on the evaluation of two-dimensional acoustic fields. Part II. Characteristics as a function of angular range," *J. Acoust. Soc. Am.*, vol. 99, pp. 1349–1359, Mar. 1996.

[29] T. Varslot and G. Taraldsen, "Computer simulation of forward wave propagation in soft tissue," *IEEE Trans. Ultrason. Ferroelectr. Freq. Control*, vol. 52, no. 9, pp. 1473–1482, Sep. 2005.

[30] T. Varslot and S. E. Måsøy, "Forward propagation of acoustic pressure pulses in 3D soft biological tissue," *Model. Identif. Contr.*, vol. 27, no. 3, pp. 181–200, Jul. 2006.

[31] M. E. Frijlink, H. Kaupang, T. Varslot, and S. E. Måsøy, "Abersim: A simulation program for 3D nonlinear acoustic wave propagation for arbitrary pulses and arbitrary transducer geometries," in *Proc. IEEE Ultrason. Symp. 2008*. Beijing, China: IEEE, Nov. 2008, pp. 1282–1285.

Paper VI

3D simulation of parametric ultrasound fields

F. Prieur

Proceedings of the 19th International Symposium on Nonlinear Acoustics (extended version), Tokyo, Japan, May 2012.

3D simulation of parametric ultrasound fields

F. Prieur

Abstract— Parametric sonar is widely used for seafloor characterization, sub-bottom object detection, or underwater communication. It takes advantage of the interaction between two primary beams transmitted at slightly different frequencies. Due to nonlinear propagation, two secondary beams at the sum and difference frequency are generated. The signal at the difference frequency combines sub-bottom penetration due to low attenuation, and high resolution due to an acoustic beam with a narrow main lobe and negligible sidelobes. It allows to generate directional low frequency beams with transducers of reasonable size. A method that estimates the pressure level and the beam profile of the signals at the sum and difference frequency is presented. It solves the Westervelt equation in the frequency domain under the quasi-linear approximation. A full three dimensional estimate of the radiated fields can be computed at any depth without the need for stepwise propagation from the source plane. The method applies to two dimensional transducers of arbitrary geometry and distribution. It does not rely on the parabolic approximation and is not limited to monochromatic signals, thus allowing to model pulses with wide bandwidth. The limits of the method come from the assumptions of a homogeneous medium and input pressure levels sufficiently low to satisfy the quasi-linear approximation. The obtained results in the case of a flat piston transducer compare favorably to previous measurements and numerical estimates from proved methods.

I. Introduction

Parametric sonar is a powerful tool used for long range exploration in the sea, seafloor characterization [1,2], sub-bottom object detection [3,4], and underwater communications [5]. It combines the directivity of high frequency sound signals with the low attenuation at low frequencies. The physics of parametric signals consists of transmitting two beams of slightly different frequencies that overlap in space. Due to the nonlinearity of sound propagation in water, signals at the sum and difference frequency appear. The low attenuation of the created field at the difference frequency allows the pulse to propagate to large ranges in water or penetrate deep into the sea bottom. Its spatial distribution follows the spatial distribution of the primary beams and gives a directional low frequency beam with almost no sidelobe. Accurate estimates of the pressure level and spatial distribution of the second order signals can contribute to adequately dimension a parametric sonar system. The requirements in spatial resolution and pressure level of the second order signals dictate the size of the transducers, as well as the transmitted frequencies and the input powers [6]. Modeling of parametric sonar can be classified in roughly three categories [7,8]: absorption limited arrays, spreading loss limited arrays, and saturation limited arrays. Many models that fit each category have been developed [9–12]. They are based upon approximations for the region of nonlinear interaction and for the beam patterns of the transmitted pulses. Except for simple cases they do not provide a closed expression for the lateral or axial profiles. Later models for parametric signals have solved a nonlinear wave propatation equations using the quasi-linear approximation [13–15]. If the results given by these models are more precise and have a larger domain of validity than the first methods, they still make some assumptions or approximations on the transducer geometry or the transmitted beam profiles.

In this article we present a method that estimates the parametric signals by solving the Westervelt equation under the quasi-linear approximation. The method provides a full 3D estimate of a beam profile at any depth without stepwise propagation. It can model any transducer geometry and any type of power law attenuation.

The first part of this article presents the theory the model is based on and the expressions for the parametric signals at the sum and difference frequency. The second part compares the estimates given by the method with results from other recognized methods and measurements. Finally, we discuss the advantages and weaknesses of the method.

II. Theory

A. Quasi-linearity and angular spectrum approach

The nonlinear propagation of sound in a thermo-viscous fluid can be described by the Westervelt equation [16]

$$\nabla^2 p - \frac{1}{c_0^2}\frac{\partial^2 p}{\partial t^2} + \frac{\delta}{c_0^4}\frac{\partial^3 p}{\partial t^3} = -\frac{\beta}{\rho_0 c_0^4}\frac{\partial^2 p^2}{\partial t^2}, \tag{1}$$

where ∇^2 is the Laplacian operator, p, c_0, ρ_0, δ, and β represent the acoustic pressure, the sound speed, the medium density, the diffusivity of sound, and the coefficient of nonlinearity, respectively. In the quasi-linear approximation, the sound pressure p is approximated by the sum of the first and second order sound fields, respectively p_1 and p_2, while the sound fiels of higher order are neglected. The propagation equations for p_1 and p_2 are, respectively

$$\nabla^2 p_1 - \frac{1}{c_0^2}\frac{\partial^2 p_1}{\partial t^2} + \frac{\delta}{c_0^4}\frac{\partial^3 p_1}{\partial t^3} = 0 \quad \text{and} \tag{2}$$

$$\nabla^2 p_2 - \frac{1}{c_0^2}\frac{\partial^2 p_2}{\partial t^2} + \frac{\delta}{c_0^4}\frac{\partial^3 p_2}{\partial t^3} = -\frac{\beta}{\rho_0 c_0^4}\frac{\partial^2 p_1^2}{\partial t^2}. \tag{3}$$

The angular spectrum approach (ASA) used in the presented method decomposes the pulse in a sum of monochromatic plane waves. The complex pressure $P(x, y, z, t)$ can therefore be introduced as a sum of complex exponentials and is related to the real pressure as follows

$$p(x, y, z, t) = \frac{1}{2}P(x, y, z, t) + c.c. \tag{4}$$

where $c.c.$ stands for complex conjugate. Since the ASA solves the propagation of sound in the frequency domain, a three-dimensional Fourier transform along the time t and the transverse spatial directions x, and y is introduced and we can define the Fourier transform of the complex pressure as

$$\hat{P}(\mathbf{k}, z) = \iiint P(x, y, z, t)e^{-j(\omega t + k_x x + k_y y)}dxdydt, \tag{5}$$

where $\mathbf{k}$ is a vector with coordinates $(\omega/c_0, k_x, k_y)$ with ω, k_x, and k_y the angular temporal frequency and spatial wave numbers in the x and y directions, respectively.

B. Solutions of parametric signals

In the case of a parametric sonar, two pulses with a slightly different center frequencies f_a and f_b are transmitted. Callling P_a and P_b the complex pressures of these primary beams, the quasi-linear theory approximates the total pressure as the sum of

$$P_1 = P_a + P_b \quad \text{and} \quad P_2 = \frac{1}{2}(P_a^2 + P_b^2 + 2P_aP_b - 2P_aP_b^*) \tag{6}$$

where the star denotes the complex conjugate. In the expression of P_2, the first two terms represent the second harmonic issued from the interaction of each primary beam with itself. The third and fourth terms represent the secondary sound fields at the sum and difference frequency $f_p = f_a + f_b$ and $f_m = f_a - f_b$, respectively assuming $f_a > f_b$. They are due to the interaction of the primary beams with each other. The solutions for the fundamental of each transmitted beam propagating linearly satisfy the following equations

$$\frac{\partial^2 \hat{P}_t(\mathbf{k}, z)}{\partial z^2} + K_t^2(\mathbf{k})\hat{P}_t(\mathbf{k}, z) = 0 \tag{7}$$

where

$$K_t^2(\mathbf{k}) = \omega_t^2/c_0^2 - k_x^2 - k_y^2 - j\delta\omega_t^3/c_0^4, \tag{8}$$

and the subscript t should be replaced by a or b when referring to the signal transmitted at frequency f_a or f_b, respectively. The solution for primary beams at depth z is therefore

$$\hat{P}_t(\mathbf{k}, z) = \hat{P}_t(\mathbf{k}, 0)e^{-jzK_t(\mathbf{k})}. \tag{9}$$

As Eqs. (8) and (9) show, the imaginary part of K_t describes the attenuation due to thermo-viscous effects. In the low frequency approximation, this attenuation is proportional to the square of the frequency. For media like sand, clay, or sediments the frequency dependency of the attenuation differs [17]. An ad-hoc modification of the imaginary part of K_t allows modeling of a power law attenuation characteristic of such complex media.

In the rest of the document the subscripts p and m refer to the signals at the sum and difference frequency, respectively. The solution for the signal pressures P_p and P_m satisfy the following equations:

$$\frac{\partial^2 \hat{P}_p(\mathbf{k}, z)}{\partial z^2} + K_p^2(\mathbf{k})\hat{P}_p(\mathbf{k}, z) = \frac{\beta\omega_p^2}{\rho_0 c_0^4}\hat{P}_a(\mathbf{k}, z) \otimes \hat{P}_b(\mathbf{k}, z) \tag{10}$$

$$\frac{\partial^2 \hat{P}_m(\mathbf{k}, z)}{\partial z^2} + K_m^2(\mathbf{k})\hat{P}_m(\mathbf{k}, z) = \frac{-\beta\omega_m^2}{\rho_0 c_0^4}\hat{P}_a(\mathbf{k}, z) \otimes \hat{P}_b^*(\mathbf{k}, z) \tag{11}$$

when the Fourier transform of $P_b^*(x, y, z, t)$ is assumed equal to $\hat{P}_b^*(\mathbf{k}, z)$. This is verified in z=0 if the aperture function is symmetric in both transversal directions. A solution to a similar equation presented in Ref. [18] allows us to write

$$\hat{P}_p(\mathbf{k}, z) \approx \frac{jM_p}{K_p(\mathbf{k})}\int_0^z e^{-jK_p(\mathbf{k})(z-z')}\hat{P}_a(\mathbf{k}, z') \otimes \hat{P}_b(\mathbf{k}, z')dz', \tag{12}$$

$$\hat{P}_m(\mathbf{k}, z) \approx \frac{-jM_m}{K_m(\mathbf{k})}\int_0^z e^{-jK_m(\mathbf{k})(z-z')}\hat{P}_a(\mathbf{k}, z') \otimes \hat{P}_b^*(\mathbf{k}, z')dz', \tag{13}$$

Using the expression for $\hat{P}_a(\mathbf{k}, z)$ and $\hat{P}_b(\mathbf{k}, z)$ given in Eq. (9) and after integrating along z' as shown in Ref. [19], we get

$$\hat{P}_p(\mathbf{k}, z) \approx \frac{M_p}{K_p(\mathbf{k})}\iiint \hat{P}_a(\mathbf{k}', 0)\hat{P}_b(\mathbf{k} - \mathbf{k}', 0)H_p(\mathbf{k}, \mathbf{k}', z)\frac{d\mathbf{k}'}{(2\pi)^3}, \tag{14}$$

$$\hat{P}_m(\mathbf{k}, z) \approx \frac{-M_m}{K_m(\mathbf{k})}\iiint \hat{P}_a(\mathbf{k}', 0)\hat{P}_b^*(\mathbf{k} - \mathbf{k}', 0)H_m(\mathbf{k}, \mathbf{k}', z)\frac{d\mathbf{k}'}{(2\pi)^3}. \tag{15}$$

where

$$M_p = \beta\omega_p^2/(\rho_0 c_0^4), \quad H_p(\mathbf{k}, \mathbf{k}', z) = ze^{-jK_p(\mathbf{k})z}e^{-j\Lambda_p(\mathbf{k},\mathbf{k}')z/2}\mathrm{sinc}\left[\Lambda_p(\mathbf{k}, \mathbf{k}')\frac{z}{2\pi}\right], \tag{16}$$

$$M_m = \beta\omega_m^2/(\rho_0 c_0^4), \quad H_m(\mathbf{k}, \mathbf{k}', z) = ze^{-jK_m(\mathbf{k})z}e^{-j\Lambda_m(\mathbf{k},\mathbf{k}')z/2}\mathrm{sinc}\left[\Lambda_m(\mathbf{k}, \mathbf{k}')\frac{z}{2\pi}\right], \tag{17}$$

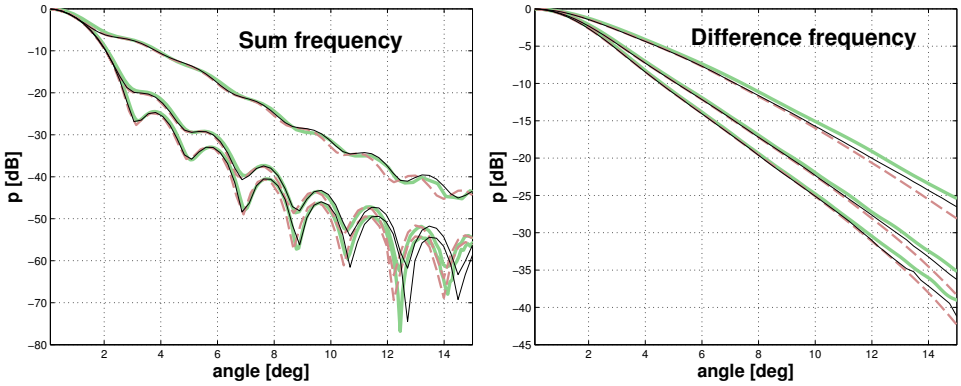

Fig. 1: *Lateral profiles for the signals at the sum frequency: 28 kHz (left) and difference frequency: 3 kHz (right) obtained at 7.5 m, 16.9 m, and 27.2 m by the QL method (bold), the Ding method (dashed), and the Garrett method (thin). Note the different vertical scale for each plot.*

and

$$\Lambda_p(\mathbf{k},\mathbf{k}') = -K_p(\mathbf{k}) + K_a(\mathbf{k}') + K_b(\mathbf{k}-\mathbf{k}'), \tag{18}$$

$$\Lambda_m(\mathbf{k},\mathbf{k}') = -K_m(\mathbf{k}) + K_a(\mathbf{k}') - K_b(\mathbf{k}-\mathbf{k}'), \tag{19}$$

$$\mathrm{sinc}(x) = \frac{\sin(\pi x)}{\pi x}. \tag{20}$$

Equations (14) to (20) show that the pressures P_p and P_m can be evaluated from the expression of $\hat{P}_a(\mathbf{k},0)$ and $\hat{P}_b(\mathbf{k},0)$. This allows for a fast simulation of lateral profiles or pulse shape at any depth without the need for stepwise propagation. The conditions of application for this method are a quasi-linear propagation with $p_1 \gg p_2$, and a homogeneous medium.

III. Results

A simulator that solves Eqs. (14) and (15) was implemented using MATLAB® (version 2011a, The MathWorks, Natick, MA). In order to check the accuracy of the method, the parametric source described in Ref. [20] was modeled. It consists of a flat piston of radius $a = 0.87$ m transmitting two beams at $f_a = 15$ kHz and $f_b = 12$ kHz. The results produced by our method referred to as the quasi-linear (QL) method from this point on were compared against a numerical evaluation of the integrals presented in Eq. 5 of Ref. [14] and Eq. 9 of Ref. [13] (referred to as the Garrett method) for the sum and difference frequency signals, respectively. They were also compared against the results given by the method described by Ding in Ref. [15] which uses a sum of Gaussian beams to approximate a flat piston aperture (referred to as the Ding method). All three methods attempt to reproduce the results of the measurements made by Garrett *et al.* [20] in 1982.

Figure 1 compares the results given by all three methods for the lateral profile at three different depths for the sum and difference frequency signals. The results match well with the measurements reported on Fig. 11 of Ref. [13]. Axial profiles for the signals at the sum and difference frequency were also computed by the QL method. The results are compared against the results given by the

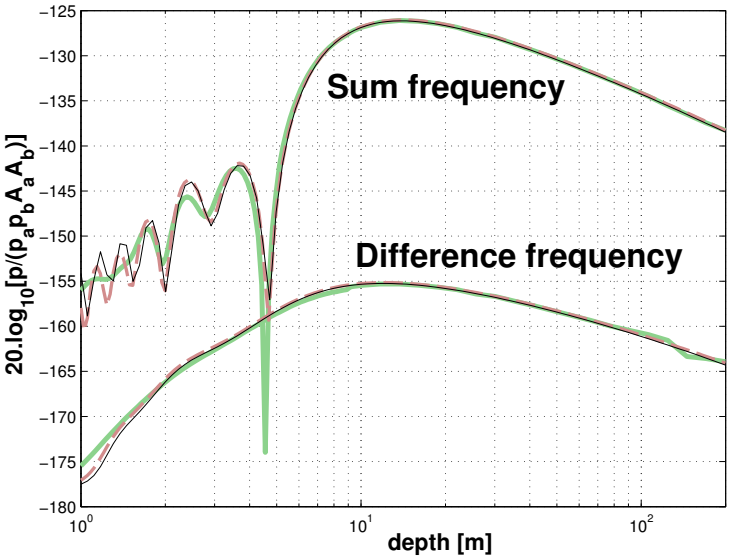

Fig. 2: *Axial profiles for the signals at the sum and difference frequency obtained by the QL method (bold), the Ding method (dashed), and the Garrett method (thin). The axial pressure is normalized by the pressures of the transmitted beams p_a and p_b and by the areas of the transducer emitting the primary beams A_a and A_b.*

Garrett and Ding methods in Fig. 2. Again, there is a good match with the measurements reported on Fig. 3 of Ref. [13].

The average difference between the QL method and the other methods is below 1.8 dB and 0.9 dB for the lateral profiles of the signals at the sum and difference frequency, respectively, and below 0.8 dB and 0.4 dB for the axial profiles.

IV. Discussions

The method described in Refs. [13–15] use the Khokhlov-Zabolotskaya-Kuznetsov (KZK) equation as a starting point. This equation uses the parabolic approximation that is valid for directional beams. The QL method uses the Westervelt equation as a starting point that does not make the parabolic approximation. The parabolic approximation is equivalent to replacing the expression for the real part of $K_t(\mathbf{k})$ by

$$Re[K_t(\mathbf{k})] = \frac{\omega_t}{c_0} - \frac{c_0(k_x^2 + k_y^2)}{2\omega_t}. \tag{21}$$

while our simulator uses

$$Re[K_t(\mathbf{k})] = \sqrt{\omega_t^2/c_0^2 - k_x^2 - k_y^2}. \tag{22}$$

Consequently, the QL method should be more precise at short range than the other methods. That is if all spatial frequencies are taken into account. For the computation to be feasible in a reasonable amount of time, the extent of the spatial frequency domain has to be limited. Since the near field

contains high spatial frequencies, the QL method applies, in this domain, a low-pass spatial filter which damps the variations of the near field as shown in Fig. 2.

The integral solutions presented in Refs. [13] and [14] are valid only for flat piston sources with an axial symmetry while the approximation presented by Ding in Ref. [15] applies to any source with axial symmetry. This theory can be extended to approximate sources with arbitrary source distribution and geometry by a sum of two-dimensional Gaussian beams but the final form still requires the evaluation of an integral over the propagation direction [21, 22]. The QL method provides a full 3D estimate of the signals at the sum and difference frequency and can be used with transducers of arbitrary geometry. In addition, the extra step needed to compute the coefficients describing the Gaussian beams in Ding's method is avoided.

While the compared methods assume a mono-frequency signal, the QL method can model signals with a large frequency bandwidth. Sub-bottom characterizing applications often use wide bandwidth pulses like Gaussian pulses to guarantee a good range resolution [2, 3, 23]. Likewise underwater communication use phase shift keying modulated signals with large bandwidth in order to achieve high bit rates [5]. In the case of mono-frequency signals the convolutions in Eqs. (14) and (15) involve only two dimensions, the transverse spatial frequencies, while for large bandwidth pulses the additional temporal frequency dimension has to be taken into account.

The QL method encounters limitations due to the assumptions it relies on. It assumes a homogeneous media and quasi-linear propagation. This means that if the media deviates from a homogeneous model, like the layers of the sub-bottom, the results given by the method become less accurate. Similarly, if the transmitted levels exceed a certain threshold, the energy transmitted to harmonics of degree greater than two is not negligible and the quasi-linear model is not valid anymore. The fundamental and second harmonic pressure levels are therefore over-estimated in this case.

For very long propagation distances, the simulation domain has to be taken large enough to avoid perturbations coming from source replica generated by the discrete Fourier transform. This slows down the computation for lateral profiles at long range.

V. Conclusions

A method that solves the propagation of parametric signals in a homogeneous medium has been presented. It provides estimates for the lateral profile of the parametric signals at the sum and difference frequency without the need for stepwise propagation. The results given by the method have been compared to other analytical forms and match within 1.8 dB for the calculated lateral profiles, and 0.8 dB for the axial profile.

The main advantage of this method is that it allows more flexibility in the model. It directly models any transducer geometry and any power law attenuation. It is not reduced to the case of a continuous wave and can model pulses with a wide bandwidth. The method is based on the assumption of quasi-linearity, which puts a limitation on the level of transmitted pressure. Above a certain level, the first and second harmonics can be over-estimated.

This method could be used to estimate the pressure level and the beam profile of the parametric signals when using sub-bottom target detection. Both allow an accurate estimation of the sound intensity that hits a target. Corrolating this knowledge with the reflected echo from the target could contribute to a better determination of the size and type of targets. If the sound propagates in water

and in sediments, the simulation can be divided into two parts where the first part estimates propagation in water and the second part estimates propagation in sediments. The frequency spectrum obtained by the first simulation at the interface water-sediment would be the input to the second simulation. This approximates the medium as a stack of homogenous layers perpendicular to the sound main propagation direction.

Bibliography

[1] P. Pettersen, J. M. Hovem, A. Løvik, and T. Knudsen, "A new sub-bottom profiling sonar using a non-linear sound source," *Radio Electr. Eng.*, vol. 47, no. 4, pp. 105–111, Mar. 1977.

[2] A. Caiti, O. Bergem, and J. Dybedal, "Parametric sonars for seafloor characterization," *Meas. Sci. Technol.*, vol. 10, no. 12, pp. 1105–1115, Dec. 1999.

[3] P. Morén and J. Pihl, "Sub-bottom Characterisation using a Parametric Sonar," in *OCEANS'98 Conf. Proc.*, vol. 3, Nice, France, Oct. 1998, pp. 1828–1832.

[4] J. Dybedal, O. Bergem, and A. Løvik, "Application of a Parametric Source for Sediment Characterisation and Object Detection," in *OCEANS'97 Conf. Proc.*, vol. 2, Halifax, NS , Canada, 1997, pp. 1376–1881.

[5] R. F. W. Coates, M. Zheng, and L. Wang, ""BASS 300 PARACOM": A "Model" Underwater Parametric Communication System," *IEEE J. Oceanic Eng.*, vol. 21, no. 2, pp. 225–232, Apr. 1996.

[6] A. L. Vyas, V. S. Balaji Raj, and R. G. Gupta, "Design considerations of parametric arrays," in *Proc. 1998 Inter. Symp. Underwater Technol.*, Tokyo, Japan, Apr. 1998, pp. 98–102.

[7] L. Kopp, D. Cano, E. Dubois, L. Wang, B. Smith, and R. F. W. Coates, "Potential performance of parametric communications," *IEEE J. Oceanic Eng.*, vol. 25, no. 3, pp. 282–295, Jul. 2000.

[8] L. Bjørnø, "Forty years of nonlinear ultrasound," *Ultrason.*, vol. 40, no. 1–8, pp. 11–17, 2002.

[9] P. J. Westervelt, "Parametric acoustic array," *J. Acoust. Soc. Am.*, vol. 35, no. 4, pp. 535–537, Apr. 1963.

[10] H. O. Berktay, "Possible exploitation of non-linear acoustics in underwater transmitting applications," *J. Sound Vib.*, vol. 2, no. 4, pp. 435–461, Oct. 1965.

[11] T. G. Muir and J. G. Willette, "Parametric acoustic transmitting arrays," *J. Acoust. Soc. Am.*, vol. 52, no. 5B, pp. 1481–1496, 1972.

[12] M. B. Moffett and R. H. Mellen, "Model for parametric acoustic sources," *J. Acoust. Soc. Am.*, vol. 61, no. 2, pp. 325–337, Feb. 1977.

[13] G. S. Garrett, J. Naze Tjøtta, and S. Tjøtta, "Nearfield of a large acoustic transducer, Part II: Parametric radiation," *J. Acoust. Soc. Am.*, vol. 74, pp. 1013–1020, Sep. 1983.

[14] J. Berntsen, J. Naze Tjøtta, and S. Tjøtta, "Nearfield of a large acoustic transducer. Part IV: Second harmonic and sum frequency radiation," *J. Acoust. Soc. Am.*, vol. 75, pp. 1383–1391, May 1984.

[15] D. Ding, "A simplified algorithm for the second-order sound fields," *J. Acoust. Soc. Am.*, vol. 108, pp. 2759–2764, Dec. 2000.

[16] M. F. Hamilton and C. L. Morfey, "Model equations," in *Nonlinear Acoustics*, M. F. Hamilton and D. T. Blackstock, Eds. San Diego, CA: Academic Press, Dec. 1998, ch. 3, pp. 41–63.

[17] M. J. Buckingham, "Theory of acoustic attenuation, dispersion, and pulse propagation in unconsolidated granular materials including marine sediments," *J. Acoust. Soc. Am.*, vol. 102, no. 5, pp. 2579–2596, Nov. 1997.

[18] F. Prieur, T. F. Johansen, S. Holm, and H. Torp, "Fast simulation of second harmonic ultrasound field using a quasi-linear method," *J. Acoust. Soc. Am.*, vol. 131, pp. 4365–4375, Jun. 2012.

[19] H. Torp, T. F. Johansen, and J. S. Haugen, "Nonlinear wave propagation - a fast 3D simulation method based on quasi-linear approximation of the second harmonic field," in *Proc. IEEE Ultrason. Symp. 2002*, vol. 1, Munich, Germany, Oct., pp. 567–570.

[20] G. S. Garrett, J. Naze Tjøtta, and S. Tjøtta, "Nearfield of a large acoustic transducer, Part I. Linear radiation," *J. Acoust. Soc. Am.*, vol. 72, pp. 1056–1061, Sep. 1982.

[21] D. Ding, "A simplified algorithm for second-order sound beams with arbitrary source distribution and geometry (L)," *J. Acoust. Soc. Am.*, vol. 115, pp. 35–37, Jan. 2004.

[22] Y. Jun, S. Kan, G. Woon-Seng, and T. Jing, "A Fast Field Scheme for the Parametric Sound Radiation from Rectangular Aperture Source," *Chinese Phys. Lett.*, vol. 21, pp. 110–113, Jan. 2004.

[23] A. Trucco, "Detection of objects buried in the seafloor by a pattern-recognition approach," *IEEE J. Oceanic Eng.*, vol. 26, no. 4, pp. 769–782, Oct. 2001.

Paper VII

Multi-Line Transmission in medical imaging using the second harmonic signal

F. Prieur, B. Dénarié, A. Austeng, and H. Torp

IEEE Transactions on Ultrasonics, Ferroelectrics, and Frequency Control, submitted July 3, 2012.